ISTITUTO ITALIANO
DI TECNOLOGIA

UNIVERSITÀ DEGLI STUDI
DI GENOVA

Modelling Neuron Morphology: Automated Reconstruction from Microscopy Images

Author:
Dott. Silvia Baglietto

Supervisor:
Prof. Vittorio Murino
Dr. Diego Sona

A thesis submitted in fulfillment of the requirements
for the degree of Doctor of Philosophy

Doctoral Course on “Computational Vision, Automatic Recognition and Learning"
Doctoral School on “Science and Technology for Electronic and
Telecommunication Engineering”

Università degli Studi di Genova
Istituto Italiano di Tecnologia
Pattern Analysis and Computer Vision, PAVIS

XXX Cycle - Genoa, March 2018

Abstract

Understanding how the brain works is, beyond a shadow of doubt, one of the greatest challenges for modern science. Achieving a deep knowledge about the structure, function and development of the nervous system at the molecular, cellular and network levels is crucial in this attempt, as processes at all these scales are intrinsically linked with higher-order cognitive functions.
The research in the various areas of neuroscience deals with advanced imaging techniques, collecting an increasing amounts of heterogeneous and complex data at different scales. Then, computational tools and neuroinformatics solutions are required in order to integrate and analyze the massive quantity of acquired information. Within this context, the development of automatic methods and tools for the study of neuronal anatomy has a central role. The morphological properties of the soma and of the axonal and dendritic arborizations constitute a key discriminant for the neuronal phenotype and play a determinant role in network connectivity. A quantitative analysis allows the study of possible factors influencing neuronal development, the neuropathological abnormalities related to specific syndromes, the relationships between neuronal shape and function, the signal transmission and the network connectivity. Therefore, three-dimensional digital reconstructions of soma, axons and dendrites are indispensable for exploring neural networks.

This thesis proposes a novel and completely automatic pipeline for neuron reconstruction with operations ranging from the detection and segmentation of the soma to the dendritic arborization tracing. The pipeline can deal with different datasets and acquisitions both at the network and at the single scale level without any user interventions or manual adjustment. We developed an ad hoc approach for the localization and segmentation of neuron bodies. Then, various methods and research lines have been investigated for the reconstruction of the whole dendritic arborization of each neuron, which is solved both in $2D$ and in $3D$ images.

Contents

List of Figures

List of Tables

List of Acronyms

AC Active Contour

CLSM Confocal Laser Scanning Microscopy

CMOS Complementary Metal Oxide Semiconductor

CT Computer Tomography

DC Dice Coefficient

DIADEM DIgital reconstructions of Axonal and DEndritic Morphology

dMRI Diffusion Magnetic Resonance Imaging

DTI Diffusion Tensor Imaging

DS Dominant Set

FA Fractional Anisotropy

FACT Fiber Assignment by Continuous Tracking

FN False Negative

FP False Positive

fMRI Functional Magnetic Resonance Imaging

GT Ground Truth

HD-MEA High-Density MEA

ICBM International Consortium for Brain Mapping

JI Jaccard Index

LGN Lateral Geniculate Nucleus

LSM Light-Sheet Microscopy

MEA Micro Electrode Array

MRI Magnetic Resonance Imaging

MS Mean Separation

MST Minimum Spanning Tree

Acronyms

PSF Point Spread Function

RENVISION Retina-inspired ENcoding for advanced VISION tasks

RGC Retinal Ganglion Cell

ROI Region of Interest

TN True Negative

TP True Positive

WM White Matter

Introduction

The word *brain* appears as the first recorded statement in the *Edwin Smith Surgical Papyrus*, an ancient Egyptian medical text written in the 17th century BC. Since this period of the ancient Egyptian mummifications to 18th century scientific research on "globules" and neurons, there is evidence of neuroscience practice throughout the early periods of man history. Since then, the brain research holds a leading role in the scientific community from Greek philosophers-scientists' works, through Leonardo Da Vinci's studies during the Renaissance, till the Modern Era [Gross, 1999]. Neuroscience is really old but, to the detriment of thousands years of studies, most of brain mechanisms and functions still remain unknown: the brain remains the most formidably complex and the most uncovered system in biology. This fact is confirmed by the activity in this research area suggesting that there is still a large amount of knowledge to be discovered.

Brain processing involves a huge number of cells with heterogeneous phenotypes that are structurally and functionally organized in a complex architecture at multiple scales. This complicated network is responsible of mental processes, starting from basic sensorimotor tasks to cognitive and executive functions. Thanks to recent improvements in data acquisition technology, such as advanced imaging modalities with sophisticated microscopes and Magnetic Resonance Imaging (MRI), an ever-increasing amount of data has become available for analysis. The massive quantity of acquired information requires powerful computational capabilities and advanced processing algorithms to overcome the poor scalability/reliability of manual measurements and visual evaluation. So, the comprehension of the brain demands the attention of different research fields, from psychology, biology and neuroscience to computer science, mathematics and engineering.

In the last decades a big effort has been put forward to investigate the so called *connectome*, defined as "a comprehensive structural description of the network of elements and connections forming the human brain" [Sporns et al., 2005], with

fundamental insights for health and disease. The term *connectomics* identifies a wide scope, ranging over different connectivity scales: at the microscale describing single neuron interplays; at the mesoscale reconstructing the neuronal population connectivity; at the macroscale depicting the pathways at the brain regions level [Leergaard et al., 2012]. The first step through the comprehension of the connectome has been done into the direction of the *structural connectivity* that is how the neural elements are physically connected, providing an anatomical description of networks nodes, such as neurons (*microscale*) or brain regions (*macroscale*). Then, beside the structural connectome, the functional connectome is referred to *functional connectivity*, which is mainly viewed as an undirected statistical measure between neural elements over time. In particular, the functional connectivity measures the activity of neurons or brain areas from the study of synchronous patterns of neuronal activation [Rykhlevskaia et al., 2008]. Interestingly, thanks to the multimodal analysis, structure and function reveal to be highly related.

Looking at the microscale interactions, we can observe that the functional properties of each neuron are strongly driven by their soma morphology, dendritic arborizations, synaptic distributions and anatomical interconnections with other cells [Baden et al., 2016].

Regarding neuronal network studies, there is a growing interest in the scientific community towards the structural and functional organization of the retina. The retina is a photosensitive membranous tissue lying at the back of the eye. Its role is to process the light stimuli and to transmit the information to the brain through the optic nerve. Although it is often compared to a photographic film on which the images are imprinted and encoded into electrical signals with a columnar processing, the retina has a very complex function and structure, composed of several layers of cells in a tangled network [Gregory, 2015]: photoreceptors feed into bipolar and amacrine cells, which pass the input to an assorted set of retinal ganglion cells (RGCs). Recent studies show that retina performs sophisticated non-linear computation, extracting spatio-temporal visual features with high selectivity. This is reflected by the fact that distinct RGC types have been found to encode specific visual features for transmission to the brain [Neumann and H 2016]. According to the current knowledge, there is a correlation between RGC morphology and function and this is usually studied at the single cell level [Berson et al., 2010]. Recently, an intense debate is rising around the importance of studying the retina at the circuit level and the actual challenge is to tackle the problem at a different scale, analyzing populations of neurons at a network level [Roska et al., 2006], [Kim et al., 2010]. Several studies are trying to model responses of RGC populations heading to a better understanding of the role of RGCs [Baden et al., 2016]. To support neuroscientists in this study, automated tools

for the large-scale segmentation of neuron structures are required.

This thesis addresses this challenge by proposing a combined pipeline for detecting and segmenting neurons at the population level. In this way, this can help in the neuronal cell functional classification based on their morphology [Torben-Nielsen et al., 2007]. Multimodal studies on structure-function find a growing field thanks to recent imaging acquisition technologies that can capture neuronal anatomy and physiology at multiple scales and at unprecedented resolution [Feldt et al., 2011]. Attempts in this direction have mostly concerned the macroscopic study of functional and structural connectomics at the brain-area level. However, *macroscale* approaches are not suitable for single-neuron resolution as they deal with large regions, involving billions of neurons, that make any fine-grained analysis impracticable. On the other hand, *microscale* studies achieves good resolution by focusing on single cells, but looses the information on the topology and interplays of the full network. The gap of knowlegde between micro and macro can be filled by the so-called *mesoscale*. Mesoscale connectomics studies connectivity at the level of neuronal networks and populations with a micrometric spatial resolution [Sporns, 2011]. Moreover, many of the stratified complex mechanisms underlying brain processing can be particularly observed at this scale. Therefore, it becomes important to capture how neurons play in a network to accomplish the simple tasks on top of which high-level functions - such as learning and memory - rest on [Jimbo et al., 1999], [Marom and Eytan, 2005].

The advent of multi-electrode array technology (MEA) allows a further step to characterize the connections between patterns describing a mesoscale for studying neuronal networks [Spira and Hai, 2013]. In particular, novel generations of active Micro Electrode Arrays (MEAs), such as the High-Density MEA (HD-MEA) chips [Berdondini et al., 2009], can record the electrical activity of neuronal networks from thousands of electrodes at sub-millisecond resolution and approach the granularity of the single cell. The multimodal acquisition of such an high-resolution functional data with fluorescence microscopy imaging can enable an unprecedented mapping of both activity and structure of neural populations at a cellular scale. Indeed, relatively sparse neuronal assemblies, grown on-chip by seeding few thousand cells, and retinal samples (as in our case studies) provide to acquire detailed spatio-temporal acquisitions of neuronal activations and topological distribution of cells with respect to the electrode grid. This allows a chance of correlating functional activity with neuronal topography over large assemblies. Within this framework, new computational challenges come from the acquisition of highly-complex multimodal datasets that require innovative methods for their analysis.

Goals and Contributions

Aim of this thesis is to provide automated computational tools for studying the morphology of neurons both at the single and at the network scale. This problem is addressed by developing an automatic pipeline for the anatomical analysis of fluorescence images, focusing on a whole reconstruction of the neuron: from the detection of neuronal cells to the segmentation of their body and dendritic tree. This morphological reconstruction represents the necessary step towards a full structural and functional integration.

Neuronal datasets are complex for different reasons. First of all, there is an high heterogeneity of samples across different acquisitions. Images show high cell density and shape variety and there is a low contrast at the neuron boundaries. Indeed, the fluorescence expressed is non-uniform: it has higher values into the soma and leads to fragmentation and gaps into dendrite appearance.

To overcome these challenging features, ad hoc processing steps are crucial to improve the quality of images, for example through a background suppression and an enhancement of the structures of interest, while lowering the contribution of other elements in the images.

The first part of the work aims at the detection and segmentation of neuron bodies developing an ad hoc approach that can deal with different datasets and acquisitions without any user interventions or manual adjustment. Within this framework, we propose a new multiscale blob enhancement filter that detects neuronal bodies, both in images of population and of single neurons. Then, we perform the segmentation by a localizing region-based active contour which finds the contour of cells and of group of cells and by a watershed transform that separates contiguous somas.

The second part of the work proposes various methods and research lines for the reconstruction of the whole dendritic arborization of each neuron, which is done both in the $2D$ than in the $3D$ images. In the $2D$ case, segmented somas are used as initialization seeds to start the reconstruction of attached processes. To solve this task, we designed a level set propagation with local phase and with Hessian eigenvalues information. In order to automatically trace the $3D$ volume of neurons, an innovative pipeline that overcomes the challenging and problematic features of the datasets is then developed. During a preprocessing step, a ROI mask of the dendrite structures is designed by the Frangi Filter. This mask is used for driving a tracker using the principal directions extracted in each voxel. The inspiration comes from Neuroimaging, where a similar idea has been developed for deteministic MRI tractography. After this point, we have investigated different solutions in order to create a continuous tracing starting from the tracked fibers. First, a geometrical approach is developed.

Then, a more precise reconstruction is performed by an active contour segmentation initialized by all traces and also by the most representative ones chosen as centroids of clusters computing by a Dominant Set Clustering Approach.

Content Overview

The content of the thesis is organized in four main chapters as follows.

First of all, a brief biological background about neurons and retina is provided in Chapter 1 to introduce the basic concepts about the neurobiology of the subjects of our reseach with the related state of art studies.

In Chapter 2, the acquisition process of fluorescent images is described. It follows a summary about the $HD-MEA$ recordings that allows the multimodal analysis. Then, the datasets used for our studies and researches are illustrated and shown in the remain of the chapter.

The central core of the thesis is revealed in the Chapter 3 and in the Chapter 4. Chapter 3 presents the part of the pipeline related to the detection and segmentation of cell bodies. First, the state-of-art is provided focusing the attention on how this type of dataset is peculiar and discusses the importance of having completely automatic methods for the analysis. Then, it introduces our approach dealing with the detection of the soma and its segmentation [Baglietto et al., 2017a]. It is fully automatic and it has been tested on two datasets showing good results for images of both single cells and neuron populations.

Chapter 4 deals with the dendritic arborization reconstruction. Once the neuron has been localized and its soma has been segmented, the dendritic tracing is required in order to obtain the whole neuron morphology. After a summary about the existent methods, our solution is proposed starting from $2D$ images. Using the soma localization and segmentation, a pipeline is developed with an improved level set model obtaining encouraging results on $2D$ images. The second part of the Chapter is related to the same problem on $3D$ images. We propose different solutions that we have explored in order to find the best results in a so complex framework [Baglietto et al., 2017b].

Finally, conclusions are exposed opening possible directions for future investigations.

1 Background

In this Thesis, computer science is connected to biology and neurobiology. This Chapter presents an overview on some basic biological concepts about neurons, retina and their relative studies in order to link the biological background with our works.

1.1 Neurons

Neurons are one of the most important cell types of any organism and they are the *elementary functional units* of the brain tissue. The key numbers of the human brain are very impressive. They underline the difficulties into the understanding of how the brain works. The avarage human brain has about 100 billions of neurons. Every neuron has on average up to 10000 synapses. The total number of synapses of a human, adult brain is estimated to be in the range of 10^{14} to 5×10^{14} synapses. Although the brain presents a great diversity and quantity of neuronal cells, they all share a common fundamental architecture enabling their communication in a rapid and precise way [Kandel et al., 2000].

For their neuron studies, Camillo Golgi and Santiago Ramòn y Cajal (shared Nobel Prize in Medicine in 1906) are considered as the founders of modern neuroscience [De Carlos and Borrell, 2007]. In 1873, Golgi had developed a sparse staining method for brain tissue, which was further improved and extensively used by Cajal. Fig. 1.1 shows a drawing by Cajal made in 1899 of nerve cells in pigeon cerebellum. The Golgi's method can stain only a small subset of cells, but if a cell is stained, it is stained in its entirety. Based on this observations, Cajal states that the nervous system is composed of individual cells ("*neurons*"), as opposed to a diffuse network as claimed

by Golgi and others.

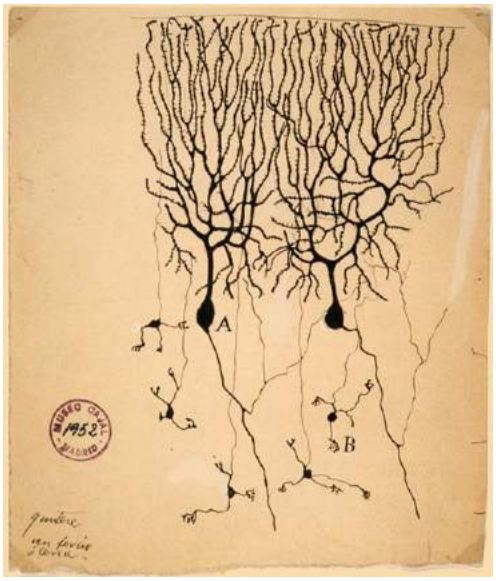

Figure 1.1 – Drawing of Purkinje cells (A) and granule cells (B) from pigeon cerebellum by Santiago Ramòn y Cajal, 1899. Instituto Santiago Ramòn y Cajal, Madrid, Spain.

A neuron has a cell body called *soma*, that is the metabolic center of the neuron. From the soma, two types of *processes, dendrites* and *axons* (collectively called *neurites*), depart, being in charge of delivering electrical impulses to other target neurons. The soma typically gives rise to multiple dendrites, which branch in a tree-like shape in the area near the soma. While the density of dendrites ensures the interconnection of a neuron to a great number of other neurons, the axonal connection allows rapid signal propagation over very large distances [Dayan et al., 2003]. At its end, the axon branches into terminals (*presynaptic terminals*) forming the communication sites - called *synapses* - with other nerve cells (*postsynaptic neurons*).

Neurons can be classified according to their functional behavior in three main classes: *sensors, motors* and *interneurons*. Sensor and motor neurons are in charge of - respectively - delivering perceptive information from the periphery to the brain and motor commands from the brain to muscles and glands. Instead, the interneuronal neurons cover the rest of brain nerve cells and can interact on a local basis with short-range axons or extend over considerable distances conveying signals from one brain region to another.

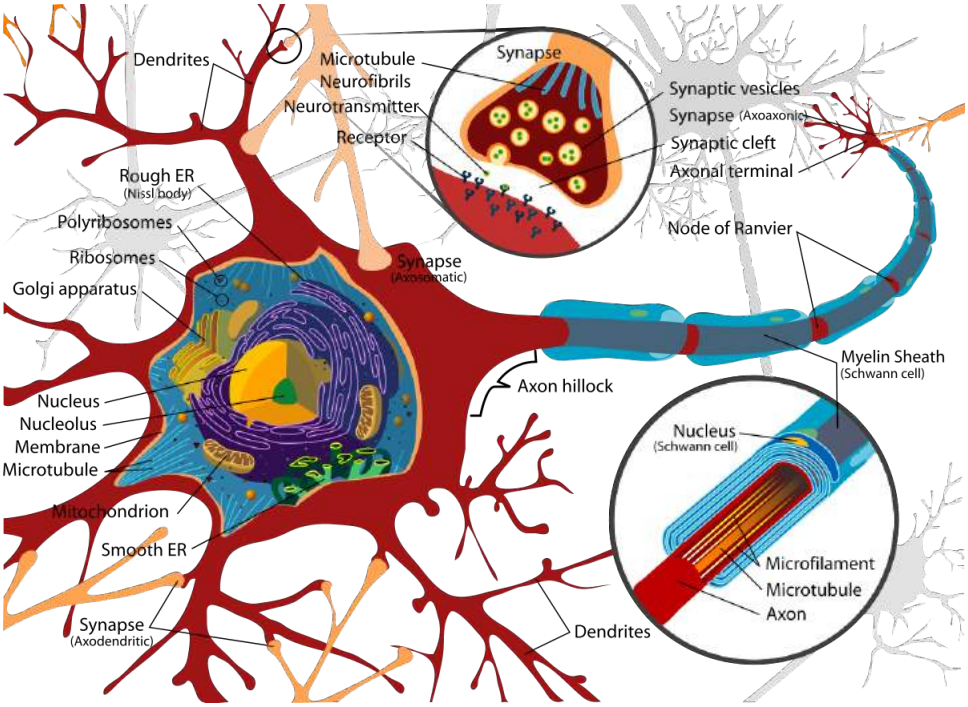

Figure 1.2 – Image from [Wikipedia,] showing the different part of a neuron and its connections with the attached neurons.

At resting state, neurons have negative electrical potentials inside their cell membrane. This state is called *polarization*. When an incoming stimulus arrives (*receptor potential*), the neuron starts depolarizing, i.e. its potential changes to less negative or even positive values. If the sum of all converging potentials is above some threshold, this rapid change in the potential across the cell membrane generates an *action potential*, i.e. an all-or-nothing electrical impulse which can travel along axon over large distances without any attenuation. Action potentials - also called *spikes* - represent how neuronal signaling takes place, i.e. the way the brain accomplishes its tasks of receiving, analyzing and conveying information [Kandel et al., 2000]. A sequence of action potentials occurring together is called a *spike train*. When an action potential reaches the presynaptic terminals, this impulse stimulates the emission of *neurotransmitter molecules* from their containers, the *vesicles*. These molecules bind to the synaptic receptors generating a *synaptic potential* and stimulating the postsynaptic neuron. This relation was studied for the first time by Otto Loewi and

Henry Dale (Nobel Prize 1936), who found evidence that information can be sent between neurons by chemical means: neurotransmitter molecules are released in one cell and sensed by another [Seung, 2012]. Synapses connect directly one presynaptic cell with one or several postsynaptic cells. Synaptic potentials can assume an *inhibitory* or *excitatory effect*, according with the type of receptors in the postsynaptic cell. On the contrary to excitatory receptors, inhibitory receptors generate a decrease in the membrane potential - called *hyperpolarization* - which makes the postsynaptic neuron less likely to generate action potentials.

Even if spike signals can differ in amplitude, shape and duration, only two features are considered to bring information: the number of action potentials and the time between them, i.e. their frequency, which defines the amount of transmitter released at the synaptic gate. For this reason, spikes are typically considered as *binary events*, i.e. they are only described by the time when they occurred. Consequently, the temporal evolution of a neuron's electrophysiological signal is expressed as a set of time instants corresponding to its spiking events. In this setting, the information encoding is carried by the temporal pattern of the spikes, i.e. number and frequency of action potentials.

Most of the neuronal synapses can be classified into *electrical* or *chemical* by their structure. In the first case, pre and postsynaptic neurons are physically connected: the current generated by an action potential directly flows from one to the other; the second case is represented by a cleft separating the two connected cells. Here, a neurotransmitter from the axon terminal is released in order to transmit the signal from the pre-synaptic to the post-synaptic neuron. The neurotransmitter moves across the cleft and reaches the target neuron by binding with local receptor molecules placed in the neuronal membrane. Such a binding process allows the current to propagate through the synapse causing inhibition or excitation in the postsynaptic neuron. The sign of the signal and the inhibitory or excitatory effect of the transmission on the target neuron only depend upon the nature and chemical properties of the receptor. Both excitatory and inhibitory synaptic potentials can converge to the same neuron from various incoming arborizations. Excitatory currents depolarize the neuron stimulating an initiation of an action potential. On the other side, inhibitory potentials with their hyperpolarizing effect counteract this action and make the neuron less likely to fire. Afferent inputs are then integrated in the postsynaptic neuron by summing the synaptic potentials.

1.1.1 SWC Data File

The structure of a neuron (see previous Sec.1.1) can be modeled as a tree, which is composed of a set of nodes and the edges connecting the nodes. Each node is a ball in the 3D space and its size is specified by its radius. The edges form the skeleton of the neuron. This simple model is defined by the commonly used SWC format. SWC are the initials of the last names of E.W. Stockley, H.V. Wheal and H.M. Cole, who developed a system for generating morphometric reconstructions of neurons [Stockley et al., 1993]. Therefore, we sometimes refer to a node as a neuron node or an SWC node. Every compartment (except the root) has exactly one *parent* compartment and may have 0, 1, or 2 *children* compartments, corresponding respectively to a termination, continuation, or bifurcation. A node is defined as a *root*, *bifurcation* or *termination* in the tree. A tree model created from image data is called *tracing* and a 3D image is also called *stack*.

The Groud Truth of the Morphological neuron reconstructions are often available for download as SWC files, as in our case [Gulyanon et al., 2016] and as in DIADEM challenge dataset [Brown et al., 2011].
A file in SWC format contains information representing a digitally reconstructed neuron. SWC is non-proprietary and stores the minimum amount of parameters required to represent a vector-based three-dimensional reconstruction. For this reason, the format of an SWC file is fairly simple. It is a white-space delimited text file with a standard set of headers beginning with a # character (for comment lines) and a series of parameters are organized into 7 columns. From left to right these columns are: unique identity value for trace point, structure type, x coordinate, y coordinate, z coordinate, radius, identity value for parent (i.e. trace point that comes before and connects to the current trace point). The file lists a set of 3D neuronal compartments, where each line represents a point and have the following layout:

	1	2	3	4	5	6	7
Data Type	Sample number	Structure Identifier	$x_{position}$	$y_{position}$	$z_{position}$	$radius$	Parent Sample
Data Value	Integer value, generally continuous, starting from '1'	Standardized swc files 0 - undefined 1 - soma 2 - axon 3 - (basal) dendrite 4 - apical dendrite 5+ - custom	'x', 'y', 'z' are spatial coordinates, given in micrometers. '$radius$' is half the dendrite thickness, also given in micrometers.				The sample number. Connectivity is expressed with this value. Parent samples should appear before any child samples.

Table 1.1 – SWC is a file of subsequent non-empty lines each represent a single neuron sample point with seven data items.

1.2 Retina

The eyes together with their connecting pathways to the brain form the visual system. The visual system is beautifully crafted to transmit information of the external world to visual processing and cognitive centers in the brain [Gregory, 2015]. The *optic nerve*, a cable–like grouping of nerve fibers, transmits vision signals to the *lateral geniculate nucleus* (LGN), where visual information is relayed to the *visual cortex* of the brain that converts the image impulses into objects that we see (Fig. 1.3).

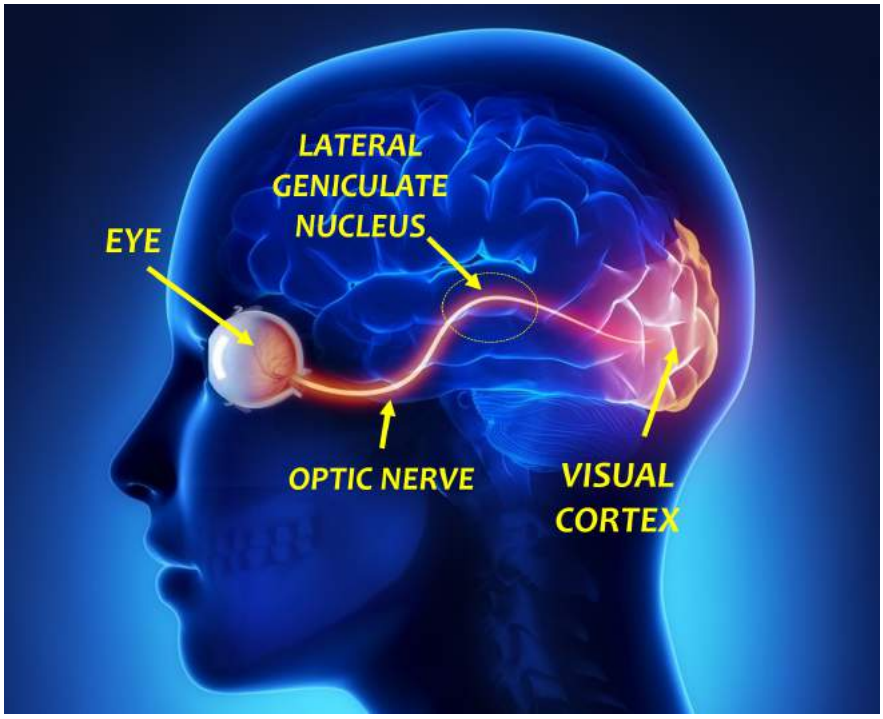

Figure 1.3 – The visual information system: eye images the world around us and sends information to the lateral geniculate nucleus thorugh the optic nerve. LGN then comunicates with visual cortex of the brain.

The visual information processing starts in the *retina*, lying at the back of the eye. Its role is to process the light stimuli and to transmit information to brain through the optic nerve (see Fig. 1.4). Light entering eye triggers *photochemical reactions* in *rods* and *cones* at back of the retina. Rod cells are responsible for our night vision, and respond well to dim light. Cone cells are placed in a central region of the retina called the fovea; they are responsible for high acuity tasks like reading, and also for

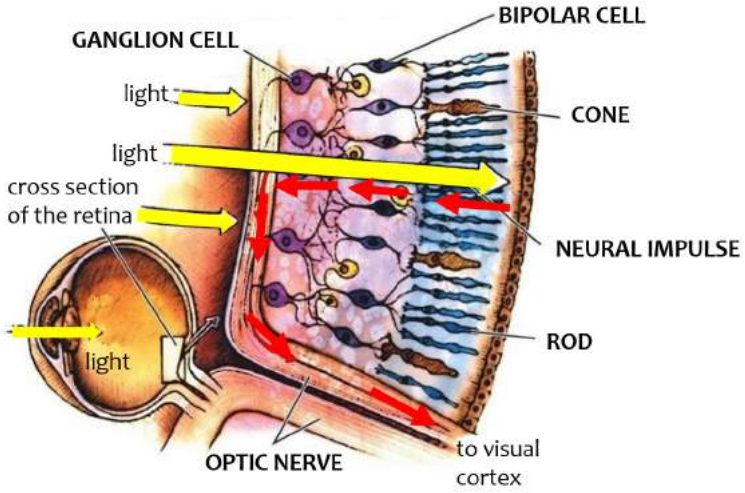

Figure 1.4 – Visual perception starts as soon as the eye focuses light onto the retina, where it is absorbed by a layer of photoreceptor cells, rods and cones, that convert light into electrochemical signals. Signals from the photoreceptor cells pass through a network of interneurons in the second layer of the retina to RGCs in the third layer. RGCs transmit the information received to the visual cortex of the brain through the optic nerv.

color vision. Cones can be subcategorized into three types, depending on how they respond to red, green, and blue light. In combination, these three cone types allow us to perceive colors. From these photoreceptor cells, chemical reactions in turn active *bipolar* and *amacrine* cells. The neurons in these retinal layer exhibit complex receptive fields that enable them to detect contrast changes within an image; these changes might indicate edges or shadows. These second layer cells then activate the *ganglion cells* (also called RGCs as Retinal Ganglion Cells), the axons of which converge to form the *optic nerve*. Ganglion cells gather these information along with other information about color, and send their output into the brain through the optic nerve. This nerve transmits information to the visual cortex in the brain's occipital lobe.

In the last decade there is an increasing interest into the studies of the retina. This depends on the fact that the retina is a sophisticated distributed processing unit of the central nervous system encoding visual stimuli in a highly parallel, adaptive and computationally efficient way. Recent studies show that rather than being a simple spatio-temporal filter that encodes visual information, the retina performs

sophisticated non-linear computations extracting specific spatio-temporal stimulus features in a highly selective manner (e.g. motion selectivity) [Zordan et al., 2015], [Cessac et al., 2017]. A lot of scientists are involved in the research activity around the retina and one of the hotter topic is around the relation of retinal ganglion cell morphology with the functional role [Kong et al., 2005], [Coombs et al., 2006]. Moreover, understanding the neurobiological principles beyond retinal functionality is also essential to develop successful artificial computer vision architectures.

1.3 State of the Art in Neuron Studies

Neuronal morphology analysis is a key determinant in the endeavor to comprehend the structure of the brain and of the nervous system. The morphological study of somas, axons and dendrites provides an essential support to understand more about synaptic integration, signal transmission, network connectivity, and circuit dynamics. Since the great advances in the cellular imaging and microscopy acquisition, there is a important rise to massive amounts of heterogeneous and complex data collected at multiple scales of observation. Computational approaches are necessary for integrating and analyzing these data to quantify the intricate relationship between neuronal morphology (structure) and physiology (activity) [De Schutter and Bower, 1994], [Borst and Haag, 1996], [Segev and Rall, 1998], [Halavi et al., 2008], [Häusser et al., 2000], [Schmitt et al., 2004], [Ascoli et al., 2007]. Therefore, digital reconstructions of the whole neuron are indispensable for exploring neural function [Svoboda, 2011].

While the body of literature on the subject is growing [Halavi et al., 2012], [Meijering, 2010], [Donohue and Ascoli, 2011] as well as challenging competitions have been organized in the field, the quest for a robust and fully automated system of more general applicability still continues.

The lack of powerful computational tools for automated neuron tracing and reconstruction has inspired several initiatives in the recent years to establish a competition. For example, *DIADEM Challenge* [Ascoli et al., 2010] (DIgital reconstructions of Axonal and DEndritic Morphology) (with a total of $75,000 in prize money) was designed to encourage the development of new algorithms to advance the field [Zhao et al., 2011], [Wang et al., 2011], [Narayanaswamy et al., 2011], [Chothani et al., 2011], [Türetken et al., 2011], [Bas and Erdogmus, 2011]. Even if it was not to be expected, in view of the past decades of many constant efforts, that a one-year competition would lead to the final solution, it aimed at attracting new generations of computer scientists to take up the field.

Some automated tools have recently appeared in the literature and proposed solutions for various tasks such as tracing, visualization and editing [Mukherjee et al., 2015], [Wang et al., 2011]. However, most of the neuroanatomists and biologists still continue to process the reconstruction of dendritic and axonal arborizations manually because available tools lack of general applicability. For this reason, there is still a need to improve automated reconstruction of the whole anatomy of neurons. Moreover, most of the computational tools require manual interactions including *Neuromatic* [Myatt and Nasuto, 2008], *Simple Neurite Tracer* [Longair et al., 2011], *NeuronJ* [Meijering et al., 2004], *Neurite Tracer* [Pool et al., 2008], *NeuronStudio*

[Wearne et al., 2005], *neuTube* [Feng et al., 2015], *FARSIGHT* [Wang et al., 2011], *V3D* [Peng et al., 2010], *Reconstruct*[Fiala, 2005] and the *AxonTracker* [Srinivasan et al., 2010].

Neuromatic is a free application providing semi-manual or semi-automatic $3D$ neuron reconstruction. It can be used as an inspecting and editing software. *NeuronJ* and *Simple Neurite Tracer* are both semi-manual tracing plug-ings of the widely used *ImageJ* (https://imagej.nih.gov/ij/), an open source image processing program designed for scientific multidimensional images [Abràmoff et al., 2004], [Collins et al., 2007]. *NeuronJ* implements a minimal cost path tracing method [Meijering et al., 2003] but it can only deal with $2D$ images. Instead *Simple Neurite Tracer* accepts also $3D$ volumes and requires user interaction for the definition of start and end points for each branch. *NeuroStudio* performs a reconstruction method using adaptive thresholding, skeletonization and rayburst sampling algorithm. It is semi-automatic because the user has to manually supply a $3D$ point at the tree root and optional points at locations where the tracing fails. *FARSIGHT* has an higher level of automation: it implements an open curve snakes that can be initialized automatically from a single seed point. It takes the first step for a system capable of automatic and semi-automatic tracing. *V3D* is a visualization tool for large-scale image datasets, supporting up to $5D$ rendering (spatially $3D$ over time and in multiple colors) of data that can be described as a graph (such as neuronal data), point clouds, and landmarks. The *V3D*-Neuron needs user-supplied terminal points of the neurites. Plus, it offers various image analysis functions (as add-on modules), and also enables user-developed plug-ins with which a user can manipulate the *V3D* platform in developing new functions. *Reconstruct* is a tool for semi-automatic segmentation of serial section electron microscopy. *AxonTracker* is a package developed for semi-automatic reconstruction of Neuromuscular Junction image volumes.

Most algorithms proposed in literature are dedicated to specific neuronal image datasets and required manual interactions. For these reasons, the interest in the field is growing but a fully automatic method for the $3D$ reconstruction remains an open question.

2 Imaging and Dataset

This Chapter will present an overview on technical methods in the acquisition of both structural and functional information from biological samples with a specific focus on microscopy acquisitions and on HD-MEA technologies. Then, the datasets under investigation are discussed in the remain of the Chapter.

2.1 Fluorescence Microscopy

Since the past century, the introduction of labeling techniques to trace neuronal networks have profoundly revolutionized the study of neuroanatomy [Kandel et al., 2000]. Basically, it is possible to label specific structures inside the cell by a *fluorochrome* or using a *fluorescent protein*. The cells can be transfected by Deoxyribonucleic acid (DNA) encoded for proteins.

Immunocytochemistry is a common laboratory technique that is used to study of cellular processes by using highly-specific antibodies which recognize target proteins. Thanks to their peculiarity, antibodies selectively bind to the protein of interest in the sample. In this way, the antibody-antigen interaction can be accurately visualized by using fluorescent detection. In this setting, a *fluorochrome* or *fluorescent dye* can be conjugated to the antibody. Fluorochromes can be excited on specific wavelengths and emit red shifted photons. Such a response can be detected under a fluorescence microscope providing an image of the structures of interest. The joint use of immunocytochemistry with fluorescent dyes is known as *immunofluorescence* [Storch, 2000]. Since fifties, this technique has been used by biologists for many different applications and biological samples, including retinal samples, cultured cells, tissues and microarrays [Coons, 1971] .

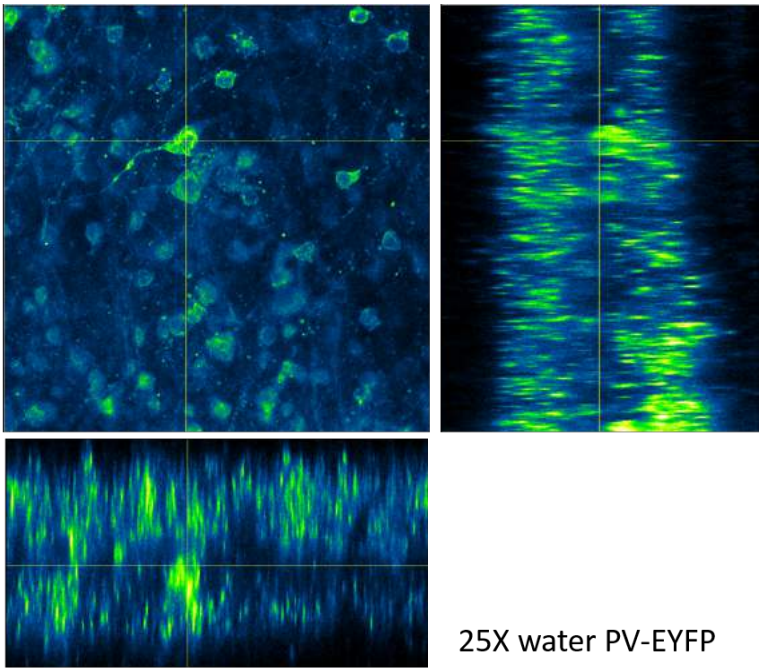

Figure 2.1 – A $xy-$ (top left), $xz-$ (bottom left) and $yz-$slice (top right) of a $3D$ fluorescence image coming from Renvision project (Sec. 2.3.1).This example shows the worse resolution in the z axis.

2.1.1 Confocal Microscopy

Confocal microscopy (also called *confocal laser scanning microscopy* (CLSM)), is an optical imaging technique for increasing optical resolution and contrast of a micrograph (i.e. a photograph or digital image taken through a microscope or similar device to show a magnified image of an item). This is obtained using a spatial pinhole to block out-of-focus light in image formation [Pawley, 2006]. In other words, a confocal microscope creates sharp images of a sample that would otherwise appear blurred when viewed with a conventional microscope. Excluding most of the light from the sample that is not from the microscope's focal plane, the image has less haze and better contrast compares to conventional microscope one and represents a thin cross-section of the sample. Thus, it is possible to build three-dimensional ($3D$) reconstructions of a volume of the sample by assembling a series of thin slices taken along the vertical axis [Semwogerere and Weeks, 2005] [Prasad et al., 2007].

Fluorescence samples are usually imaged in volume (x, y and z dimensions). In these images, edges are not clearly visible in difference to images taken in photography. For this aspect, fluorescence images are more similar to medical images like Magnet Resonance Imaging (MRI) or Computer Tomography (CT) images. In any case, the issues of fluorescence acquisitions are still different from medical images. In addition to the lack of any edge information, it has to be noticed that the axes z has a worse resolution compared with the x- and y-axes in high-resolution fluorescence microscopy. In fact, the Point Spread Function (PSF) is elongated in the z-direction. For these reasons, the application of real 3D image analysis approaches and algorithms is quite difficult and requires mostly to care in detail about the issues with the z-resolution. In Figure 2.1 we show as an example a $xy-$ (top left), $xz-$ (bottom left) and $yz-$slice (top right) representation of a $3D$ fluorescence acquisition of retinal tissue. In this image the issue of the difference between horizontal (x, y) and axial (z) resolution and sampling is well visible. In z-direction the intensity changes are not continuous. Plus, there are also intensity changes along structures which are caused by the neuron properties as well as the distribution of fluorescent dye or protein. Moreover, the dendrites have only few pixels in the axial direction. This is highlighted by the typical image resolution (image spacing) of fluorescence images: z-spacing is about $0.5\mu m$ while the x- and y-spacing are in the range of less than $0.2\mu m$. So, the image intensity does not correspond to light reflected from the objects (not like in classical photography) but it is the detected fluorescence that is emitted from the object by light excitation. Depending on sample preparation and microscope settings, huge differences in image intensities can arise in the image (and over multiple images).

In a conventional (i.e., *wide-field*) fluorescence microscope, the entire specimen is flooded in light from a light source (i.e. mercury or xenon). All parts of the specimen in the optical path are excited at the same time and the resulting fluorescence is visible directly by eye or projected directly onto an image capture device or photographic film (see Fig. 2.2 left).

In contrast, a confocal microscope uses point-by-point illumination and a pinhole in an optically conjugate plane in front of the detector to eliminate out-of-focus signal – the name "*confocal*" comes from this configuration. As only light produced by fluorescence very close to the focal plane can be detected, the image's optical resolution, especially in the sample depth, is much better than that of wide-field microscopes. However, as much of the light from sample fluorescence is blocked at the pinhole, this increased resolution is at the cost of decreased signal intensity – so long exposures are often required. After the pinhole, the light intensity is detected by

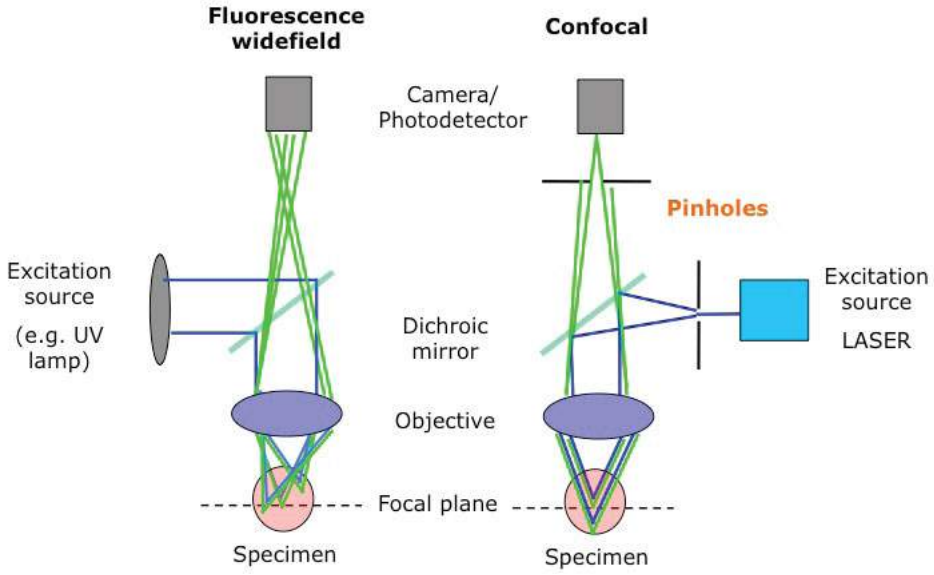

Figure 2.2 – Comparison of conventional wide field microscope with confocal fluorescence one. Two pin holes used in the confocal geometry restrict the field of view to a single point on the focal plane.

a sensitive detector, that transforms the light signal into an electrical one recording by a computer. Thus, the two pinholes working together effectively restrict the field of view of the sample fluorescence to a point on the focal plane (see Fig. 2.2 right).

Successive slices make up a 'z-stack' which can either be processed by specific softwares to create a 3D volume or can be merged into a 2D projection image (usually the maximum pixel intensity is taken, but there are other common methods including the usage of the standard deviation or summing the pixels). The most popular free software for microscopy image processing is *ImageJ* [Schneider et al., 2012], [Schindelin et al., 2012].

2.2 Micro Electrode Array : MEA

The Micro Electrode Array technology can record the electrophysiology of the extracellular activity of neurons. Neuronal signals can be reordered in extracellular and intracellular modality [Maccione et al., 2012]. Intracellular recordings are executed by the usage of glass electrodes (e.g. patch electrodes) which allows to record both rapid spikes and the under slowly-varying subthreshold potential. On the other side, to register the extracellular activity the electrode is sited close to a neuron soma in order to reveal only its overthreshold spiking activity.

The first MEA technology appeared around the seventies [Thomas et al., 1972] and have been improving in the recording and stimulation systems [Baumann et al., 1999], [Berdondini et al., 2006]. While the spatial resolution (about $100\mu m$) and the number of electrodes (a few hundreds) are limited in the first devices, in 2009 there was a great improvement in the spatio-temporal resolution that overcome previous constraints [Berdondini et al., 2009]. This new implementation allows the recording of the electrical activity of *in-vitro* neuronal networks by thousands of electrodes at sub-millisecond resolution at the single-cell level. The new MEA platform is called *High Density Micro Electrode Array* (HD-MEA) based on the Complemenatary Metal Oxide Semiconductor (CMOS) technology and is composed by an array of 64×64 electrodes that provides acquisitions at a full-frame rate of 7.8 KHz and with a spatial resolution of $21\mu m$ (see Fig. 2.3).

The key feature of HD-MEA is that their high electrode density beats the spatial undersampling that other MEA platforms suffer. Thanks to this, the cases in which the same event is recorded by multiple electrodes should be limit. So, the number of false positive spike detections is reduced and the system allows a more accurate study if whole-network dynamics.

HD-MEA can be applied in a wide range of studies from the alteration in the neuron signals under the effect of chemical compound to the investigation of high-level coding and learning mechanisms of neuron populations [Jimbo et al., 1999], [Marom and Eytan, 2005]. They are also applicable in the record of electrophisiology of different biological samples, including disassociate cultures and retina or brain slices. Thanks to their high spatial resolution, it is possible to study the high-level abstraction of identifying neurons with the underlying electrodes. And it makes possible to link the network structure to the functional activity.

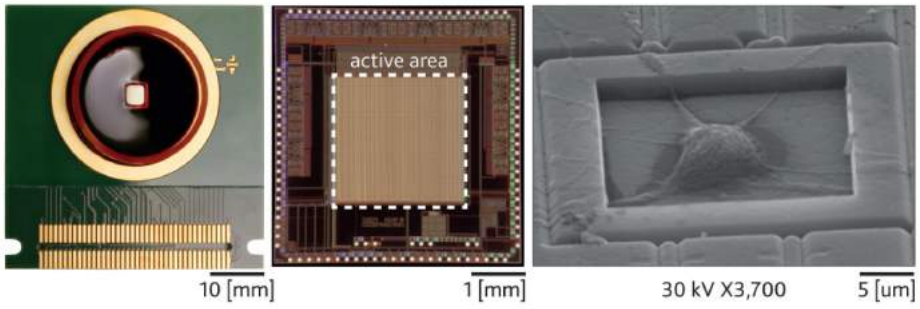

Figure 2.3 – High-Density Multi-Electrode Array. From left to right: 1) The HD-MEA chip implemented in the CMOS technology, 2) A close-up on the HD-MEA circuitry. The platform features an active area of 4096 electrodes arranged in a $64 \times 64 matrix$. Each electrode has a square-shape with $42 \mu m$ side pitch and a recording area of $21 \mu m$. 3) A cultured nerve cell lying on an HD-MEA electrode.

2.3 Reference Datasets

Our studies have been concentrated on two different groups of data: *Mouse Retina* and *Larva Drosophila*. The first important difference between the dataset is that *Mouse Retina* samples show RGCs at a population level both in $2D$ and in some cases in $3D$ acquisitions while *Larva Drosophila* presents volumes of single neurons. Both dataset are imaged using fluorescent confocal microscope and present common challenging features:

- images are affected by low contrast between structures and background;
- the fluorescence expressed in these images is non-uniform, leading to fragmented appearance of the objects and to unreliable separation between somas, dendrites and axons;
- there is a high variability of sample condition across different microscopic acquisitions;
- in *Mouse Retina* dataset, there are an high cell density, shape deformations, occlusions among neurons and processes and the presence of a large mass of structures such as dendrites and axons on the same channel.

Hence, pre-processing is a necessary step to improve image quality through the enhancement of the structures of interest. To this end, in this thesis is developed a framework addressing all the steps of morphological reconstruction, from pre-processing to cell body and dendrite segmentation.

2.3.1 Mouse Retina

The first dataset under investigation is called *Mouse Retina* and contains images and volumes from fluorescent samples of mouse retinas recorded by confocal microscope acquired during RENVISION Project (see the following subsection). In some case, sample activity is also recorded by MEA technology. For this reason, in some case, sample volume imaging is blurred by the presence of MEA chips as Fig. 2.4b) shows and they cannot be acquired easily in their $3D$ volume .

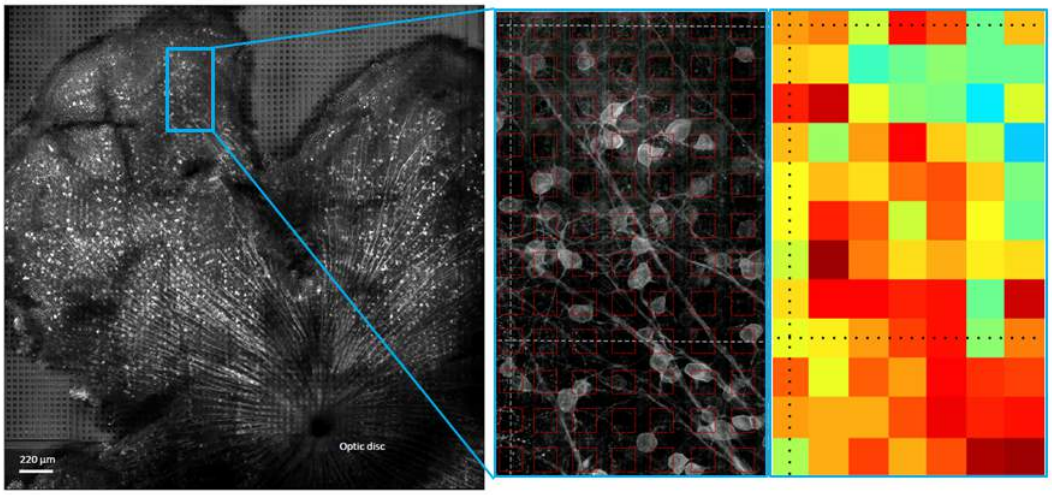

Figure 2.4 – a) Whole mount retina automatically stitched (with built in algorithm in Leica $SP5$) from 7×7 subfield images, high resolution imaging data in mosaic single plane. b) Image of 12×7 electrode array (taken by Leica $SP5$ with objective $25 \times /0.95 NA$) with the electrodes highlighted by red squares. c) The corresponding electro-physiological recording map of b)

Renvision Project

RENVISION (Retina-inspired ENcoding for advanced VISION tasks) is a three-year project funded by the European Union FP7 FET (Future Emerging technology) proactive program: Neuro-Bio-Inspired Systems.
RENVISION aims at achieving a comprehensive understanding of how the biological retina encodes visual information through the different cellular layers, and to use such insights to develop a new generation of retina-inspired ICT systems that can automatically accomplish real-world visual tasks, far more efficient and robust than existing technologies.
To this aim, exploiting the recent advances in high-resolution light-sheet microscopy (LSM) $3D$ imaging and high-density multi-electrode array (MEA) technologies, RENVISION is in an unprecedented position to investigate pan-retinal signal processing at high spatio-temporal resolution, integrating these two technologies in a novel experimental setup. This allows for simultaneous recording from the entire population of ganglion cells and functional imaging of inner retinal layers at near-cellular resolution, combined with $3D$ structural imaging of the whole inner retina. The combined analysis of these complex datasets has then required the development of novel multi-modal analysis methods, from which new retina models and computational vision algorithm have been designed.

Develop activity in the project

The final aim of my activity was to investigate the relationships between the functional class of RGCs and their morphology. To this end we developed tools (i) for the segmentation of a large population of neuronal cells; and (ii) for the automatic detection and segmentation of the dendritic arborization, at least of primary dendrites leaving from the cell, as the density of the processes becomes too high much before reaching the *Inner Plexiform Layer* (IPL, i.e. axons of bipolars and amacrines, dendrites of ganglion cells) and processes cannot be disentangled. The segmentation should be as precise as possible since we need then to extract morphological features/indexes characterizing cell and dendrites shape. To this end, in this thesis is presented the specific developed framework addressing all the steps of morphological analysis, from image pre-processing to the segmentation of cells and processes.

Selected images

Mouse retinal samples were imaged using Leica SP5 upright confocal microscope. Images were acquired at (sub)cellular resolution and at high averaging number to

reduce the noise level due to limited light penetration in deep layers of the tissue where RGCs are located.

For our studies, we chose a total of 5 images (2048 × 2048 and 1024 × 1024 pixels), containing some hundreds of cells, selected from 3 different retina samples including: i) three images coming from samples with genetic fluorescence expression, (i.e., $Im1$ from PV-EYFP and $Im2$ and $Im5$ images from Thy1-EYFP mouse), and ii) two images from samples with immunofluorescence staining using the Calretinin calcium-binding protein ($Im3$ and $Im4$) (Fig. 2.5 and Fig. 2.6). The samples were selected in order to best capture the variability in terms of fluorescence expression, cell and axonal bundle density and background.

2.3.2 Larva Drosophila

The second dataset analyzed is *Larva Drosophila* and includes volumes of some sensory neurons in the wild-type larva Drosophila studied over different development phases (see Fig.2.7, Fig. 2.8, Fig. 2.9, Fig. 2.10). This dataset is public and it is released by Prof. Tsechpenakis' lab [Gulyanon et al., 2015], [Gulyanon et al., 2016]. It is composed by 11 volumes of 1024x1024x20. They are representative of spatially inhomogeneous signal-to-noise ratios. All samples are prepared and imaged from the fruit fly type.

Larvae were mounted one per slide ($75 \times 25 \times 1mm$) in Halocarbon $1000N$ oil to match the refractive index of microscope objective oil-immersion fluid. Coverslips ($22 \times 22mm$) were secured using putty in order to apply appropriate pressure without popping the larva and to prevent larva movement while imaging. Larvae for all experiments were 48-72 hours old. The neurons used in imaging were on the distal left side along the larvae's dorsal end. Image stacks (.5 micron sections) of sensory neurons were detected with an inverse confocal laser scanning microscope (Zeiss LSM 780) using a Plan-Neofluar 40 × /1.30 Oil $M27$ objective (Zeiss) and the ZEN 2010 software.

In this dataset, neurons are imaged at the single scale but it happens that parts of dendrites of other neurons appear fluorescent in the same image.

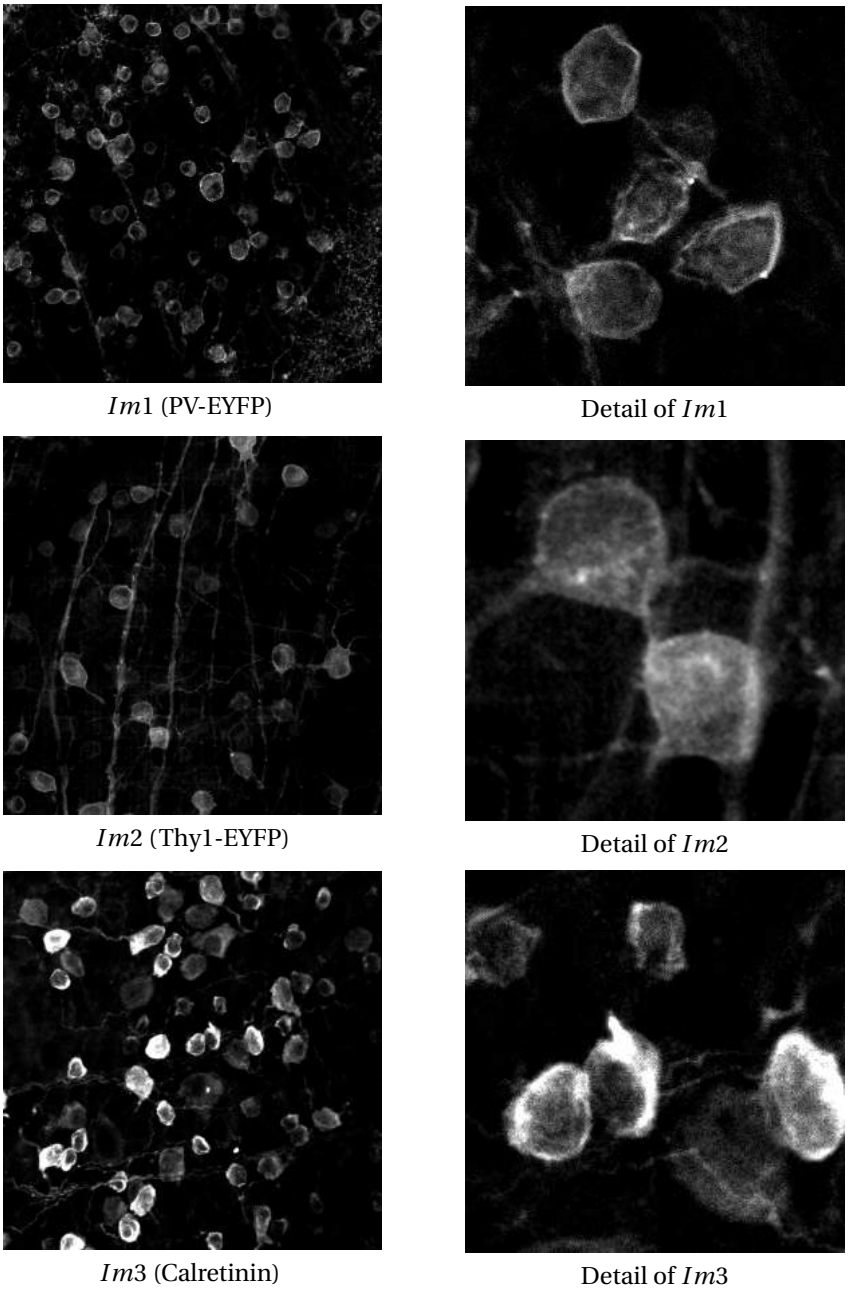

$Im1$ (PV-EYFP) Detail of $Im1$

$Im2$ (Thy1-EYFP) Detail of $Im2$

$Im3$ (Calretinin) Detail of $Im3$

Figure 2.5 – *Mouse Retina Dataset.* Images containing Retinal Ganglion Cells (RGCs) selected for testing the proposed method. The images show high variability across samples. While in the right column there are some magnified crops showing the complexity of images, on the left the correspondent images are visualized, where the analyzed structures are mixed with background and other structures.

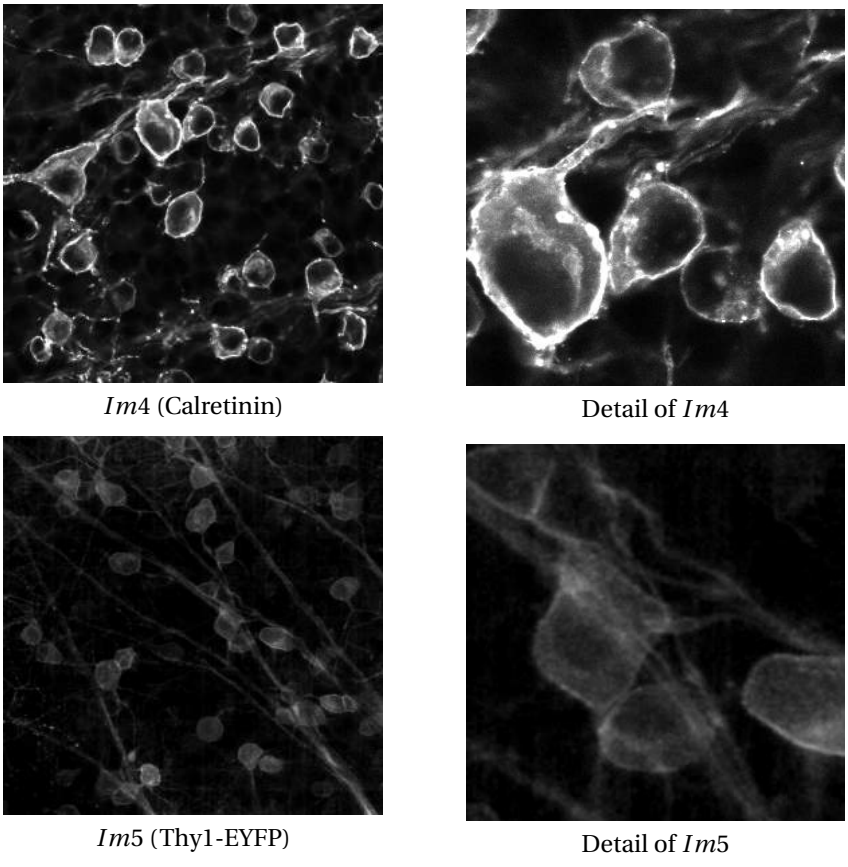

$Im4$ (Calretinin) Detail of $Im4$

$Im5$ (Thy1-EYFP) Detail of $Im5$

Figure 2.6 – *Mouse Retina Dataset.* Images containing Retinal Ganglion Cells (RGCs) selected for testing the proposed method. The images show high variability across samples. While in the right column there are some magnified crops showing the complexity of images, on the left the correspondent images are visualized, where the analyzed structures are mixed with background and other structures.

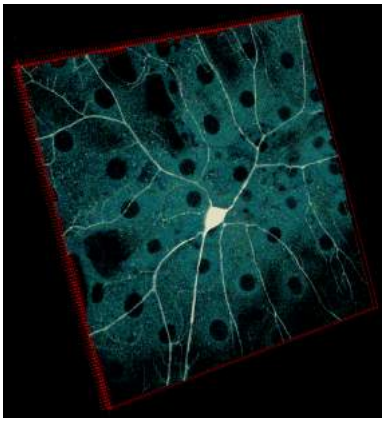

Sample #1

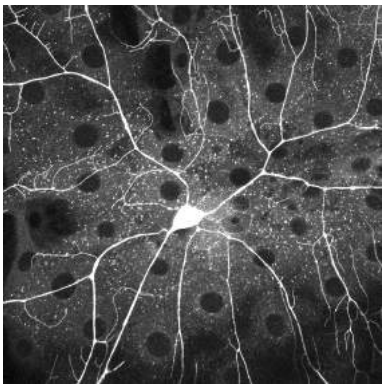

Maximum projection of Sample #1

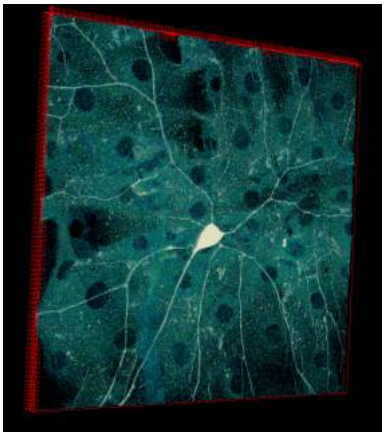

Sample #2

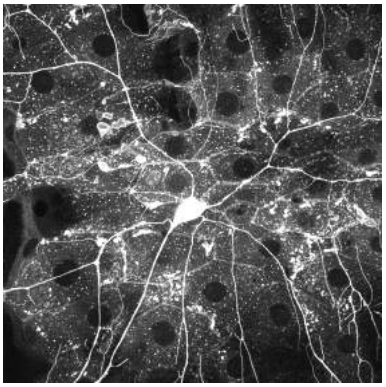

Maximum projection of Sample #2

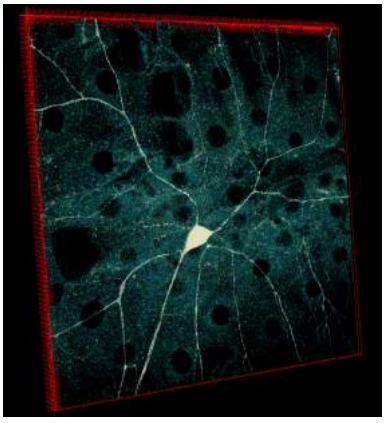

Sample #3

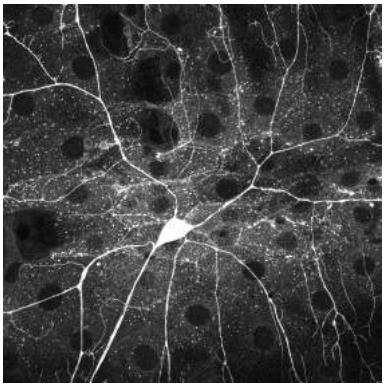

Maximum projection of Sample #3

Figure 2.7 – *Larva Drosophila Dataset.* Images contain some sensory neurons in wild-type Larva Drosophila studied over different development phases (each page contains a case study). Also in these case, images show heterogeneity across samples. While in the left column there are the sample volumes, on the left side the correspondent maximum projections are shown.

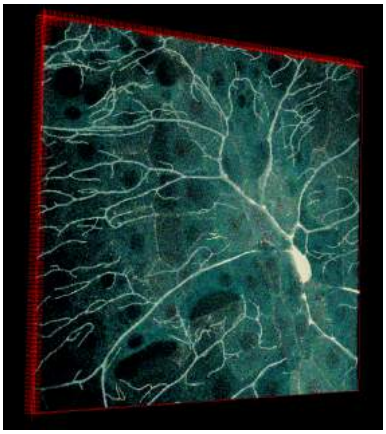

Sample #4

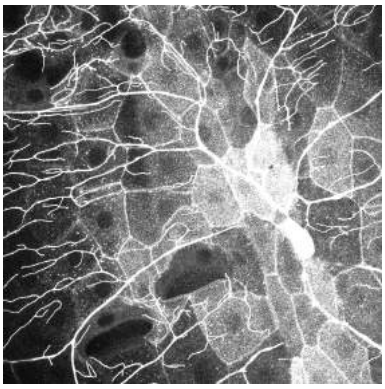

Maximum projection of Sample #4

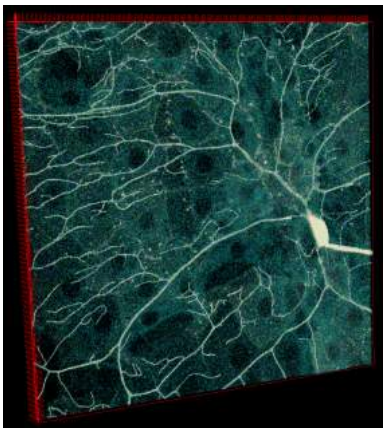

Sample #5

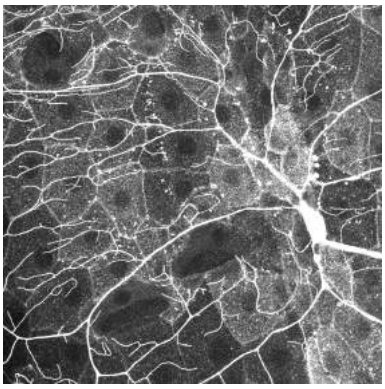

Maximum projection of Sample #5

Figure 2.8 – *Larva Drosophila Dataset.* Images contain some sensory neurons in wild-type Larva Drosophila studied over different development phases (each page contains a case study). Also in these case, images show heterogeneity across samples. While in the left column there are the sample volumes, on the left side the correspondent maximum projections are shown.

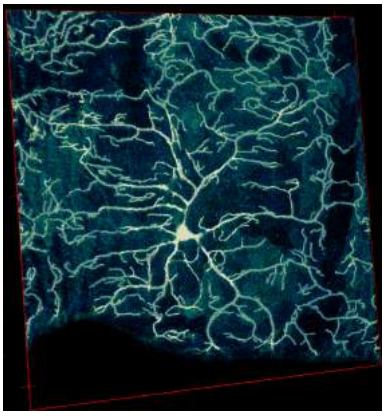

Sample #6

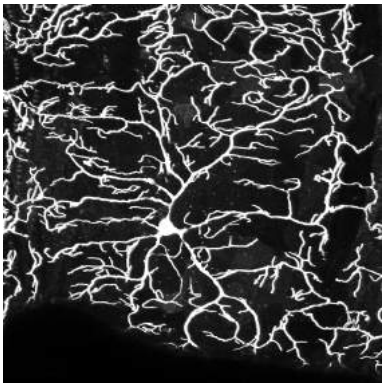

Maximum projection of Sample #6

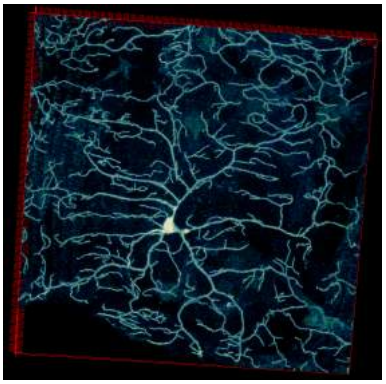

Sample #7

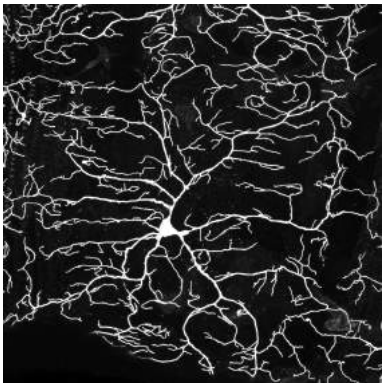

Maximum projection of Sample #7

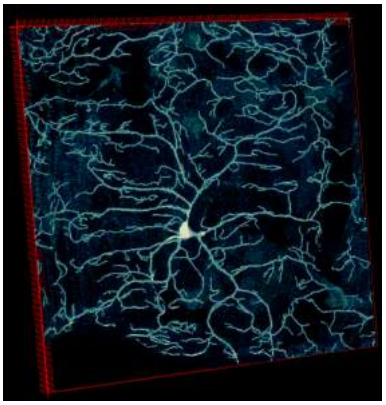

Sample #8

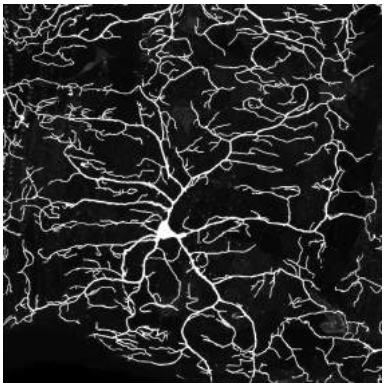

Maximum projection of Sample #8

Figure 2.9 – *Larva Drosophila Dataset.* Images contain some sensory neurons in wild-type Larva Drosophila studied over different development phases (each page contains a case study). Also in these case, images show heterogeneity across samples. While in the left column there are the sample volumes, on the left side the correspondent maximum projections are shown.

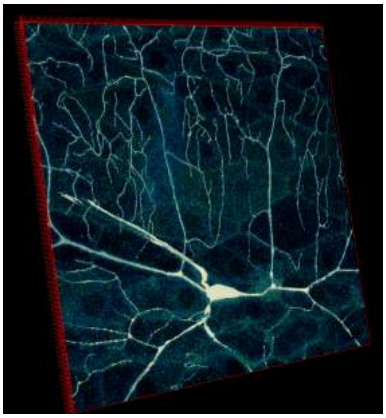

Sample #9

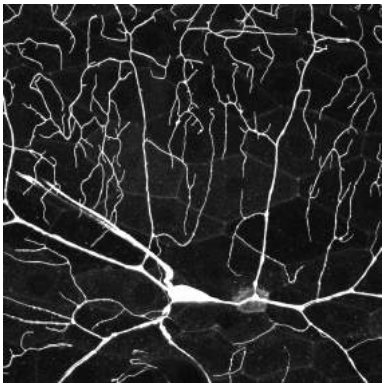

Maximum projection of Sample #9

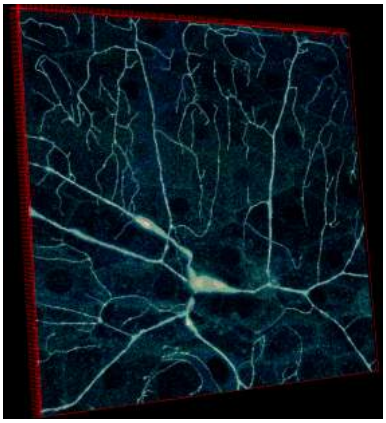

Sample #10

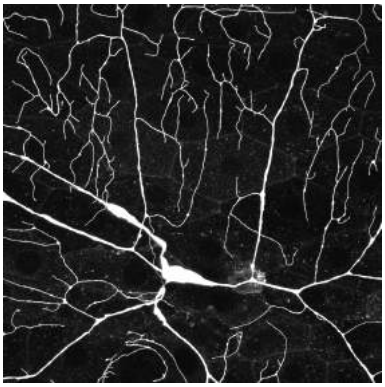

Maximum projection of Sample #10

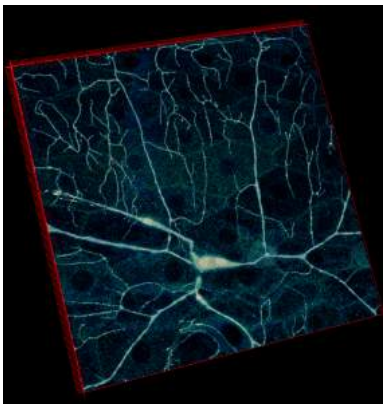

Sample #11

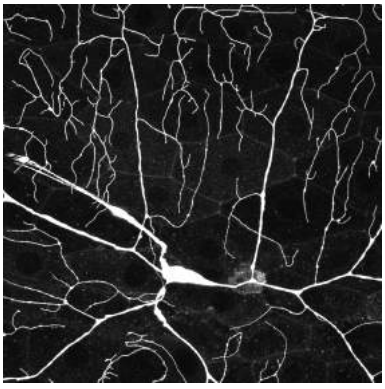

Maximum projection of Sample #11

Figure 2.10 – *Larva Drosophila Dataset.* Images contain some sensory neurons in wild-type Larva Drosophila studied over different development phases (each page contains a case study). Also in these case, images show heterogeneity across samples. While in the left column there are the sample volumes, on the left side the correspondent maximum projections are shown.

3 Soma morphology study: detection and segmentation

To reconstruct the whole neuron morphology, the automatic soma detection and segmentation is required. In this chapter, a combined technique for detecting and segmenting cell bodies in fluorescent microscopy images is presented. The method incorporates a novel blob enhancement filtering in order to select the specific cell shapes, an active contour process for precise border segmentation and a watershed transform step which separates single cell contours in possible grouped segmentations.

3.1 State of art

Analyzing the morphology of neuronal networks requires automatic tools that can detect and segment the neuron structures. The first step of this research would be identify and segment precisely cell bodies in order to accurately study and to classify neuron morphology. Cell segmentation approaches have been largely improved in the last decades, however they generally rely on images where labeling is limited to cell bodies. In our setting, the fluorescence is expressed by the entire neuron (including axon and dendrites)(see from Fig. 2.5 to Fig. 2.10). This opens new challenges from a computational perspective, because many structures are simultaneously labelled on the same channel. Detecting and segmenting neuron somas from these images requires an approach that can deal with a non-uniform fluorescence expression (typically limited to the cell nucleus or sometimes to cell membrane) that leads to fragmented appearance of the objects and to unreliable separation between somas, dendrites and axons. Plus, the algorithm should overcome a strong number of occlusions and background clutter. Last but not least, the method should not be sensible to the high variability of samples condition across different acquisitions.

This global setting introduces to new challenging computational tasks for image segmentation. Indeed, state-of-the-art methods usually work on single neuron reconstruction [Gulyanon et al., 2016] and can hardly be adequate for separating neurons from the background. The automated detection and segmentation is still a critical open problem. On the other hand, the manual interaction to generate the morphological reconstruction is time consuming and expensive. Traditional cell detection and segmentation approaches which use only basic techniques, such as morphological operators and thresholding, are not powerful enough and lead to wrong segmentations [Meijering, 2012]. Another alternative approach is to start from selected seed points in the image and to iteratively cluster connected points to form labeled regions [Frasconi et al., 2014]. Learning approaches, such as [Arteta et al., 2013] and [Zhang et al., 2014], require hand-labelled neurons for training and testing. In addition, they cannot manage to extract the precise segmentation of cells because of the difficulties dealing with the high variance in cell appearance. In contrast, active contour methods have demonstrated good performance in image segmentation dealing with challenging data [Chan et al., 2001], [Yezzi et al., 2002]. Their main limitation is related to the strong sensitivity to the model initialization, which usually requires variable degrees of user intervention. To this end, recent years have witnessed the spread of active contour models in different formulations, aiming at hybrid approaches for automating the initialization process [Ge et al., 2015], [Wu et al., 2015].

Within this scenario, we designed a method based on active contour initialized on specific ROIs, which are automatically identified by a multiscale blob filter emphasizing only cell bodies. Several shape-based enhancement filters have been introduced in literature. Frangi filter has been reported to be one of the most effective vessel enhancement filter [Frangi et al., 1998]. In light of that, we introduced a novel multiscale blob filtering method derived from the Frangi filter for the enhancement of neuron somata. Cell bodies are then segmented by a localizing region-based active contour algorithm [Lankton and Tannenbaum, 2008] followed by a watershed-based step to split groups of neurons and to separate cells from dendrites and axons.

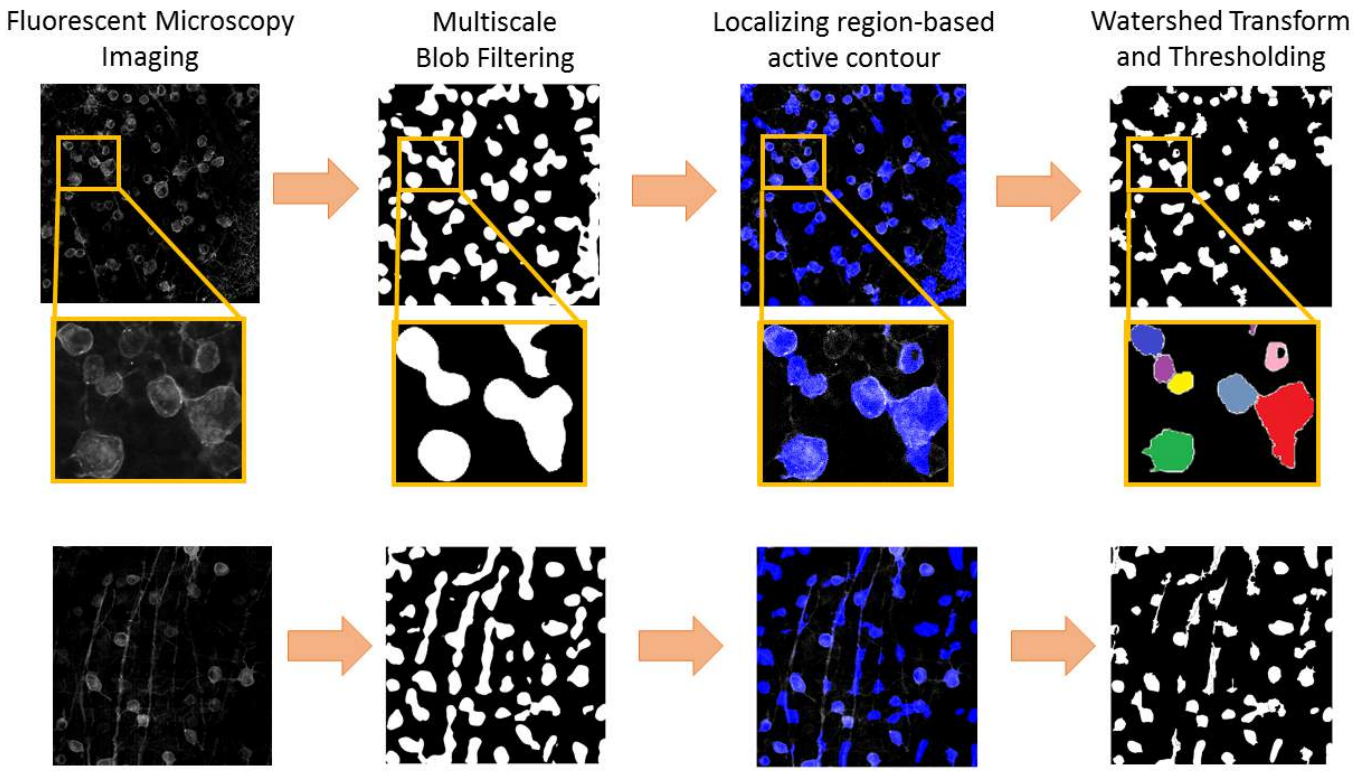

Figure 3.1 – Pipeline applied to two examples (from the top, $Im1$ (PV-EYFP) and $Im2$ (Thy1-EYFP)) with a crop in the central row, showing the difficulties caused by contiguous cells. In column, starting from the left side: Original Fluorescent Microscopy Images; Results of the multiscale blob filter after binarization; Results of the active contour segmentation in blue transparency over the original image for getting the suitable qualitative performance; Results of the watershed transform and of the final threshold.

3.2 Cell Detection : Multiscale Blob enhancement filtering

The aim of blob enhancement is to improve the intensity profile of neuron bodies and reduce the contribution of dendritic and axonal structures. It is based on the analysis of the eigenvalues of the Hessian matrix to determine the local likelihood that a pixel belongs to a cell, i.e. to a blob structure. The proposed approach is inspired by the work of Frangi et al. [Frangi et al., 1998] on multi-scale vessel enhancement filtering.

3.2.1 Frangi Filter

The Frangi filter essentially depends on the orientational difference or anisotropic distribution of the second-order derivatives to delineate tubular and filament-like structures. In this work, vessel enhancement is conceived as a filter searching for geometrical patterns which can be associated to a tubular structure. Plus, since vessels and dendrites have different scales in the same image, a multiscale approach is used. In order to study locally the behavior of the image L, a common method is to consider its Taylor expansion in the neighborhood of a point $\mathbf{x}_o$. Let's consider the second order expansion:

$$L(\mathbf{x}_o + \delta\mathbf{x}_o, s) \quad \approx \quad L(\mathbf{x}_o + s) + \delta\mathbf{x}_o^T \nabla_{o,s} + \delta\mathbf{x}_o^T \mathscr{H}_{x_o,s} \delta\mathbf{x}_o \tag{3.1}$$

where $\nabla_{o,s}$ is the gradient vector and $\mathscr{H}_{o,s}$ is the Hessian matrix of the image, both computed in $\mathbf{x}_o$ at scale s. Concerning the computation of the differential operators of L, in a well posed situation, it is used the linear scale space theory [Florack et al., 1992], [Koenderink, 1984]. According to this theory, differentiation is given by a convolution with Gaussian derivatives:

$$\frac{\partial}{\partial x} L(\mathbf{x}, s) \quad = \quad s^\gamma L(\mathbf{x}) * \frac{\partial}{\partial x} G(\mathbf{x}, s) \tag{3.2}$$

where the Gaussian function in D dimensions is:

$$G(\mathbf{x}, s) \quad = \quad \frac{1}{\sqrt{(2\pi s^2)^D}} \exp^{-\frac{\|\mathbf{x}\|^2}{2s^2}} \tag{3.3}$$

and where γ is a normalized parameter that has to guarantee fair comparison among the responses coming from different scales [Lindeberg, 1998]. The kernel generated by the second derivative at scale s measures the contrast between the areas inside and outside the range $(-s, s)$ in the direction of the derivative (Fig. 3.2).

Frangi's idea, as previously done in [Sato et al., 1997] and in [Lorenz et al., 1997], follows this observation.

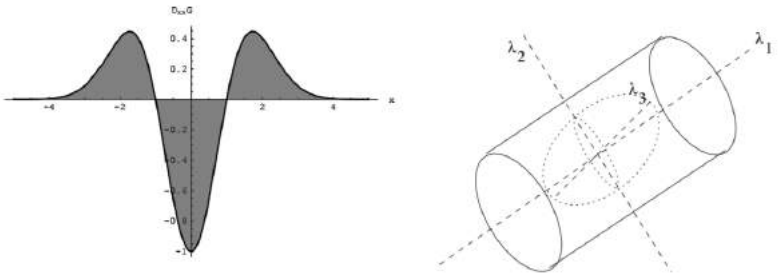

Figure 3.2 – *Figure on the left: Plot of the second order derivative of a Gaussian kernel. Figure on the right: The second order ellipsoid describes the principal direction locally.* Reprinted figure with courtesy of A. Frangi [Frangi et al., 1998]. ©1998 by Springer

The analysis of the Hessian eigenspace allows to extract the principal directions in which we can decompose locally the second order structure of the image. This is less expensive than the application of several multiple orientation filters.

Let $\lambda_{s,k}$ the eigenvalue corresponding to the k^{th} normalized eigenvector $\hat{\mathbf{u}}_{s,k}$ of the Hessian matrix $\mathscr{H}_{x_o,s}$, computed at the scale s. From the definition of eigenspace:

$$\mathscr{H}_{x_o,s}\hat{\mathbf{u}}_{s,k} = \lambda_{s,k}\hat{\mathbf{u}}_{s,k}$$

follows that:

$$\hat{\mathbf{u}}_{s,k}^{T}\mathscr{H}_{x_o,s}\hat{\mathbf{u}}_{s,k} = \lambda_{s,k}$$

From a geometrical interpretation, the eigenvector decomposition extracts three orthonormal directions that are invariant up to scale when mapped by Hessian matrix. These eigenvectors can represent axes of an ellipsoid that locally describes the second order image structure and can be used as an intuitive tool for the definition of geometric similarity measures.

In this thesis (note that this notation is different in [Frangi et al., 1998]), λ_k is the eigenvalue with the k^{th} biggest magnitude ($|\lambda_3| \leq |\lambda_2| \leq |\lambda_1|$).

2D		3D			Orientation Pattern
λ_1	λ_2	λ_1	λ_2	λ_3	
N	N	N	N	N	noisy, no prefferd direction
		$H-$	L	L	plate-like structure (bright)
		$H+$	L	L	plate-like structure (dark)
$H-$	L	$H-$	$H-$	L	tubular structure (bright)
$H+$	L	$H+$	$H+$	L	tubular structure (dark)
$H-$	$H-$	$H-$	$H-$	$H-$	blob-like structure (bright)
$H+$	$H+$	$H+$	$H+$	$H+$	blob-like structure (dark)

Table 3.1 – Possible patterns in $2D$ and in $3D$ according with the value of the eigenvalues λ_k (H = high, L = low, N = Noisy, + and − indicate the sign of the eigenvalue) and $|\lambda_3| \leq |\lambda_2| \leq |\lambda_1|$.

Table 3.1 shows the relations that have to been hold between eigenvalues of the Hessian for the detection of different structures. In particular, for an ideal tubular structure in a $3D$ image:

$$\begin{cases} |\lambda_3| \simeq 0 \\ |\lambda_3| \ll |\lambda_2| \\ \lambda_2 \simeq \lambda_1 \end{cases} \tag{3.4}$$

and the sign of λ_1 and λ_2 indicate its polarity.

In Frangi Filter all the three eigenvalues play a central role in the discrimination of the local pattern. This idea makes Frangi Filter different from the similarity measures proposed by [Sato et al., 1997] and [Lorenz et al., 1997] that only use λ_1 and λ_2 in the corresponding $3D$ vessel enhancement filters.

The Vesselness function computed in the point x_o proposed by Frangi is define as:

$$\mathcal{V}_s(x_o) = \begin{cases} 0 & \text{if } \lambda_1^{x_o} > 0 \\ (1 - exp\left(-\frac{\mathcal{R}_{\mathcal{A}}^2}{2\alpha^2}\right)) exp\left(-\frac{\mathcal{R}_{\mathcal{B}}^2}{2\beta^2}\right) (1 - exp\left(-\frac{\mathcal{S}^2}{2c^2}\right)) & \text{otherwise} \end{cases} \tag{3.5}$$

where $\mathcal{R}_{\mathcal{B}} = \frac{|\lambda_3^{x_o}|}{\sqrt{|\lambda_1^{x_o}||\lambda_2^{x_o}|}}$ is the blob-like component that can not distinguish between line- and plate-like patterns; $\mathcal{R}_{\mathcal{A}} = \frac{|\lambda_2^{x_o}|}{|\lambda_1^{x_o}|}$ is the contribution that can do that (in fact it will be zero in the case of plate-like pattern). Then, $\mathcal{S} = \|\mathcal{H}\|_F = \sqrt{\sum_{j \leq D} (\lambda_j^{x_o})^2}$, with D dimension of the image, is used to discard regions where the intensity variations

are small. Parameters α, β and c are thresholds which control the sensitivity of the filter.

The Vesselness measure in Eq. (3.5) is computed at different scales s. The response of the tubular filter will be maximum at a scale that approximately matches the size of the vessel to detect. Then the information at different scales is integrated in order to get the final vesselness estimation:

$$\mathcal{V}(x_o) = \max_{s_{min} \leq s \leq s_{max}} \mathcal{V}_s(x_o)$$

where s_{min} and s_{max} are the minimum and maximum scales at which structures are expected to be found.

For $2D$ case, the Vesselness measure becomes:

$$\mathcal{V}_s(x_o) = \begin{cases} 0 & \text{if } \lambda_1^{x_o} > 0 \\ exp\left(-\frac{\mathcal{R}_{\mathcal{B}}^2}{2\beta^2}\right)(1 - exp\left(-\frac{\mathcal{S}^2}{2c^2}\right)) & \text{otherwise} \end{cases} \tag{3.6}$$

where $\mathcal{R}_{\mathcal{B}} = \frac{\lambda_2^{x_o}}{\lambda_1^{x_o}}$ is the blobness measure in $2D$.

Note that Eq. (3.5) and (3.6) are defined for light structure enhancement. For the usage with dark objects, conditions (or images) should be inverted.

3.2.2 Multiscale Blob enhancement filtering

In this thesis, we start from Frangi's idea and modify the filtering process (in particular Equation 3.6) in order to have a reduction of line-like patterns in favor of blob-like structures (as [Liu et al., 2010]). Instead of a vesselness measure, we define a blobness measure as follows:

$$\mathcal{B}_s(x_o) = \begin{cases} 0, & \text{if } \lambda_1^{x_o} > 0 \\ e^{\frac{1}{2\beta^2} \cdot \left(\frac{\lambda_2^{x_o}}{\lambda_1^{x_o}}\right)^2}, & \text{otherwise} \end{cases} \tag{3.7}$$

where $\lambda_1^{x_o}$ and $\lambda_2^{x_o}$ are the eigenvalues of the Hessian matrix at point x_o and at scale s. β is a threshold which controls the sensitivity of the blob filter. Both β and the Hessian scale have been selected as the average neuron radius. Eq.(3.7) is given for bright structures over dark background. In case of dark objects conditions should be reversed.

The filter is computed at a multiscale level. The response of the blob filter would be maximum at scale s that more suited to the diameter of the blob to detect. Our *blob enhancement filtering* is said *multiscale* because we combine the blob measure at different scales to obtain a final blobness estimation defined as:

$$\mathscr{B}(x_o) = \max_{s_{min} \leq s \leq s_{max}} \mathscr{B}_s(x_o) \tag{3.8}$$

where s_{min} and s_{max} are the minimum and maximum scales where we expect to find structures.

This novel filter gives an image with values between 0 and 1 corresponding to the probability map that a specific pixel belong to a blob shape area.
This information is then binarized in order to get a binary mask for initializing the active contour method in the following step.

3.3 Cell Body Segmentation : Localizing Region-Based Active Contour

In order to study the cell morphology, a precise definition of soma contour and size is required. After blob enhancement filtering, we know where each cell is located. In fact, the information coming from the introduced filter corresponds to blob areas where with high probability there are neuron somas. Therefore, the probability map can be binarized and used as initialization ROIs for segmenting soma profiles. Segmentation can be performed in various ways as shown in Sec. 3.1. What follows provides a mathematical insight for the class of segmentation methods known as *active contours*.

Active contour methods have a growing success in recent years and have been applied in a range of fields including visual tracking and image segmentation [Blake and Isard, 1998], [Paragios et al., 2006]. Active contours are one class of variational methods that solve complex problems via optimization. In a variational approach, one must define a quantity or "energy" that will be at an optimum (maxima or minima) when a desirable solution is reached. Usually an energy is minimized by finding its first variation with respect to key arguments and iteratively reducing the energy by manipulating those arguments through gradient descent [Morel and Solimini, 2012]. In active contour algorithms, an energy functional is defined and its arguments contain the image to analyze and a closed curve that partitions the image. The energy is then minimized via iteratively deforming the contour by gradient descent. With a well-chosen energy, the curve will be stopped when a meaningful segmentation has been achieved.

3.3.1 Localizing Region-Based Active Contour

Localizing active contour [Lankton and Tannenbaum, 2008] is an improved version of traditional active contour models [Chan et al., 2001], [Yezzi et al., 2002]: objects characterized by heterogeneous statistics can be successfully segmented thanks to localized energies where the corresponding global ones would fail. This framework allows to remove the assumption that the foreground and background regions are distinguishable based on their global statistics. Indeed the working hypothesis is that interior and exterior regions of objects are locally different. Within this framework, the energies are constructed locally at each point along the curve in order to allow the analysis of local regions. The choice of the localization radius is driven by the size of the object to be segmented.

General formulation.

Let I be a given image defined in the domain Ω, and let Γ be a closed and regular curve defined as the zero level set of a signed distance function Φ, i.e. $\Gamma = \{x \in \mathbb{R}^D | \Phi(x) = 0\}$ with D dimension of domain Ω [Osher and Fedkiw, 2003], [Tsai et al., 2003]. The interior of the contour C is assigned by the smoothed version of the Heaviside function:

$$\mathscr{H}\Phi(x) = \begin{cases} 1, & \text{if } \Phi(x) < -\epsilon \\ 0, & \text{if } \Phi(x) > \epsilon \end{cases} \tag{3.9}$$

In a complementary definition, the exterior of C is $(1 - \mathscr{H}\Phi(x))$. In order to define the area around the contour, the derivative of $\mathscr{H}\Phi(x)$ is used. Then, the derivation result is a smoothed version of the δ of Dirac:

$$\delta\Phi(x) = \begin{cases} 1, & \text{if } \Phi(x) = 0 \\ 0, & \text{if } \|\Phi(x)\| > \epsilon \end{cases} \tag{3.10}$$

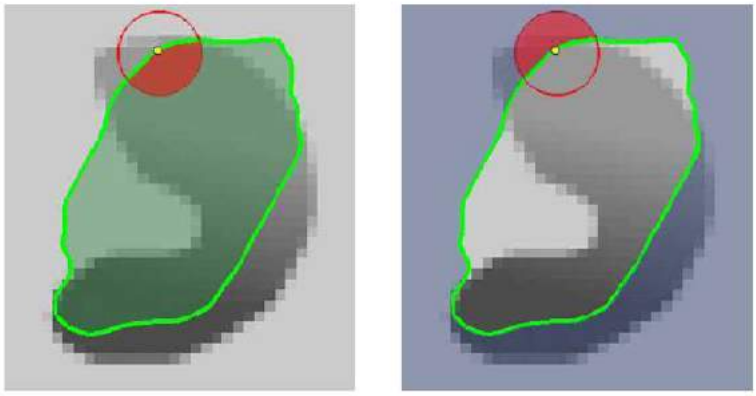

Figure 3.3 – Ball is considered at each point along the contour. This circle is split by the contour into local interior and local exterior regions. In both images, the point x is represented by the yellow small dot. The $\mathscr{B}(x, y)$ neighborhood is represented by the larger red circle. In (a), the local interior is the shaded part of the circle and in (b), the shaded part of the circle indicates the local exterior. Reprinted figure with courtesy of S. Lankton [Lankton and Tannenbaum, 2008]. ©2008 by IEEE

Given x and y independent spatial variables representing two different single points in the domain, let define the characteristic function dependent on the radius r:

$$\mathscr{B}(x,y) = \begin{cases} 1, & \|x-y\| < r \\ 0, & \text{otherwise} \end{cases} \tag{3.11}$$

$\mathscr{B}(x,y)$ is a spherical mask and it is 1 when y is in within the ball of radius r and centre x and 0 outside. Fig. 3.3 shows how this ball $\mathscr{B}(x,y)$ plays on the contour. This equation (3.11) is then used for localizing the energy functional defined in term of a generic force function F:

$$E(\Phi) = \int_{\Omega_x} \delta\Phi(x) \int_{\Omega_y} \mathscr{B}(x,y) \cdot F(I(y),\Phi(y)) dy dx \tag{3.12}$$

In equation (3.12), F is an internal energy function representing local adherence to a given structure at each point along the contour Γ. For each point x given by $\delta\Phi(x)$, the computation of E is masked by $\mathscr{B}(x,y)$ in order to ensure that F is applied only on local information of the image in x. Hence, the first term final contribution of the energy E is the sum of F values given by $\mathscr{B}(x,y)$ neighborhood along the zero level set.

Then, for keeping the curve smooth, a regularization term is usually added. This term penalized the curve arclength and weight this quantity by a parameter λ. The energy is now given as:

$$E(\Phi) = \int_{\Omega_x} \delta\Phi(x) \int_{\Omega_y} \mathscr{B}(x,y) \cdot F(I(y),\Phi(y)) dy dx + \lambda \int_{\Omega_x} \delta\Phi(x) \|\nabla\Phi(x)\| dx \tag{3.13}$$

The evolution equation is given by the first variation of the energy E respect to Φ:

$$\frac{\partial\Phi}{\partial t}(x) = \delta\Phi(x) = \int_{\Omega_y} \mathscr{B}(x,y) \cdot \nabla_{\Phi(y)} F(I(y),\Phi(y)) dy + \lambda\delta\Phi(x) div\Big(\frac{\nabla\Phi(x)}{|\nabla\Phi(x)|}\Big) \tag{3.14}$$

The only request about the internal energy function F is that the first variation with respect to Φ can be computed. This is necessary in order to ensure that all region-based segmentation can be calculated within this framework. In this way, all global energies (as for example in [Chan et al., 2001], [Yezzi et al., 2002]) can be localized and improved by this method by Lankton [Lankton and Tannenbaum, 2008].

Implementation details.

Since now, the formulation is defined in a general energy overview. In this thesis, the adopted energy is the Mean Separation (MS) Energy, introduced in [Yezzi et al., 2002] and localized as in [Lankton and Tannenbaum, 2008].
Concerning the radius of the ball function $\mathscr{B}(x, y)$, this parameter choice is important and it is determined on how local the segmentation has to be. In particular, its scale should be on the same scale of the object to be segmented and depending on the surrounding background pattern.

In our case, for each image, we used a radius equal to the average soma radius, depending on the image size and on the microscope lens. Thanks to this efficient technique, we obtain a segmentation mask which tightly fits real cell bodies.
In some situations, where cells are contiguous and there are occlusions and unreliable separations (Fig. 3.5), active contour approach can segment a group of cells as a unique entities. A further step is required to split them.

3.4 Watershed Transform and Size Filter

To separate groups of overlapping or contiguous cells, we exploit the simplicity and computational speed of the watershed transform, introduced by Beucher and Lantuéjoul [Beucher and Lantuéjoul, 1979].

The watershed algorithm detects catchment basins of all minima in the image. Consider the image I in three dimensions: I can be represented as two spatial coordinates versus intensity [Gonzalez and Woods, 2001]. In such "topographic" interpretation, we suppose that a hole is located in each regional minimum and that the entire topography is flooded from below by letting water rise through the holes at a uniform rate. When water coming from different catchment basins is about to merge, a dam is built to avoid the merging. These dams are the (connected) boundaries extracted by a watershed transform algorithm (Fig. 3.4).

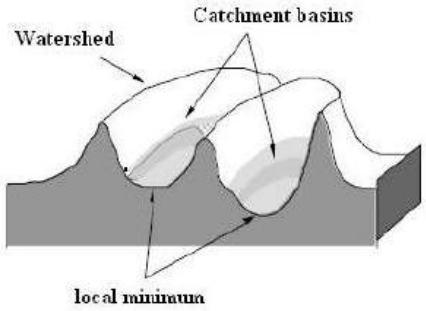

Figure 3.4 – Modelling of contours by watershed transform: the watersheds are the zones dividing adjacent catchment basins.Reprinted figure with courtesy of A. El Allaoui [El Allaoui et al., 2012] ©2012 by AIRCC.

Implementation details.

In our case , we applied watershed transform to the single connected components, segmented after the active contour step. This would lead to the extraction of single cell segmentation when occlusions and fuzzy boundaries drive AC model to the wrong and grouped segmentation (see Fig. 3.5).

As a final step, we delete components which are too small or too large for being cell bodies (an example is given in Fig.3.1, first line) applying a size filter to remove structures with size outside an acceptable range of soma dimensions. It is possible to fix this range by a statistical analysis of cell dimensions removing the tails of the distribution.

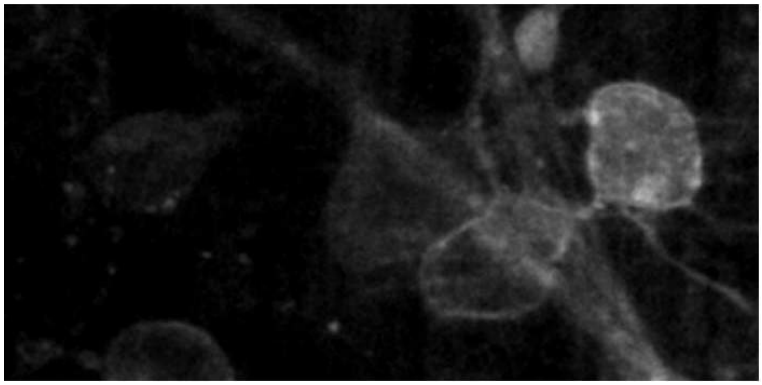

Crop of $Im5$

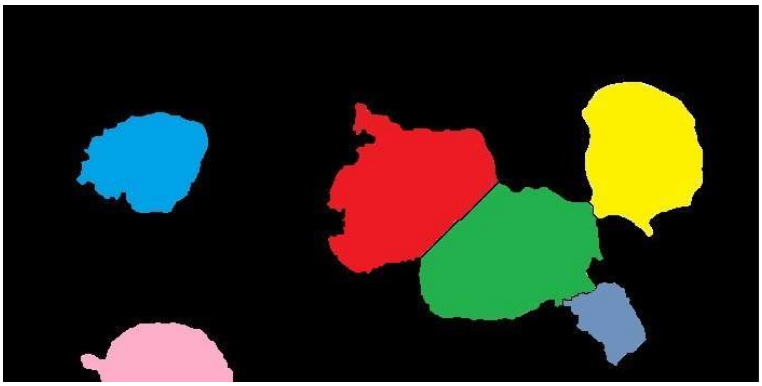

Resulted Crop Segmentation

Figure 3.5 – Some cells are not easily visible to the human eye just visualizing the retina images, but they are discovered and segmented by our algorithm (for example, in this cropped figure, pink and blue cells were hardly detectable). Adding contrast to the image makes these somata clearer but it increases noise and cell heterogeneity.

3.5 Results and Discussion

For the evaluation of soma detection and segmentation, we applied our pipeline to two different datasets, *Mouse Retina* [Baglietto et al., 2017a] and *Larva Drosophila* [Gulyanon et al., 2016].

As previously described in Chapter 2, Sec. 2.3, the first dataset, *Mouse Retina*, is composed of 5 different retinal images representative of possible variations on the retinal samples, such as brightness, intensity, size and number of cells, presence of axonal structures and processes, strong background signals, etc. These samples show images at the network scale of many dozens of RGCs with higher fluorescence expression into the soma. The ground truth have been generated manually segmenting all cells in each image (around 280 cells in total).
The second dataset, *Larva Drosophila* contains fluorescent images made of 11 single neurons representative of spatially inhomogeneous signal-to-noise ratios. Also in this case, all the neurons (both soma and dendrites) have been manually segmented.

To give a qualitative evaluation, we report different examples of *Mouse Retina* in Fig.3.1-3.5 and of *Larva Drosophila* in Fig. 4.3 (central column) where it is possible to see that our approach works in different sample conditions.

To quantify the performance of our method, we adopt the Dice Coefficient (DC), a widely used overlapped metric for comparing two segmentation. DC is defined as follows:

$$DC = \frac{2(A \cap B)}{(A + B)},$$

where A is the binary ground truth mask and B is the binary segmentation result. The DC value ranges between 0 (absence of agreement) and 1 (perfect agreement). A DC higher than 0.70 usually corresponds to a satisfactory segmentation [Zijdenbos et al., 1994].

Table 3.2 shows the quantitative results on our *Mouse Retina* samples. We compute the DC for each of the three steps in the pipeline (Blob-based Filtering after binarization, Active Contour and Watershed Transform). Each stage clearly improves the segmentation, reaching satisfactory results for all images. In $Im3$ (Fig. 2.5), the fluorescence is mainly expressed by the body cells; for this reason, we reach good scores right after the first two steps. The weaker DC values on images $Im2$ and $Im5$ are due to a strong presence of axonal structures which can be hardly removed. As an additional index of performance at the network scale, we also present the percentage of detected cells for each *Mouse Retina* image. Fig.3.6 shows the variation

Image	# of cells	Blob Filter DC	Active Contour DC	Final DC	Final detected cells
$Im1$ (PV-EYFP)	95	0.60	0.69	0.81	86.32%
$Im2$ (Thy1-EYFP)	37	0.43	0.58	0.64	89.19%
$Im3$ (Calretinin)	64	0.62	0.82	0.83	75.00%
$Im4$ (Calretinin)	29	0.57	0.71	0.79	82.76%
$Im5$ (Thy1-EYFP)	48	0.51	0.62	0.70	85.42%

Table 3.2 – Results for soma segmentation on *Mouse Retina* samples. Dice Coefficient is computed for all steps in the pipeline (Blob Filter, Active Contour and Watershed Transform) and it shows improvements after each step. For the final stage of the pipeline, there is also the percentage of detected cells computed assuming as detected a cell with minimum overlap 50% with ground truth fixed at 50%.

of the percentage of detected cells at different thresholds of overlapping between computer-aided segmentation with the ground truth to count a cell as detected. It can be observed that 50% threshold is a good trade off between the certainty of a cell detection and a satisfactory retrieval. So, in Table 3.2, we consider a cell as detected if it is correctly segmented for more than 50% of its total area, comparing the segmentation mask to the ground truth for each annotated RGC.

Table 3.3 reports the quantitative evaluation on the *Larva Drosophila* dataset. In this case, we compute the DC and the Jaccard Index (JI). Jaccard Index [Jaccard, 1901] is another overlap ratio measure and it is defined as follows:

$$JI = \frac{|A \cap B|}{|A \cup B|}$$

The DC is currently more popular than the Jaccard overlap ratio [Crum et al., 2006]. This is because JI is numerically more sensitive to mismatch when there is reasonably strong overlap (as we can observe in the results in Tab. 3.3). Worst values are obtained for Sample #4 (Fig. 2.8) and #6 (Fig. 2.9), where background noise is strong and leads to confusing borders. In general, however, the values are significantly high with an avarage reaching respectively, 0.88 and 0.80.

Part of this work is published in [Baglietto et al., 2017a] and in the journal paper under review [Baglietto et al., subm].

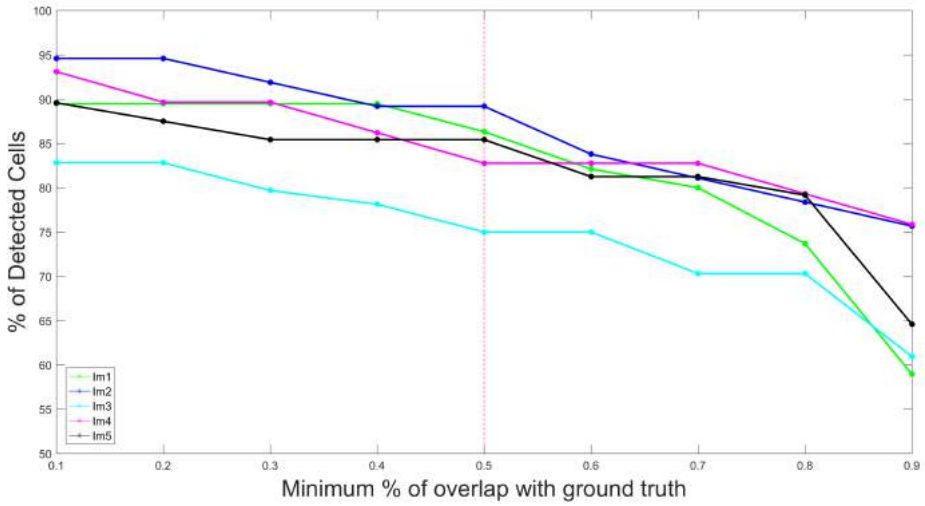

Figure 3.6 – Variation of the % of detected cells in *Mouse Retina* dataset as a function of the % threshold of overlap between detected cell and the corresponding annotated ground truth.

Image	DC	JI
#1	0.89	0.80
#2	0.95	0.90
#3	0.97	0.95
#4	0.74	0.59
#5	0.94	0.89
#6	0.69	0.53
#7	0.93	0.87
#8	0.91	0.83
#9	0.83	0.70
#10	0.89	0.80
#11	0.92	0.85
Avarage	0.88	0.80

Table 3.3 – Soma segmentation results on *Larva Drosophila* dataset. Dice Coefficient has been computed for each segmented soma.

4 Dendrite Tracing

In this Chapter, it is described our original research contribution on dendrite segmentation. When combined with our work described in Chapter 3, our method allows to automatically segment the entirety of a neuron, from soma to arborization tree. In Section 4.1 a state of art about dendrite tracing is presented. Section 4.2 and Section 4.3 show our proposal respectively dealing with $2D$ and with $3D$ acquisitions.

4.1 State of Art

Thanks to the great advances in cellular imaging and microscopy acquisition, we have technological tools and techniques allowing to address fundamental questions in neuron studies: we can capture high-resolution $2D$ and $3D$ images of single neurons and of populations that enable neurobiologists to investigate the neuronal structure and the morphological development associated to neurological disorders. In the previous Chapter, a solution for the detection and segmentation of neuron bodies is presented. The second step aims now at the dendritic arborization tracing to complete the whole neuron reconstruction.

Neuron samples acquired by a confocal microscopy are complex for different reasons. First of all, the dendrites appear as thin filaments or tubular structures and the arbors are large and extremely intricate. They are affected by low contrast at the neuron boundaries and the dendritic tree varies across different samples and acquisitions. Indeed, the fluorescence expressed in neuron volumes is non-uniform. It has higher value into the soma and presenting lower signal in the rest of the neuron structure. This leads to fragmentation and gaps into dendrite appearance. Finally, there is a high variability of samples condition on different microscopic acquisitions.

Neuron segmentation problem has been investigated since the beginning of the $'80s$ [Reuman and Capowski, 1984], when manual segmentation was the first solution and it was so infeasible. Since that period, a large number of approaches have been studied and described in literature. There are a lot of works in this field [Meijering, 2010], [Basu et al., 2010], [Mukherjee et al., 2015], [Longair et al., 2011]. Despite the increasing amount of studies, the state of art is not still satisfactory. For example, the manual interaction that some tools require [Longair et al., 2011] is time consuming, expensive and extremely depending on the user diligence and personal expertise.

Traditional segmentation approaches that use basic method such as thresholding and morphological operators are not precise enough and lead to wrong segmentations. Learning approaches, nowadays broadly used in object segmentation, including high-performance deep learning methods, are not suitable for these images because they require a huge amount of hand-labeled neuron samples for training and testing [Zheng and Hong, 2016].

Skeletonization is a global technique that extract the binary skeleton from a given neuronal structure [Lee et al., 1994], [Palágyi and Kuba, 1998]. The key idea of these methods is an iterative erasure of voxels from the volume of the segmented object preserving the topology of the contained structure. Minimal path based tracing are other global approaches and aim at linking seed points by an optimization problem [Meijering et al., 2003] or by Fast Marching algorithm [Benmansour and Cohen, 2011]. Minimum Spanning Tree (MST) tracing deals with the link between detected points into a tree representation [Türetken et al., 2011].

Among deformable models, active contour models have demonstrated good performance in segmentation even when applied to challenging data [Chan et al., 2001], [Yezzi et al., 2002]. Their main issue is the high sensitivity to the initialization, which often requires user setting. To this aim, recent active contour models propose an hybrid approach to automate the initial mask [Ge et al., 2015], [Wu et al., 2015].

Our first contribution to dendrite tracing is proposed in $2D$ dimensions. In this framework, a novel level set exploiting local phase and Hessian information is used to segment the whole neuron starting from the soma segmentation obtained by the approach presented in Chapter 3.
Then, our interest is moved to the $3D$ datasets and a series of models and methods have been studied and tested to perform a volume reconstruction of neurons. The main idea is on the fact that, computing the Hessian Matrix, the principal structure direction can be extracted. Following this information, the whole process can be traced.

4.2 Dendrite Segmentation in 2D

In this part of the thesis, level set propagation with local phase and with Hessian eigenspace information is used to segment the whole dendrite arborization, once the neuron body is detected and segmented by pipeline presented in Chapter 3. The main idea is that local phase is extracted using quadrature filters and this allows to distinguish lines and edges in a image [Lathen et al., 2008], [Läthén et al., 2010]. In our case study, a dendrite can appear as a line or as an edge pair, depending on the scale on which they are observed; then a multiple scale integration is useful for capturing information about dendrites of varying width and contrast. Our novel idea is weighting this filter by the Hessian eigenspace that guarantees that only pixel belonging to structures contributes [Frangi et al., 1998] (see Chapter 3 Sec. 3.2.1). The result is a "local" filter which can drive a contour towards the dendrite arborization.

4.2.1 Quadrature filters

In signal processing, a quadrature filter is defined as a zero function in the Fourier domain by

$$F_k(\mathbf{u}) = 0, \qquad \mathbf{u} \cdot \mathbf{n_k} \leq 0$$

where $\mathbf{u}$ is the frequency and $\mathbf{n_k}$ the filter direction. In other words, the filter is zero over one half of the Fourier domain [Derpanis, 2005]. In the spatial domain, the filter is defined as a complex filter pair: the real part is a line filter and the imaginary part is an edge filter [Granlund and Knutsson, 2013]. For this reason, when the filter finds a line-like pattern its response is mostly real, while any edge matching will give a dominantly imaginary response (Fig. 4.1(a)-(b)). Thus, the type of structure (line/edge) can be indicated by the argument θ of the complex response, as indicated in Fig. 4.1(c). θ is typically indicated as the *local phase*. Moreover, the response magnitude defines the strength of the structure and the angle θ indicates the structure type (line/edge). This line/edge detector is invariant to image contrast because the angle θ is independent of signal strength. So it becomes a more robust alternative to edge detectors based on gradients.

Combining filter directions

In $2D$ and $3D$ images, the filter kernel is usually applied in three and six uniformly distributed directions respectively. Thus, the local phase produces different responses along the different directions. In order to get an orientation invariant phase map, the filter values along different directions need to be combined. The solution is

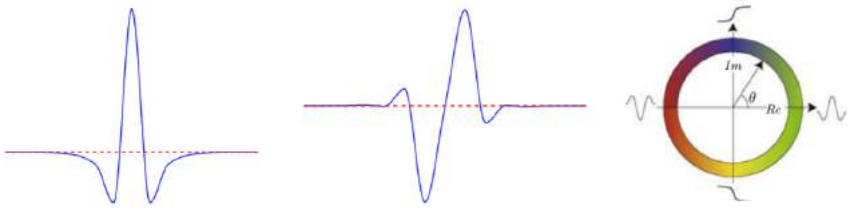

(a) Line filter (b) Edge filter (c) Local phase

Figure 4.1 – Components of the quadrature filter - Reprinted figure with courtesy of G. *Läthén* [Läthén et al., 2010]©2010 by Elsevier

computing the orientation of the dominant structure at each point, and flip the phase along the real axis for a filter with direction opposing the orientation. In practice, this produce the same phase result for an edge independent of filter direction. Solved this ambiguity, we can produce an orientation invariant phase map by making a sum of the filter responses for all directions.

Multi-scale integration

As we have already observed in the previous Chapter 3, our problem present an high variability of samples, acquisitions and conditions. Moreover in the same image there are neurons of different sizes and scales. So, our approach uses the common idea of multi-scale filtering to handle dendrite of varying width. Within this framework, different scales are combined for getting a local phase used for segmentation step. The formulation of this idea is a weighted sum over all scales:

$$q = \frac{\sum_{i=1}^{N} |q_i|^{\beta} q_i}{\sum_{i=1}^{N} |q_i|^{\beta}} \tag{4.1}$$

where N is the number of scales, q_i is the phase map for each scale and β is a weight parameter. As a final preprocessing step, a normalization step is applied to the output magnitude:

$$\hat{q}(\sigma) = 1/(1 + (\sigma/|q|)^2) \tag{4.2}$$

where q is the local phase function and σ is a data dependent threshold parameter. With this normalization, scaling issues associated to different inputs are removed.

4.2.2 Segmentation

Given the filter response on our image, we use the observation that the local phase of $\pi/2$ corresponds to edge structures. Hence, the main idea is to consider only the real part of the response. At the same time, positive and negative values are respectively found inside and outside the line structures and edge information come from the zero-crossing. Then, the segmentation of the dendrites can be done extracting the zero level set from the real part of the phase map. As done in [Lathen et al., 2008], we use the level set method as [Osher and Sethian, 1988] as means for front propagation. Relating to our phase based edge detector, the idea is to extract the real part of the phase map as a *speed function* driving a deforming contour. As presented in Equation 3.13 in Chapter 3, it is usually added a regularization term based on the curvature. The resulted evolving equation is:

$$\frac{\partial \Phi}{\partial t} = -Re(\hat{q}(\sigma))\,|\nabla\Phi| + \alpha k|\nabla\Phi| \tag{4.3}$$

where $\hat{q}$ is the normalized phase function by Eq. 4.2, α is a regularizer and k is the mean curvature.

In order to enforce the computation in proximity of structures, we introduce an improvement in the formulation of the evolving equation:

$$\frac{\partial \Phi}{\partial t} = -|\lambda_1| \quad Re(\hat{q}(\sigma))\,|\nabla\Phi| + \alpha k|\nabla\Phi| \tag{4.4}$$

where λ_1 is the first eigenvalue computed in each pixel by the Hessian Matrix. With this contribution, the background signal is omitted and λ_1 drives the level set only where the pixels belong to a structure (Fig. 4.2). The result is a "local" filter which can drive a contour towards the dendrite arborization (see Fig. 4.4).
The Hessian Matrix in $2D$ finds two eigenvalues : $\lambda 1$ and $\lambda 2$. It can be noticed (both in the example in Fig. 4.2 and in the results in Table 4.1) that the contribution of the second eigenvalue λ_2 does not add good information but noise.

4.2.3 Results and Discussion in 2D framework

For the dendrite segmentation in $2D$ presented in this Section, we implemented the proposed method in Matlab. We initialize the level set contour with the segmented somas (following the proposed pipeline in Chapter 3) and executed the segmentation by level set until covergence, which was defined as the total difference in the contour changing less than 25 pixels between two following time-steps.

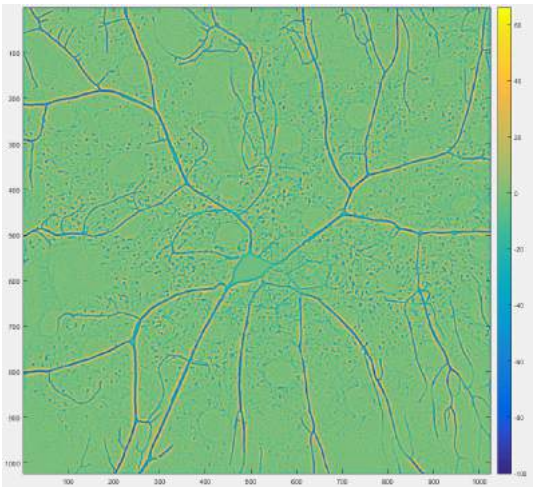

λ_1

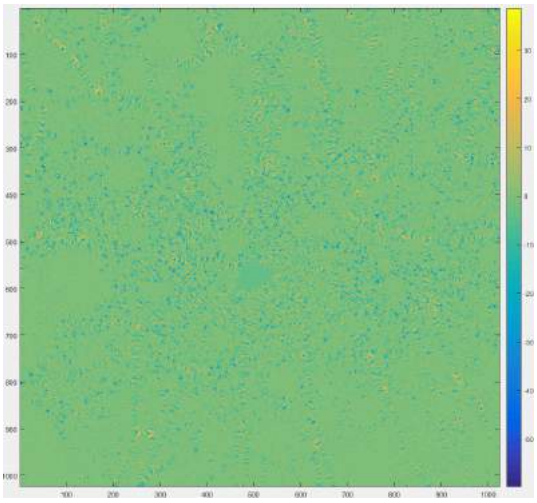

λ_2

Figure 4.2 – Example of the eigenvalues computed on a image from the dataset. It can be observed that λ_1 brings information on the presence of a strucuture.

For the experimental part, we use *Larva Drosophila* dataset that contains images with the complete dendritic tree labeled for each neuron. Sample neuronal cells are rendered in $2D$ by maximum intensity projection of slices of the original $3D$ fluorescence microscopy image stacks. For the dendritic ground-truth segmentation, we adopted the tool Simple Neurite Tracer [Longair et al., 2011].

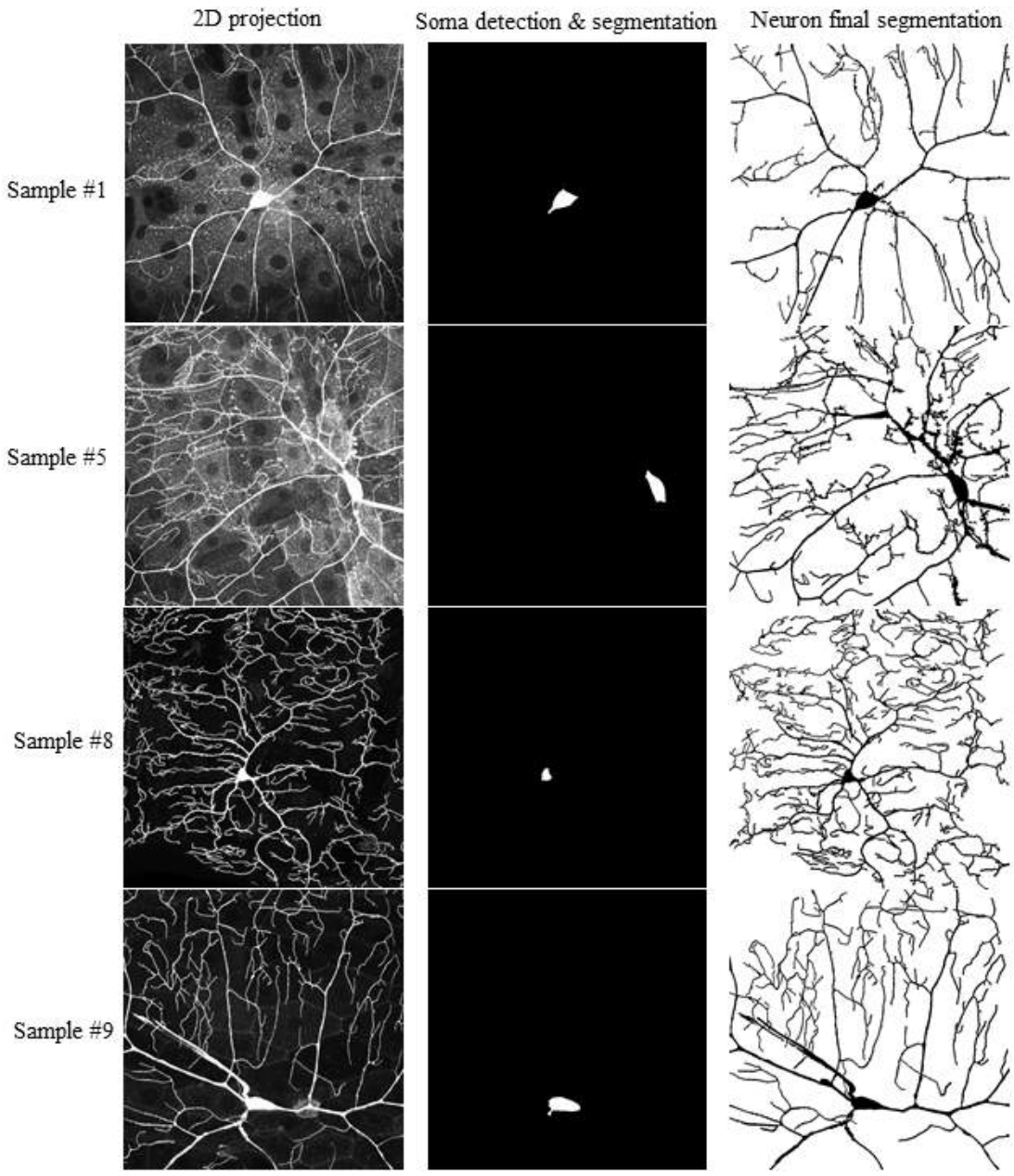

Figure 4.3 – Some example images from *Larva Drosophila* dataset. In column, from the left side: $2D$ maximum intensity projection of the original volume; soma detection and segmentation applying the first part of the proposed approach (Chap. 3); whole neuron segmentation including dendrites.

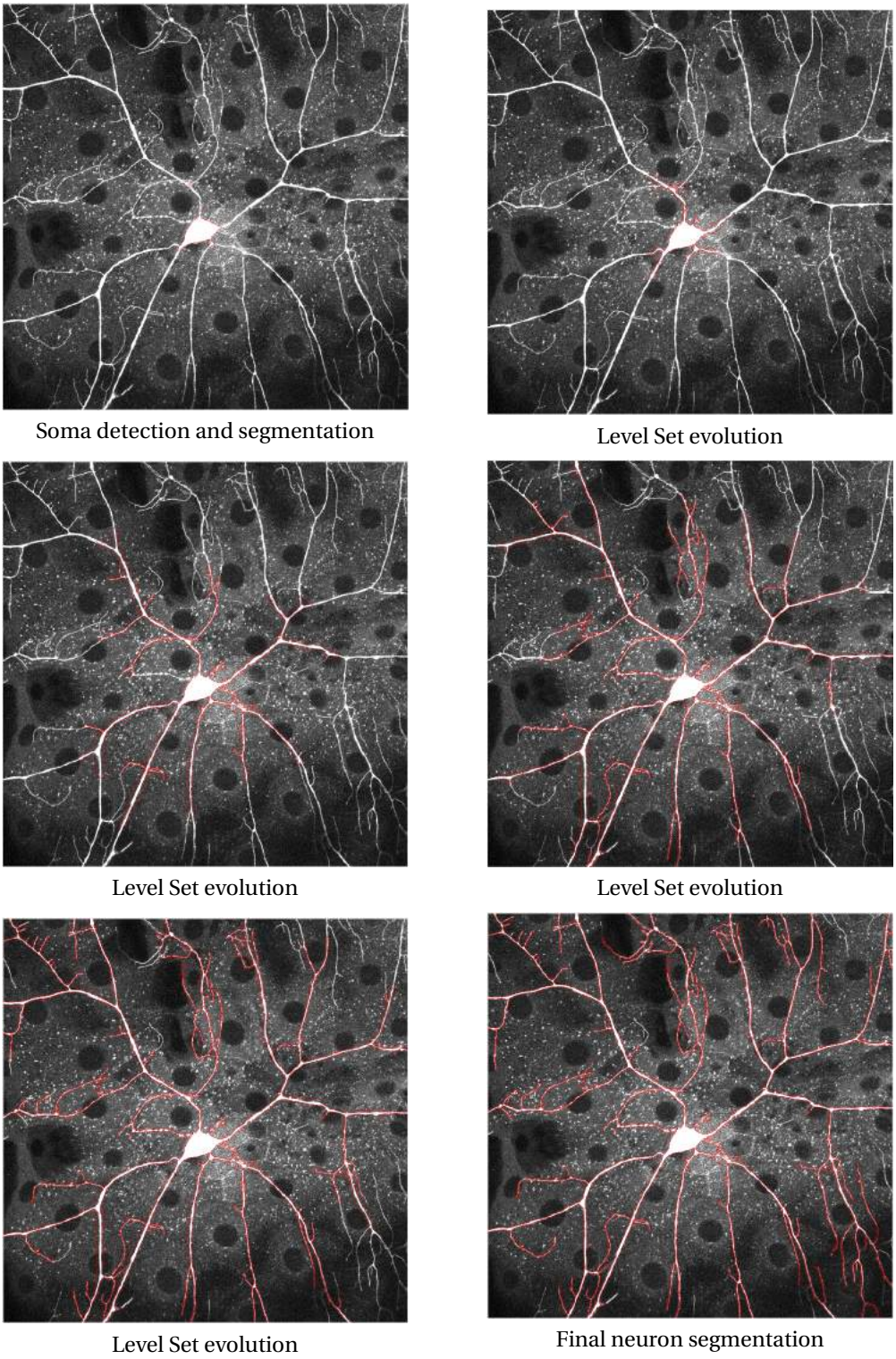

Figure 4.4 – An example of the level set evolution starting from the soma segmentation as seed point. The level set is shown at different evolution steps.

A qualitative evaluation of the dendrite segmentation starting from seed soma is shown in Fig. 4.4 (bottom right) and in Fig. 4.3. In particular Fig. 4.4 shows an example of level set initialization, its evolution and the result; Fig. 4.3 proposes some *Larva Drosophila* image results after the first part of the segmentation process (i.e. cell segmentation, middle column) and at the final segmentation (column on the right side).

To quantitatively evaluate our neuron segmentation, we compare our method with a recent state-of-the-art automated approach proposed in [Mukherjee et al., 2015], Tubularity Flow Field (*Tuff*) . *Tuff* is a technique for automatic neuron segmentation that performs directional regional growing guided by the tubularity direction of neurites. Among the state-of-the-art tools, we decide to compare our segmentation with *Tuff* because it is completely automated (the only one fully automatic among methods introduced in Sec. 1.3) and it does not require any user intervention or manual adjustment, as our method aims to. We compute the DC (measure presented in Sec. 3.5) on *Larva Drosophila* results for both methods (see Table 4.2) and it can be observed that our method significantly outperform *Tuff*.

Part of this work is in the journal paper under review [Baglietto et al., subm].

	DC	
Volume	λ_1	$\lambda_1 + \lambda_2$
#1	0.82	0.75
#2	0.71	0.74
#3	0.78	0.57
#4	0.71	0.71
#5	0.80	0.80
#6	0.91	0.91
#7	0.86	0.86
#8	0.86	0.86
#9	0.88	0.88
#10	0.83	0.83
#11	0.85	0.82
Avarage	0.82	0.79

Table 4.1 – Dice Coefficient has been computed comparing segmentation with λ_1 and $\lambda_1 + \lambda_2$ contributions.

	DC	
Volume	Our method	Tuff
#1	0.82	0.51
#2	0.71	0.39
#3	0.78	0.40
#4	0.71	0.33
#5	0.80	0.32
#6	0.91	0.77
#7	0.86	0.79
#8	0.86	0.80
#9	0.88	0.71
#10	0.83	0.76
#11	0.85	0.76
Avarage	0.82	0.56

Table 4.2 – Dice Coefficient has been computed comparing our segmentation and Tuff segmentation with manual segmentation done by Simple Neurite Tracer [Longair et al., 2011].

4.3 Dendrite Segmentation in 3D

A solution for dendrite segmentation was proposed for two dimensions in the previous section. Nowadays, technological tools and imaging techniques can capture high-resolution 3D images of single neurons and of populations. For this reason, it is required moving from the $2D$ to the $3D$ analysis of the whole volume. This jump is not simple and needs methods robust to noise and able to capture low signals. In our studies, different solutions were exploited. Fig. 4.5 shows the main steps carried out.

The initial preprocessing step aims at improving the image quality and reducing the background noise with a median filter applied to each data volume. Then, we estimated the dendrite direction in each voxel, computing the eigenvectors of the Hessian Matrix. To reconstruct the dendrite tracks, we connected the principal directions by adapting a well-known deterministic brain white matter tractography algorithm. Specifically, in diffusion MRI the Fiber Assignment by Continuous Tracking (FACT) algorithm by Mori and van Zijl [Mori and van Zijl, 2002] follows the main direction of the diffusion tensor starting from any voxel of a given Region of Interest (ROI). In our case, we used as ROI a dilated mask obtained from a binarization of the image processed with Frangi Filter [Frangi et al., 1998] applied slice by slice.
After this step, we explored three different solutions to obtain a continuous dendritic arborization.

For the first method, tracked dendrites have been used as the initialization mask for a Localizing Region Based Active Contour method [Lankton and Tannenbaum, 2008], which created a continuous and precise tracing of the dendrites.

The number of fiber is huge and it is computationally heavy to use all of them together. Active contour method results really slow in computing the result. For this reason, we decided to keep only the main representative traces with a clustering approach which adopted game theory, known as Dominant Set [Pavan and Pelillo, 2007]. In this way, the centroids of clusters could be seen as good representatives as parts of the centerline.

Given the cluster centroids, we followed traces and concatenated them in a path exploiting the main directions and distances in order to obtain the dendrite centerline. This geometrical method was really simple and fast but resulted imprecise and too approximate.

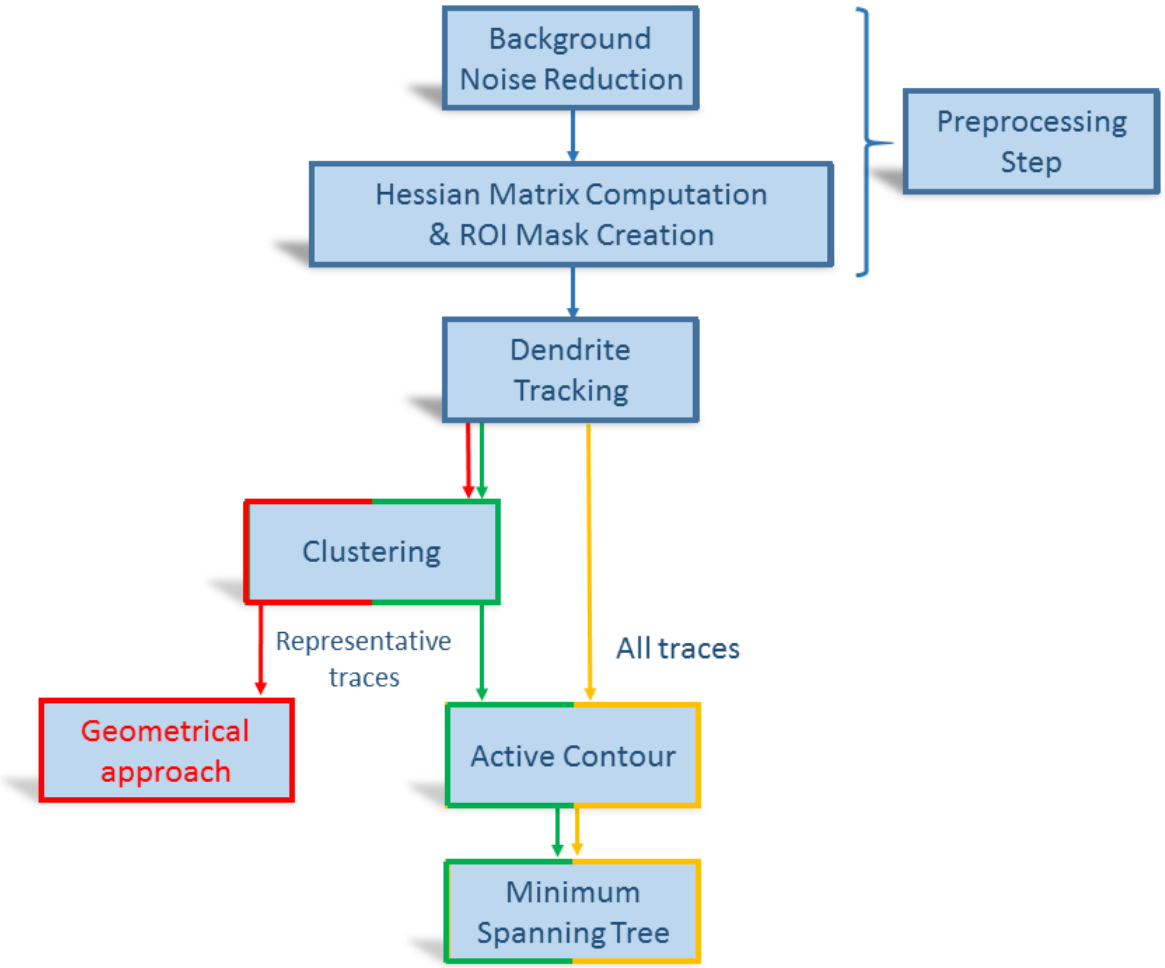

Figure 4.5 – This scheme shows the main steps of our studies exploited for finding a solution for $3D$ tracing of dendrites in neuron volume segmentation. The first part, in the blue boxes, is common to all the solutions. After dendrite tracking, three different approaches are analyzed (respectively, yellow, red and green boxes).

The third method exploited again the AC method. This time, only the centroids are used as the initialization mask of AC model that finds good and comparable results but runs very quicker than before (Fig. 4.13).

For the evaluation of the methods, we applied the Minimum Spanning Tree (MST) to our segmentations in order to obtain a single trace and to compare our results with the GT labels, given in the SWC format file.

4.3.1 Preprocessing

In order to reduce background noise, first of all we applied a 3D median filter on each volume [Gonzalez and Woods, 2001]. The median filter is a nonlinear digital filtering technique, often used to remove noise from an image or signal.

Our main idea is to track the dendrites following their direction in each voxel. So, we computed the eigenspace of the Hessian matrix that extracted the principal directions in which the local second order structure of the image could be decomposed. At this point, following Frangi's method [Frangi et al., 1998] (presented in Sec. 3.2.1), a vesselness measure is obtained on the basis of the Hessian matrix eigenvalues to delineate tubular and filament structures. The vesselness value indicates the local likelihood that a pixel in the $2D$ case or a voxel in the $3D$ belongs to a dendrite, i.e. to a vessel structure. Using this measure, we created a binary mask and we performed a morphological dilatation [Van Den Boomgaard and Van Balen, 1992]. In this way, we defined a ROI in which with high probability we could find a dendritic structures. We use this ROI for delimiting the tracking of neuron dendrite fibers in the next step. As shown in Fig. 4.8, the ROI mask would help in filtering background that can be wrongly detected and it would reduce the number of candidates decreasing the computational cost.

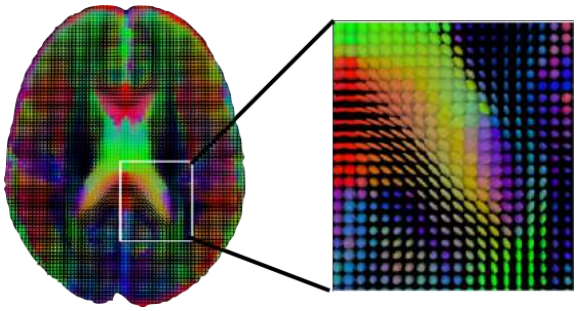

Figure 4.6 – A mid-axial slice of the ICBM (International Consortium for Brain Mapping) diffusion tensor image template. Each voxel value is a tensor represented here by an ellipsoid. Color denotes principal orientation: red = left-right, blue=inferior-superior, green = posterior-anterior.

4.3.2 Dendrite Tracking

With the Hessian matrix computation, we could obtain the directional information in each voxel. We decide to follow these directions to trace the dendritic structures. In neuroimaging, similar problems have been studied and solved in order to reconstruct brain fibers [Wakana et al., 2007], [Hagmann et al., 2006]. Inspired by diffusion MRI tractography [Mori and van Zijl, 2002], we use a deterministic approach that follows the principal direction extracted by the Hessian matrix within the Frangi's mask. Using water property, in diffusion MRI the largest principal axis of the diffusion tensor is aligned with the predominant fiber orientation in each MRI voxel. In a microscopy image, we can use the local information extracted with the Hessian and use it in order to reconstruct the dendrite arborization. An intuitive way to reconstruct a $3D$ trajectory from a $3D$ vector field is to propagate a line from a seed voxel by following its local vector orientation that, in our case, corresponds to the first eigenvector of the Hessian matrix (Fig. 4.7). To convert the discrete voxel information to a continuous tracing, we work below the image resolution and we propagate the line with a predefined step smaller than the voxel size. In this way, the resulting path is smooth respect to the image resolution. For the line propagation stopping criterion, we decide to stop when there is an angle change between voxels that would lead to an extreme turning into the line propagation.

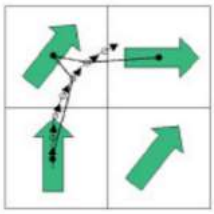

Figure 4.7 – An example of the interpolation line propagation in the $2D$ case. Big green arrows indicate the first eigenvector of the Hessian matrix. (Figure from [Mori and van Zijl, 2002].)

An example of the dendrite tracking on our samples is shown in Fig. 4.8 and in Fig. 4.9 (left). The images are characterized by inhomogeneous dendrite thickness and by gaps between the tracts due to low signal-to-noise-ratio and non-uniform fluorescent expressions. In these conditions, the aim is to create a smoother tracing filling the gaps. At this point, we investigated different approaches (Fig. 4.5).

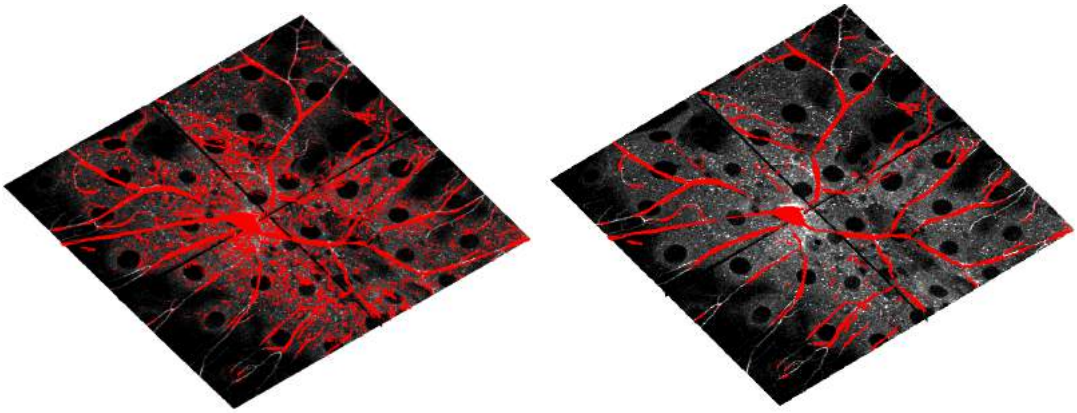

Dendrite tracking on the whole volume

Dendrite tracking with Frangi ROI

Figure 4.8 – Example of dendrite tracking without and with ROI mask by Frangi Filter. It can be noticed that in the left case (without ROI mask) the number of fibers is high and computationally hard. Thanks to the Frangi mask we can decrease the number of fibers also deleting a lot of noise.

The first method was based on active contours (Sec. 4.3.3) to create a smoother tracing filling the gaps. Our dendrite tracing is given as initialization (yellow path in Fig. 4.5). The dendrite tracking step is necessary in order to reduce the number of points that is huge and computationally unsustainable if we try to use Frangi ROI as direct initial mask.

To remedy the long computing time (several weeks on a standard Desktop computer), the second method aimed at computing representative fibers. More precisely, we clustered the traces and used the centroids of clusters to reconstruct the centerline of our dendrites (Sec. 4.3.4).

Given the centroids, an intuitive geometrical approach can be to follow the direction of each trace and reconstruct the whole dendrite path (red path in Fig. 4.5). This approach, explained in Sec. 4.3.5, is simple and based on the geometry of the traces but it is not enough effective.

The third method investigated was to apply AC model with the initialization of only centroids (Sec. 4.3.6) (green path in Fig. 4.5). This time AC runs quicker than the initialization with all traces and gives results on the same order.

4.3.3 First Method: Active Contour Model with all traces as Initialization

The Active Contour model applied in the $3D$ volumes is the Localizing Region-Based Active Contour [Lankton and Tannenbaum, 2008] that improves active contour models by a local re-formulation of traditional region-based segmentation energies [Chan et al., 2001], [Yezzi et al., 2002]. As already presented in details in Cap. 3, Sec. 3.3, localized contours can segment objects with heterogeneous statistics that would be wrongly captured by a standard global energy. Thanks to this localization, in the $3D$ case the foreground and background can be described in terms of local volumes. It avoids the assumption that the foreground and background regions are distinct based on their global statistics. Within this framework, in each point of the border, neighborhoods are split into local interior and local exterior by the evolving surface. The localization radius is chosen according to the volume-size of the objects to be segmented. In our tests we set the radius r as the average size of the dendrite diameter. In our approach, the Active Contour model takes the dendrite traces as initial mask and finds the desired continuous trace filling the gaps among tracked fibers as Fig. 4.9 shows.

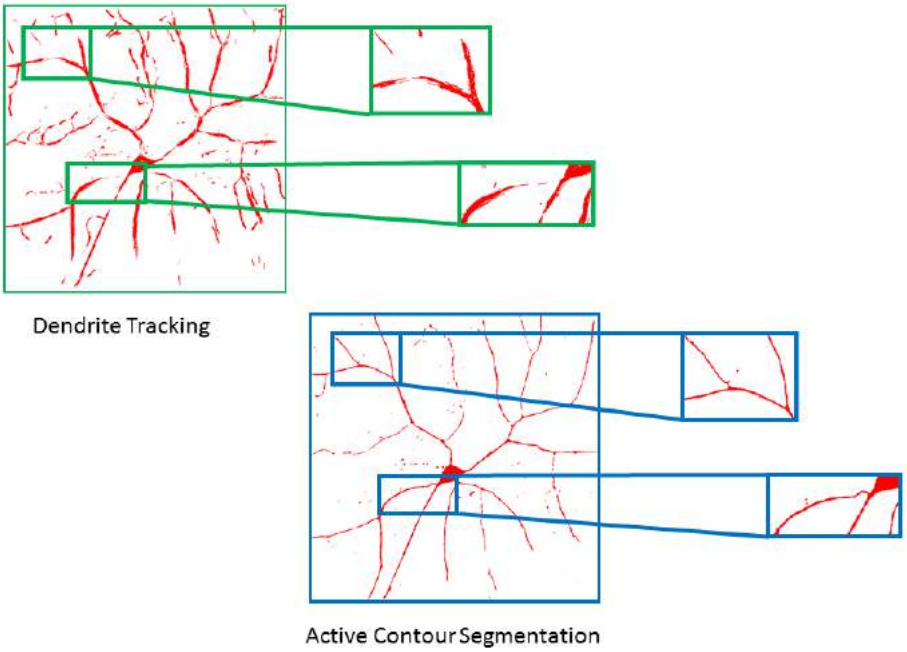

Figure 4.9 – $2D$ Visualization of dendrite tracking (in the green boxes) and of active contour segmentation (in the blue boxes) on Sample 1. After the Active Contour step, the dendrite trace becomes smoother and almost everywhere uninterrupted.

4.3.4 Clustering : Dominant Sets

The number of tracked fibers is too high for the computational cost. In order to reduce the number of fibers, a clustering approach was used before implementing the second and third methods. The centroid of each cluster becomes a good representative of the whole amount of fibers in the corresponding cluster [Dodero et al., 2014]. Among different clustering approaches, we decided to exploit the properties of Dominant Sets framework that comes from Game Theory concepts. It is robust to noise and to outliers, robust to parameter settings and it automatically infers the number of clusters.

Moreover, the tracked fibers (Fig. 4.8) have different lengths. For this reason, it is also better to divide traces in different ranges of length both for a better comparison among traces of the same length and for clustering similar structures.

Dominant Sets Clustering Method

Dominant Sets framework [Pavan and Pelillo, 2007] is a graph-theoretic method that generalizes the maximal clique problem to weighted graphs. It finds a compact, coherent and well separated subset of nodes into a graph, i.e. the *dominant set* (DS). This framework defines the correspondence between clique, DS and cluster using a graph-theoretic perspective, and provides an optimization algorithm used to extract all DSs in a graph. Formally, a dataset is represented as a weighted undirected graph $G = (V, E, \phi)$ with no self loop in which the vertices V are the data points and the edges $E \subseteq V \times V$ represent neighborhood relations among pairs of nodes, quantified by the weighting function $\phi : E \rightarrow \mathbb{R}_+$. A DS formalizes two crucial properties of all clustering techniques: the *intra-cluster homogeneity* and *inter-cluster inhomogeneity*.

A graph is compactly represented by its weighted adjacency matrix A (the affinity matrix in our approach, which is defined by Eq. 4.9) . In our setting, each trace is represented by a node in the graph and the weighting function ϕ provides a measure of the similarity between pairs of traces. Evaluating these two properties in all the possible subset of V is obviously unfeasible, for this reason the problem is casted into the following optimization task:

$$\begin{aligned} &\text{maximize} && \mathbf{x}^T A\mathbf{x} \\ &\text{subject to} && \mathbf{x} \in \triangle^n \end{aligned} \tag{4.5}$$

where $\mathbf{x}$ lies in the standard n-dimensional simplex $\triangle^n$, or equivalently, $\sum_i x_i = 1, \forall i\ x_i \geq 0$. In the DS framework, $\mathbf{x}$ is called the *weighted characteristic vector* and it quantifies the degree of participation of the i-th component in the DS. If $\mathbf{x}$ is a strict local solution of (4.5) then its support, defined as $\delta(\mathbf{x}) = \{i \mid x_i > 0\}$, is a dominant set [Pavan and Pelillo, 2003] and thus a cluster. A local maximizer of (4.5) is found using the *replicator dynamics* [Pavan and Pelillo, 2003], a result from the evolutionary game theory mimicking the temporal changes in a population, based on the fitness of its individuals:

$$x_i(t+1) = x_i(t)\frac{(A\mathbf{x}(t))_i}{\mathbf{x}(t)^T A\mathbf{x}(t)} \tag{4.6}$$

The optimization starts with a point $\mathbf{x}(t_0)$, sited in the barycenter of the simplex $\left(x_i(t_0) = \frac{1}{n}, \forall\ i\right)$. Eq. (4.6) is iterated until stability which is guaranteed to be reached if the matrix A is non-negative and symmetric. Theoretical stability condition is achieved when $\mathbf{x}(t+1) = \mathbf{x}(t)$, i.e. when the distance between two consecutive steps $||\mathbf{x}(t+1) - \mathbf{x}(t)||$ is lower than a threshold ϵ (in our setting $\epsilon = 10^{-7}$). Eq.(4.6) also guarantees the satisfaction in time of constraint in Eq.(4.5) [Pavan and Pelillo, 2003]. In practice, the algorithm operates a selection process over the components of vector $\mathbf{x}$ driven by the affinity matrix A. At convergence some elements of $\mathbf{x}$ will emerge ($x_i > 0$) and others will become extinct ($x_i = 0$). In order to extract multiple clusters a *peeling-off* strategy is applied: once a DS is determined, it is removed from the whole set of vertices V, and the process is iterated on the remaining nodes, until all elements are clustered.

Applying the method in practical cases rarely produces a vector $\mathbf{x}$ whose certain elements are equal to zero and this is mainly due to the numerical approximation or premature stopping of the dynamics. Thresholding over $\mathbf{x}$ is thus integrated into the support calculation:

$$\tilde{\delta}(\mathbf{x}) = \{i \mid x_i > \theta * \max(\mathbf{x})\} \quad \theta \in [0,1] \tag{4.7}$$

Small θ values act as noise reducer, while higher values guarantee a greater number of clusters, each one having higher internal compactness.We fixed the coherence threshold according to the findings in a previous work [Dodero et al., 2013], which needs to be very small to make the model stable ($\theta = 10^{-5}$) .

Data Encoding

In order to build the affinity matrix A, we need to define a similarity measure between fibers. We decided to build such measure exploiting the mean closest point distance as it appeared to be the most appropriate in various works [O'Donnell and Westin, 2006], [Guevara et al., 2011], [Garyfallidis et al., 2012]. To achieve an uniform representation with the same number of equidistant points, each fiber was quantized using B-spline interpolation and sampling with $k = 8$ points, as proposed in [Garyfallidis et al., 2012]. We coded the generic i-th streamline F_i as a $3D$ curve described by a set of points $F_i = \{p1...pk\}$ with $p_i \in \mathbb{R}^3$.

To cluster tracked fibers, we used the symmetrized mean closest point distance used also for White Matter (WM) fiber clustering [Guevara et al., 2011].

$$d_{smp}(F_i, F_j) = \frac{1}{2}(d_m(F_i, F_j) + d_m(F_j, F_i)) \tag{4.8}$$

defined as the average of the two directed (non-symmetric) mean closest points distances between fibers F_i and F_j.

Then, the affinity matrix $A = a_{ij}$ was defined as follows:

$$a_{ij} = \begin{cases} e^{-\frac{(d(Fi,Fj))}{\sigma}}, & \text{if } (i,j) \in \text{E} \\ 0, & \text{otherwise} \end{cases} \tag{4.9}$$

where σ is a normalization term that we imposed $\sigma = max_{i,j}(d(F_i, F_j))$ fixing a unique bound for a_{ij}, regardless of the used dataset.

Remove Low Cohesiveness Clusters

The quality of retrieved bundles is then evaluated measuring the cohesiveness, which is a quantitative index measuring the internal coherence of each cluster δ as follows:

$$C(\delta) = \mathbf{x}^T A\mathbf{x} \tag{4.10}$$

where $\mathbf{x}$ is the characteristic vector corresponding to δ and A is the adjacency matrix. High values of cohesiveness are related to clusters with high internal similarity between elements while clusters with low cohesiveness aggregates fibers with little structural significance.

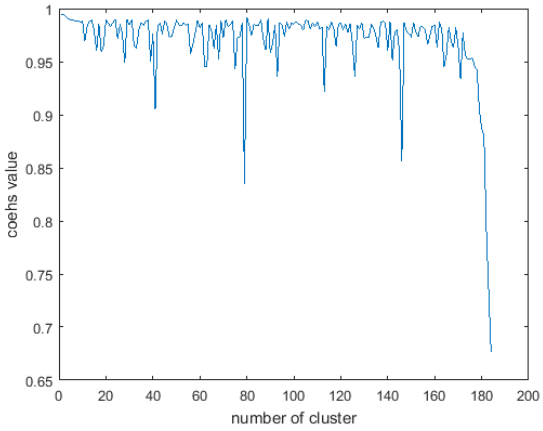

(a)

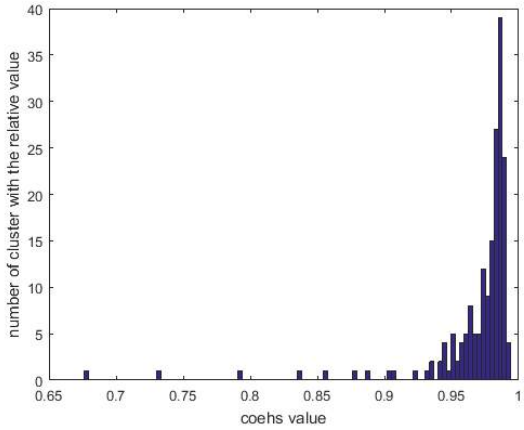

(b)

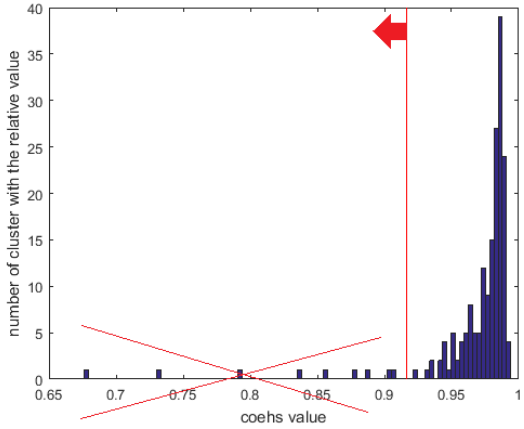

(c)

Figure 4.10 – (a) Cohesiveness value function of an example cluster. (b) Histogram of the cohesiveness. (c) First part of the cohesiveness queue removed.

Hence, we used the cohesiveness index to remove the less significant clusters and consider the relative fibers as singleton. Computed the cohesiveness (Fig. 4.10(a)), we studied the histogram and removed the first 0.5 percentile of that curve (Fig. 4.10(b)-(c)). We can also claim that the last generated clusters are generally not significant [Pavan and Pelillo, 2007] and they are part of the small group that we removed with very low internal cohesion.

4.3.5 Second Method: Geometrical approach

Once we obtained the centroids, as second approach, we followed the main direction of each centroid in a geometrical framework.
First, a trace is randomly selected among all the centroids. Then, the traces that have initial or final point within a certain range are iteratively concatenated. Before merging two traces, the main directions are computed and the angle α between them has to be smaller than a certain threshold in order to avoid an extreme turning into the dendrite structures (Fig. 4.12). If the condition is respected, the algorithm would merge the two traces by interpolation and consider the next nearest tract to the unique bigger trace. If α is too wide, the second trace is not merged with the first one and the algorithm goes ahead with the second nearest trace. The implementation would stop the dendrite reconstruction when all the traces near our reconstruction are merged or left out for an exaggerated turning into the direction.

This method is very simple and fast. The main issues of this approach are that it is not precise enough and does not result in a smooth reconstruction and when the centroids slightly overlap or are parallel one to another the interpolation could give a non linear path.

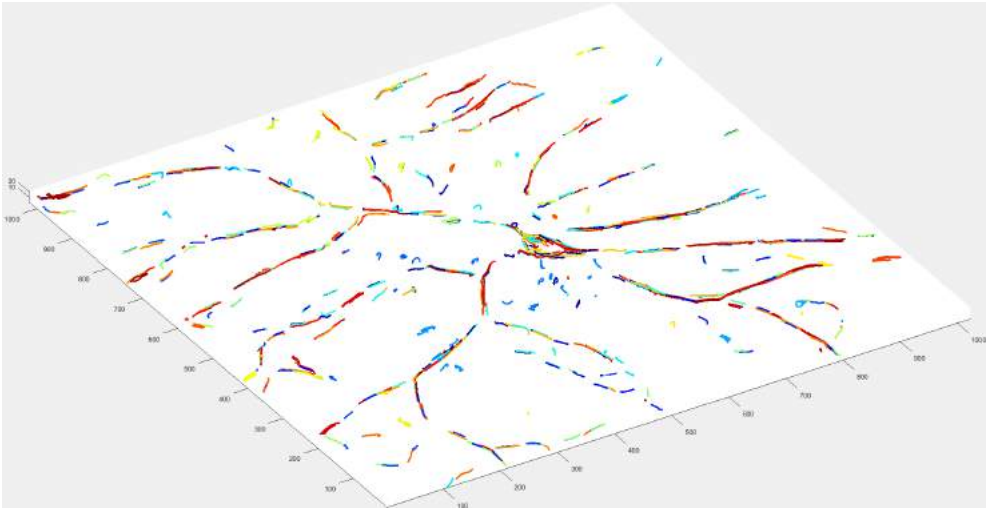

3D view

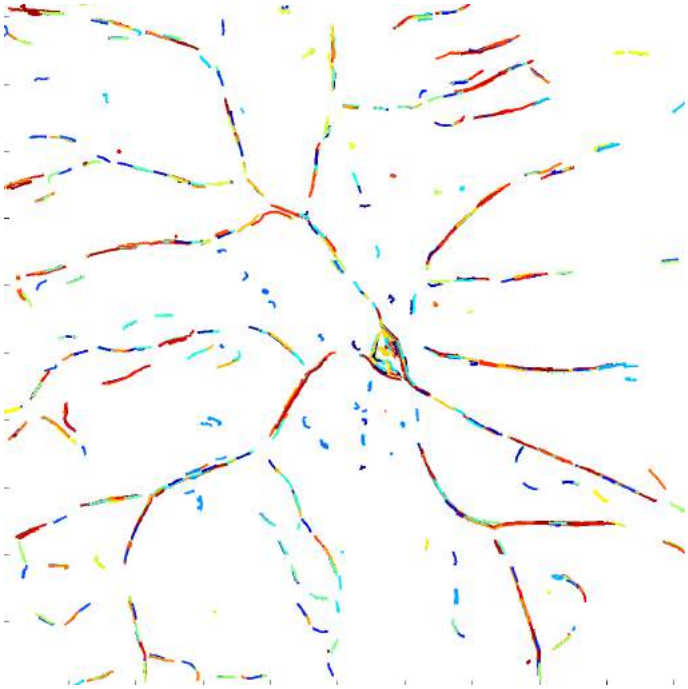

2D Projection

Figure 4.11 – An example of final centroids after low cohesiveness cluster removing.

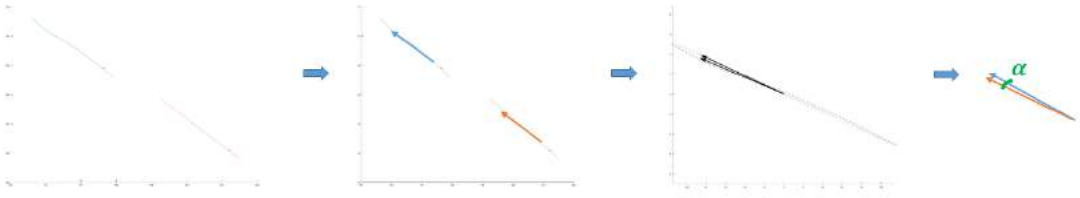

Figure 4.12 – Two near traces are selected. Then, the main directions are computed and the amplitude of the angle is taken as discriminator for the merging or not.

4.3.6 Third Method: Active Contour Model with Centroid Initialization

The third approach relied upon the most representative traces and adopted an AC model to exploit its good properties (see Sec. 3.3 and 4.3.3), given as initial mask only the centroids instead all the tracked traces (Fig. 4.13). This time the implementation goes quicker than with all the traces and reaches comparable results as we would discuss in the following Section 4.3.8.

4.3.7 Minimum Spanning Tree

Finally, to get a tree trace and the same structure as in the SWC Groud Truth file (see Sec. 1.1.1 for more details about SWC), we applied the Minimum Spanning Tree (MST) method [Siek et al., 2001] at the skeletonization of active contour segmentation.

The *Minimum-Spanning-Tree Problem* is defined as follows.
Given an undirected graph $G = (V, E)$, find an acyclic subset of the edges $T \subset E$ that connects all of the vertices in the graph and whose total weight is minimized. The total weight is the sum of the weight of the edges in T:

$$w(T) = \sum_{(u,v)\in T} w(u,v).$$

An acyclic subset of edges that connects all the vertices in the graph is called a *spanning tree*. A tree T with minimum total weight is a *minimum spanning tree*.

There are two classical algorithm for solving the minimum-spanning-tree problem: *Kruskal*'s [Kruskal, 1956] and *Prim*'s [Prim, 1957].
Kruskal's algorithm grows the minimal spanning tree (MST) one edge at a time by

finding an edge that connects two trees in a spreading forest of growing MSTs. Time complexity is $O(E + X * log(N))$, where X is the number of edges no longer than the longest edge in the MST, and N and E are the number of nodes and edges respectively.
On the other side, *Prim*'s algorithm grows the minimal spanning tree (MST) one edge at a time by adding a minimal edge that connects a node in the growing MST with any other node. Time complexity is $O(E * log(N))$, where N and E are the number of nodes and edges respectively.
Usually, *Prim*'s algorithm is the default one and it was also used in our case study by *Matlab* implementation, where the *weight* of an edge was defined as the distance among the nodes.

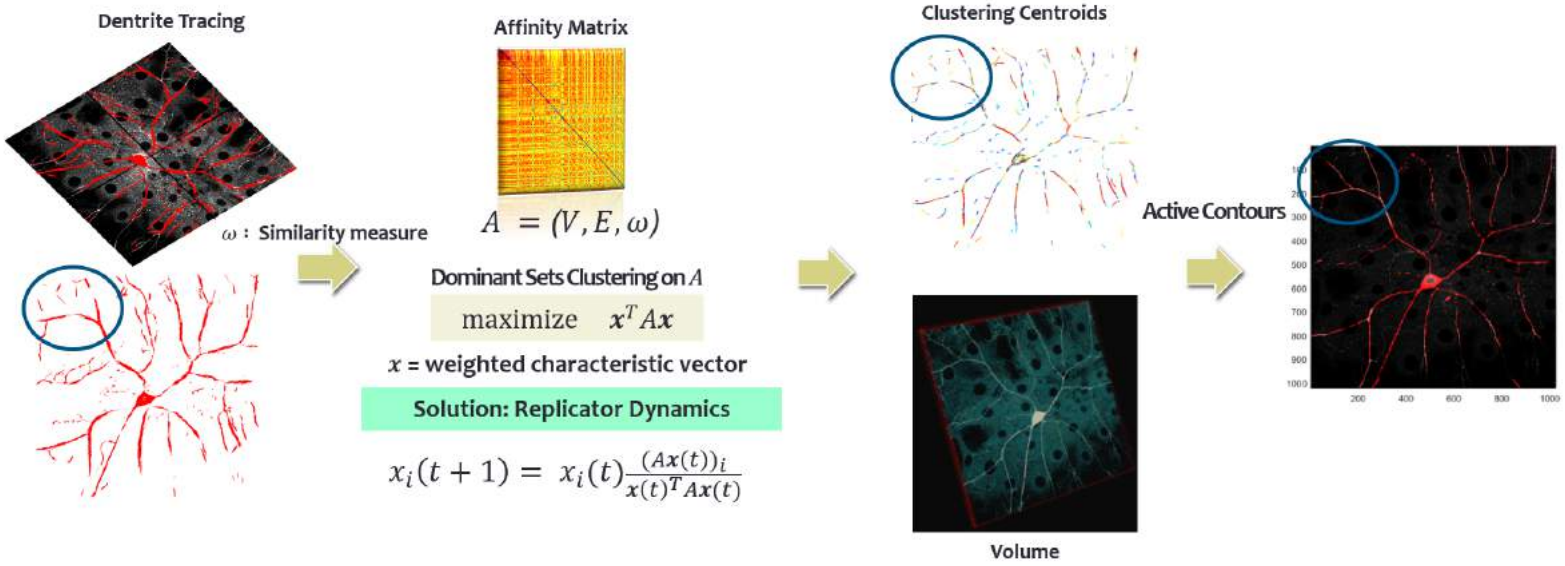

Figure 4.13 – Part of the pipeline from dendrite tracing result to the final volume segmentation according to the third method. It can be noticed that Active Contour step deletes the holes among tracked fibers and leads to a uniform reconstruction of the whole dendrite volume.

4.3.8 Results and Discussion in 3D framework

The algorithm is tested on a dataset acquired on sensory neurons in the wild-type larva *Drosophila* published in [Gulyanon et al., 2016] and studied over different development phases (see Sec. 2.3). The size of the volumes is $1024x1024x20$. They are representative of spatially inhomogeneous signal-to-noise ratios. Fig. 2.7 to 2.10 show the considered volumes. As can be seen on these Figures, samples are characterized by high variability in microscopic acquisition such as brightness, intensity, background noise, soma and dendrite shapes and development. We considered as the ground truth the same labels presented in [Gulyanon et al., 2016].

	Precision	
Samples	All traces AC	Clustering and AC
#1	0.83	0.78
#2	0.51	0.68
#3	0.72	0.70
#4	0.73	0.74
#5	0.58	0.61
#6	0.85	0.85
#7	0.88	0.88
#8	0.87	0.88
#9	0.71	0.69
#10	0.67	0.68
#11	0.67	0.66

Table 4.3 – Precision computed comparing our segmentation obtained using all tracked traces as initialization of AC (first column and corresponding to yellow path in Fig. 4.5) and clustering centroids as initialization of AC (second column and corresponding to green path in Fig. 4.5).

Some qualitative results are given in Fig. 4.13 (last column), in Fig. 4.14 and in Fig. 4.15 (right). In particular, Fig. 4.14 shows our result performed on a sample by the third method and compared with the Ground Truth tree (top image). Our segmentation (bottom image) covers almost all the dendritic tree (black circles) missing some borderline branches (blue circles) and detecting extra points not present in the Ground Truth labels (red circles). Fig. 4.15 shows the $2D$ maximum projection of a sample volume overlapped both with the Ground Truth and with our segmentation. This figure also supports the following discussion about the Ground Truth labels.

To quantify the performance, we adopted the same precision procedure as defined in [Gulyanon et al., 2016]: precision is computed by measuring the length of wrong

traces as false positives (FP) and missing traces as false negative (FN). The length of right traces is considered as true positive (TP): a trace is correct if it is within a distance (4 voxel) from the closest ground truth point. Precision is defined as

$$P = \frac{TP}{TP + FP}.$$

Table 4.3 reports respectively our results for segmenting the dendritic tree using AC initialized by all the traces in the first column and by cluster centroids in the second one. Results about the geometrical approach are not reported since this method leads to a poor and non linear reconstruction. However, thanks to its easier implementation and comprehension, this approach has been useful to understand the spatial configuration of the dendrites.

In the paper [Gulyanon et al., 2016], authors claim to reach on the considered samples the values in precision as reported in Table 4.4 (third column). They compared their results also with the Farsight method [Wang et al., 2011] (last column in Table 4.4). The precision values are higher almost in all samples. It is important to underscore that we included quantitative results for the only ground truth available. However it can be seen on Fig. 4.14 and 4.15 that dendrites we successfully segmented were not present in the published Ground Truth. As a result the quantitative results are only meant to be interpreted as indicators of the overall performance of our methods, but not as a precise performance measure of our approaches. For example, in Fig.4.15 we show two different crops (in the green and yellow circles) in which groups of dendrites are not labeled in the Ground Truth. We can observe that the connectivity path has a low signal and there are doubts about the connections. Our method leads to connect also these parts that have low-level fluorescence in the connections.
For a better understanding about the connections, another one or two slices would be required in the deep acquisitions of the stack where the signal in the low connections can be stronger. So in these dubious points the signal would have higher values in order to clarify these distinct interpretations.
Another point to be discussed is that our goal in this part of the thesis is tracing and segmenting the dendrite arborization in $3D$ volumes and not all the neuron structure. For the soma detection and segmentation we can follow other methods in the literature as [Ozcan et al., 2015] or our previous method [Baglietto et al., 2017a] presented in Chapter 3. The method can be applied to each single slice in $2D$ or can be extend to the $3D$ framework just working on the blobness filtering because the other passages in the approach have been already implemented in the three-dimensional framework.

To conclude, table 4.5 sums up the pros and cons of the three alternative approaches that can merge the traces after the tracking and reconstruct the whole dendritic tree of each sample neuron.
Part of this work is published in [Baglietto et al., 2017b] and in the paper under preparation [Baglietto et al.,].

Next step would be to apply our pipeline to neuron population stacks in $3D$ images, integrating our method with soma detection (Chapter 3) in order to distinct different neuron trees and studying distinct neuron morphologies and functions at the network scale.

	Precision			
Samples	All traces AC	Clustering and AC	Gulyanon	Farsight
#1	0.83	0.78	0.93	0.68
#2	0.51	0.68	0.91	0.50
#3	0.72	0.70	0.62	0.33
#4	0.73	0.74	0.76	0.19
#5	0.58	0.61	0.91	0.60
#6	0.85	0.85	0.89	0.91
#7	0.88	0.88	0.91	0.95
#8	0.87	0.88	0.93	0.97
#9	0.71	0.69	0.89	0.90
#10	0.67	0.68	0.89	0.91
#11	0.67	0.66	0.92	0.94

Table 4.4 – Precision computed comparing our segmentation obtained using: all tracked traces as initialization of AC (first column and corresponding to yellow path in Fig. 4.5) and clustering centroids as initialization of AC (second column and corresponding to green path in Fig. 4.5). The comparison are made with The Ground Truth labels are published in [Gulyanon et al., 2016].

Method	Pros	Cons
1) Geometrical approach	Simple and Fast Computation	Imprecise
2) AC with All Traces	Precision	Slow Computation
3) AC with Clustering Centroids	Faster than 2) and Precision	Subject to clustering parameters$^{(*)}$

Table 4.5 – Pros and Cons of the three proposed solutions for merging the traces found out by the tracker in order to reconstruct the dendritic arborization.
(*) for more details refer to Sec. 4.3.4 where it is discussed the choice of the parameters driven by previous theoretical works.

GT Graph

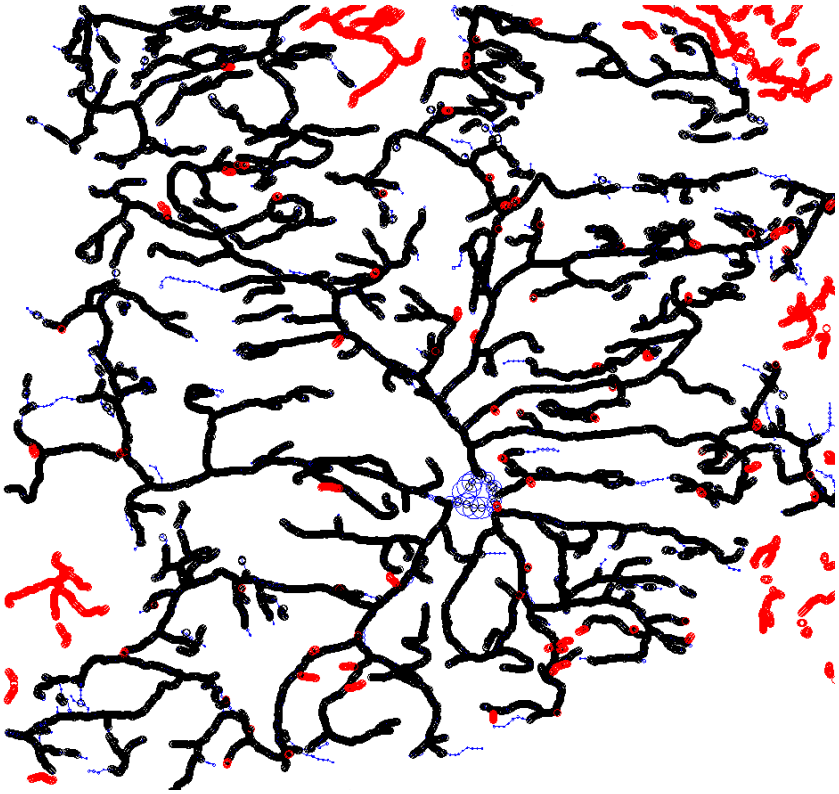

Result Graph

Figure 4.14 – Qualitative example of the AC segmentation initialized only with centroids applied on the sample #7. Black points are nodes that are correctly detected, while red are nodes wrongly detected and blue are miss one.

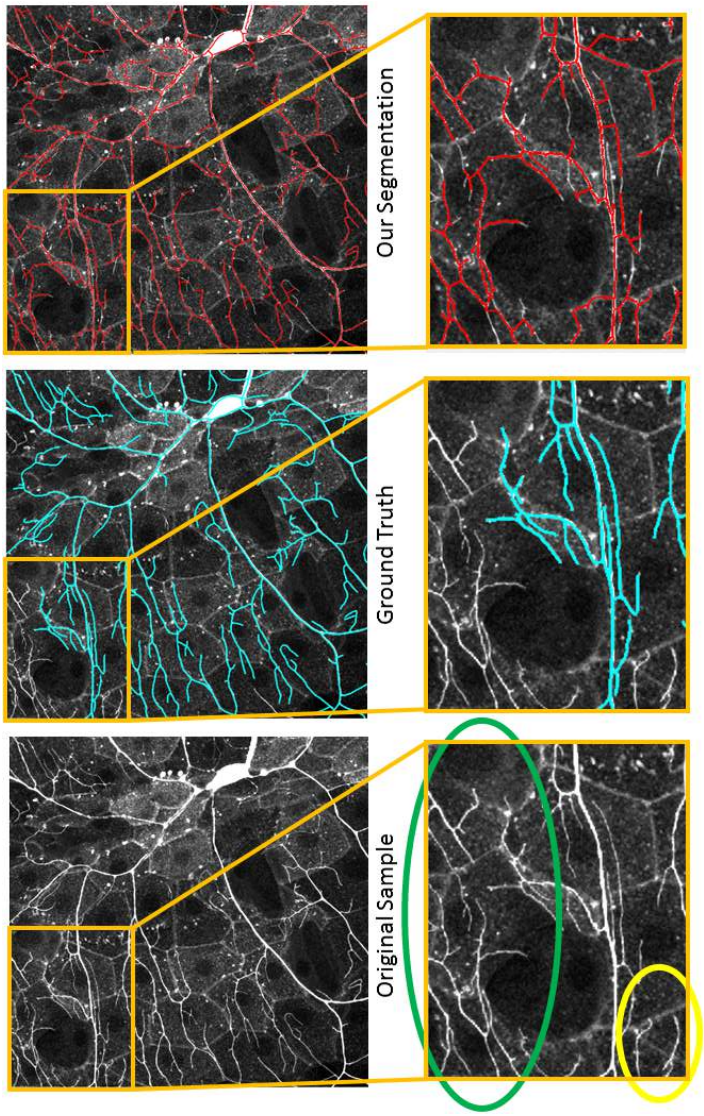

Figure 4.15 – 2*D* Visualization of maximum value on z axes of a sample volume. In the first column, the original image. In the second column, the ground truth and in the last column our segmentation. Green and yellow boxes revealed two areas that can be considered connected by low signal connections. These areas are not present in the Ground Truth labels given by [Gulyanon et al., 2016] but our algorithm detected and traced them.

Conclusion

The morphological properties of the soma and the axonal and dendritic arborizations design a key discriminant for the neuronal phenotype and play a determinant role in network connectivity.
This thesis addressed the neuroscientific request of developing a fully automatic tool for the detection and segmentation of the whole neuron morphology, opening new perspective in the study about the structure and the development of the neuronal network. The demand comes from the continuous advances in microscopy technologies and cellular imaging that capture an increasing amount of high-resolution images of single cells and of neuronal populations at different scales. These images are heterogeneous and complex and the need for computational tools and techniques to integrate and analyze these data is rising rapidly.

This work proposed a novel and completely automatic approach for fully neuron reconstruction from the detection and segmentation of the soma to the dendritic arborization tracing.

In the first part of the thesis, we developed an ad hoc approach for the localization and segmentation of neuron bodies. In this context, a novel and effective multiscale blob filter is employed for cell enhancement which selects ROIs for the initialization of an active contour step, addressing the known weakness of these methods (the need for a good initial mask). Active contour reaches satisfactory results but needs a further segmentation in case of multiple cell aggregations, which has been addressed using a watershed transform followed by a filter guided by the size of structures. We validated our approach against manual segmentations on some hundreds of neurons representative of a variety of cell appearances and image conditions. This pipeline can deal with different datasets and acquisitions both at the network and at the single cell scale, without any user interventions or manual adjustment.

Then, in the second part, various methods and research lines have been investigated

for the reconstruction of the whole dendritic arborization of each neuron, which is solved both in $2D$ and in $3D$ images. In the $2D$ case, a novel hessian-phase based level set has been developed allowing to segment the whole neuron morphology. Tests have been performed on single scale images and high performance is obtained against ground truth segmentation in comparison with an automatic state-of-the-art algorithm.
To automatically trace the 3D volume of neurons, we developed an innovative pipeline that overcomes the challenging and problematic features of the datasets. After a preprocessing step, a ROI mask of the dendrite structures is designed by Frangi Filter. The outcome is then used to drive a tracker exploiting the principal directions of local structure extracted in each voxel. After, we investigated different solutions in order to create a continuous tree starting from the tracked fibers. The first method was based on active contours initialized by all tracked traces. To improve processing speed, the second and third methods relied on keeping only the main representative traces by a Dominant Set Clustering Approach. Given the centroids, a geometrical approach is developed to merge traces in a path. This method is simple and fast but imprecise. The third method performed the segmentation by an active contour model, this time initialized only by clustering centroids. We validated our approaches against ground truth on some sensory neuron stacks and discussed the possible comparison with other methods.

The aim of this thesis was to create the premises to relate the neuronal morphology extracted by the proposed pipeline with the functional behavior. This would be obtained extracting features from the segmented neurons describing the morphology of cell-body and dendrites (e.g. Hu moments, area covered by the arborization, number of departing processes, etc.). These features could be used in a machine learning framework [Kong et al., 2005], trying to predict the functional class of the neurons. In case of success, sensitivity analysis can then be performed on the input variables to understand which features are better characterizing the neuron function.

To conclude, in this thesis we have proposed novel and improved approaches to perform a neuron segmentation. Each of the proposed solutions take into account the complexities and the properties of neuronal samples and, of course, they present strengths and limitations.

Publications

The papers published or submitted during the PhD period.

- **S. Baglietto**, I. Kepiro, G. Hilgen, E. Sernagor, V. Murino and D. Sona, *Automatic Segmentation Pipeline For Neurons From Fluorescent Microscopy Imaging*, Communications in Computer and Information Science Journal, Springer, accepted.
- **S. Baglietto**, M. Dayan, V. Murino and D. Sona, *Tractography-based dendrites reconstruction in 3D microscopic images*, to be submitted (conference paper).
- **S. Baglietto**, M. Dayan, V. Murino and D. Sona, *3D dendrite tracing inspired by diffusion MRI tractography* , BioImage Informatics (BII) Conference, Banff, Canada, 2017.
- **S. Baglietto**, I. Kepiro, G. Hilgen, E. Sernagor, V. Murino and D. Sona, *Segmentation of Retinal Ganglion Cells From Fluorescent Microscopy Imaging*, **Best Student Paper Award** at BIOIMAGING 2017, Proceedings of the 10th International Joint Conference on Biomedical Engineering Systems and Technologies - Volume 2: BIOIMAGING, BIOSTEC 2017, pages 17-23.
- P. Valentini, A. Marsella, P. Tarantino, S. Mauro, **S. Baglietto**, M. Congedo and P. Pompa, *Naked-eye fingerprinting of single nucleotide polymorphisms on psoriasis patients*, Nanoscale, 8, 11027-11033, 2016.

Bibliography

[Abràmoff et al., 2004] Abràmoff, M. D., Magalhães, P. J., and Ram, S. J. (2004). Image processing with imagej. *Biophotonics international*, 11(7):36–42.

[Arteta et al., 2013] Arteta, C., Lempitsky, V., Noble, J. A., and Zisserman, A. (2013). Learning to detect partially overlapping instances. In *Computer Vision and Pattern Recognition (CVPR), 2013 IEEE Conference on*.

[Ascoli et al., 2007] Ascoli, G. A., Donohue, D. E., and Halavi, M. (2007). Neuromorpho. org: a central resource for neuronal morphologies. *Journal of Neuroscience*, 27(35):9247–9251.

[Ascoli et al., 2010] Ascoli, G. A., Svoboda, K., and Liu, Y. (2009–2010). Neuromorpho. org: a central resource for neuronal morphologies. *The DIADEM Challenge. Available at http://www.diademchallenge.org/*.

[Baden et al., 2016] Baden, T., Berens, P., Franke, K., Rosón, M. R., Bethge, M., and Euler, T. (2016). The functional diversity of retinal ganglion cells in the mouse. *Nature*, 529(7586):345–350.

[Baglietto et al., 2017a] Baglietto, S., Kepiro, I. E., Hilgen, G., Sernagor, E., Murino, V., and Sona, D. (2017a). Segmentation of retinal ganglion cells from fluorescent microscopy imaging. *BIOIMAGING, BIOSTEC*, pages 17–23.

[Baglietto et al., subm] Baglietto, S., Kepiro, I. E., Hilgen, G., Sernagor, E., Murino, V., and Sona, D. (subm). Automatic segmentation pipeline for neurons from fluorescent microscopy imaging. *submitted to Communications in Computer and Information Science Journal, Springer*.

[Baglietto et al.,] Baglietto, S., Micheal, D., Murino, V., and Sona, D. Tractography-based dendrites reconstruction in 3d microscopic images. *under preparation*.

[Baglietto et al., 2017b] Baglietto, S., Micheal, D., Murino, V., and Sona, D. (2017b). 3d dendrite tracing inspired by diffusion mri tractography. *BioImage Informatics Conference, (BII)*.

[Bas and Erdogmus, 2011] Bas, E. and Erdogmus, D. (2011). Principal curves as skeletons of tubular objects. *Neuroinformatics*, 9(2-3):181–191.

[Basu et al., 2010] Basu, S., Aksel, A., Condron, B., and Acton, S. T. (2010). Tree2tree: Neuron segmentation for generation of neuronal morphology. In *Biomedical Imaging: From Nano to Macro, 2010 IEEE International Symposium on*, pages 548–551. IEEE.

[Baumann et al., 1999] Baumann, W., Lehmann, M., Schwinde, A., Ehret, R., Brischwein, M., and Wolf, B. (1999). Microelectronic sensor system for microphysiological application on living cells. *Sensors and Actuators B: Chemical*, 55(1):77–89.

[Benmansour and Cohen, 2011] Benmansour, F. and Cohen, L. D. (2011). Tubular structure segmentation based on minimal path method and anisotropic enhancement. *International Journal of Computer Vision*, 92(2):192–210.

[Berdondini et al., 2006] Berdondini, L., Chiappalone, M., Van Der Wal, P., Imfeld, K., de Rooij, N. F., Koudelka-Hep, M., Tedesco, M., Martinoia, S., Van Pelt, J., Le Masson, G., et al. (2006). A microelectrode array (mea) integrated with clustering structures for investigating in vitro neurodynamics in confined interconnected sub-populations of neurons. *Sensors and Actuators B: Chemical*, 114(1):530–541.

[Berdondini et al., 2009] Berdondini, L., Imfeld, K., Maccione, A., Tedesco, M., Neukom, S., Koudelka-Hep, M., and Martinoia, S. (2009). Active pixel sensor array for high spatio-temporal resolution electrophysiological recordings from single cell to large scale neuronal networks. *Lab on a Chip*, 9(18):2644–2651.

[Berson et al., 2010] Berson, D. M., Castrucci, A. M., and Provencio, I. (2010). Morphology and mosaics of melanopsin-expressing retinal ganglion cell types in mice. *Journal of Comparative Neurology*, 518(13):2405–2422.

[Beucher and Lantuéjoul, 1979] Beucher, S. and Lantuéjoul, C. (1979). Use of watersheds in contour detection. In *International workshop on image processing, real-time edge and motion detection*.

[Blake and Isard, 1998] Blake, A. and Isard, M. (1998). Active contours.

[Borst and Haag, 1996] Borst, A. and Haag, J. (1996). The intrinsic electrophysiological characteristics of fly lobula plate tangential cells: I. passive membrane properties. *Journal of computational neuroscience*, 3(4):313–336.

[Brown et al., 2011] Brown, K. M., Barrionuevo, G., Canty, A. J., De Paola, V., Hirsch, J. A., Jefferis, G. S., Lu, J., Snippe, M., Sugihara, I., and Ascoli, G. A. (2011). The diadem data sets: representative light microscopy images of neuronal morphology to advance automation of digital reconstructions. *Neuroinformatics*, 9(2-3):143–157.

[Cessac et al., 2017] Cessac, B., Kornprobst, P., Kraria, S., Nasser, H., Pamplona, D., Portelli, G., and Viéville, T. (2017). Pranas: A new platform for retinal analysis and simulation. *Frontiers in neuroinformatics*, 11:49.

[Chan et al., 2001] Chan, T. F., Vese, L., et al. (2001). Active contours without edges. *Image processing, IEEE transactions on*, 10.

[Chothani et al., 2011] Chothani, P., Mehta, V., and Stepanyants, A. (2011). Automated tracing of neurites from light microscopy stacks of images. *Neuroinformatics*, 9(2-3):263–278.

[Collins et al., 2007] Collins, T. J. et al. (2007). Imagej for microscopy. *Biotechniques*, 43(1 Suppl):25–30.

[Coombs et al., 2006] Coombs, J., Van Der List, D., Wang, G.-Y., and Chalupa, L. (2006). Morphological properties of mouse retinal ganglion cells. *Neuroscience*, 140(1):123–136.

[Coons, 1971] Coons, A. H. (1971). Introduction: the development of immunohistochemistry. *Annals of the New York Academy of Sciences*, 177(1):5–9.

[Crum et al., 2006] Crum, W. R., Camara, O., and Hill, D. L. (2006). Generalized overlap measures for evaluation and validation in medical image analysis. *IEEE transactions on medical imaging*, 25(11):1451–1461.

[Dayan et al., 2003] Dayan, P., Abbott, L., et al. (2003). Theoretical neuroscience: computational and mathematical modeling of neural systems. *Journal of Cognitive Neuroscience*, 15(1):154–155.

[De Carlos and Borrell, 2007] De Carlos, J. A. and Borrell, J. (2007). A historical reflection of the contributions of cajal and golgi to the foundations of neuroscience. *Brain research reviews*, 55(1):8–16.

[De Schutter and Bower, 1994] De Schutter, E. and Bower, J. M. (1994). An active membrane model of the cerebellar purkinje cell. i. simulation of current clamps in slice. *Journal of neurophysiology*, 71(1):375–400.

[Derpanis, 2005] Derpanis, K. G. (2005). Quadrature filters. *Department of Computer Science and Engineering, York University*.

[Dodero et al., 2013] Dodero, L., Vascon, S., Giancardo, L., Gozzi, A., Sona, D., and Murino, V. (2013). Automatic white matter fiber clustering using dominant sets. In *Pattern Recognition in Neuroimaging (PRNI), 2013 International Workshop on*, pages 216–219. IEEE.

[Dodero et al., 2014] Dodero, L., Vascon, S., Murino, V., Bifone, A., Gozzi, A., and Sona, D. (2014). Automated multi-subject fiber clustering of mouse brain using dominant sets. *Frontiers in neuroinformatics*, 8.

[Donohue and Ascoli, 2011] Donohue, D. E. and Ascoli, G. A. (2011). Automated reconstruction of neuronal morphology: an overview. *Brain research reviews*, 67(1):94–102.

[El Allaoui et al., 2012] El Allaoui, A. et al. (2012). Medical image segmentation by marker-controlled watershed and mathematical morphology. *The International Journal of Multimedia & Its Applications*, 4(3):1.

[Feldt et al., 2011] Feldt, S., Bonifazi, P., and Cossart, R. (2011). Dissecting functional connectivity of neuronal microcircuits: experimental and theoretical insights. *Trends in neurosciences*, 34(5):225–236.

[Feng et al., 2015] Feng, L., Zhao, T., and Kim, J. (2015). neutube 1.0: a new design for efficient neuron reconstruction software based on the swc format. *eneuro*, 2(1):ENEURO–0049.

[Fiala, 2005] Fiala, J. C. (2005). Reconstruct: a free editor for serial section microscopy. *Journal of microscopy*, 218(1):52–61.

[Florack et al., 1992] Florack, L. M., ter Haar Romeny, B. M., Koenderink, J. J., and Viergever, M. A. (1992). Scale and the differential structure of images. *Image and Vision Computing*, 10(6):376–388.

[Frangi et al., 1998] Frangi, A. F., Niessen, W. J., Vincken, K. L., and Viergever, M. A. (1998). Multiscale vessel enhancement filtering. In *Medical Image Computing and Computer-Assisted Interventation MICCAI 98*, pages 130–137. Springer.

[Frasconi et al., 2014] Frasconi, P., Silvestri, L., Soda, P., Cortini, R., Pavone, F. S., and Iannello, G. (2014). Large-scale automated identification of mouse brain cells in confocal light sheet microscopy images. *Bioinformatics*, 30(17):i587–i593.

[Garyfallidis et al., 2012] Garyfallidis, E., Brett, M., Correia, M. M., Williams, G. B., and Nimmo-Smith, I. (2012). Quickbundles, a method for tractography simplification. *Frontiers in neuroscience*, 6(December):175.

[Ge et al., 2015] Ge, Q., Li, C., Shao, W., and Li, H. (2015). A hybrid active contour model with structured feature for image segmentation. *Signal Processing*, 108:147–158.

[Gonzalez and Woods, 2001] Gonzalez, R. C. and Woods, R. E. (2001). *Digital Image Processing*. Addison-Wesley Longman Publishing Co., Inc., Boston, MA, USA, 2nd edition.

[Granlund and Knutsson, 2013] Granlund, G. H. and Knutsson, H. (2013). *Signal processing for computer vision*. Springer Science & Business Media.

[Gregory, 2015] Gregory, R. L. (2015). *Eye and Brain: The Psychology of Seeing: The Psychology of Seeing*. Princeton university press.

[Gross, 1999] Gross, C. G. (1999). *Brain, vision, memory: Tales in the history of neuroscience*. MIT Press.

[Guevara et al., 2011] Guevara, P., Poupon, C., and Rivière, D. (2011). Robust clustering of massive tractography datasets. *Neuroimage*, 54(3):1975–1993.

[Gulyanon et al., 2015] Gulyanon, S., Sharifai, N., Bleykhman, S., Kelly, E., Kim, M. D., Chiba, A., and Tsechpenakis, G. (2015). Three-dimensional neurite tracing under globally varying contrast. In *Biomedical Imaging (ISBI), 2015 IEEE 12th International Symposium on*, pages 875–879. IEEE.

[Gulyanon et al., 2016] Gulyanon, S., Sharifai, N., Kim, M. D., Chiba, A., and Tsechpenakis, G. (2016). Crf formulation of active contour population for efficient three-dimensional neurite tracing. In *2016 IEEE 13th International Symposium on Biomedical Imaging (ISBI)*, pages 593–597. IEEE.

[Hagmann et al., 2006] Hagmann, P., Jonasson, L., Maeder, P., Thiran, J.-P., Wedeen, V. J., and Meuli, R. (2006). Understanding diffusion mr imaging techniques: from scalar diffusion-weighted imaging to diffusion tensor imaging and beyond. *Radiographics*, 26(suppl_1):S205–S223.

[Halavi et al., 2012] Halavi, M., Hamilton, K. A., Parekh, R., and Ascoli, G. A. (2012). Digital reconstructions of neuronal morphology: three decades of research trends. *Frontiers in neuroscience*, 6.

[Halavi et al., 2008] Halavi, M., Polavaram, S., Donohue, D. E., Hamilton, G., Hoyt, J., Smith, K. P., and Ascoli, G. A. (2008). Neuromorpho. org implementation of digital neuroscience: dense coverage and integration with the nif. *Neuroinformatics*, 6(3):241.

[Häusser et al., 2000] Häusser, M., Spruston, N., and Stuart, G. J. (2000). Diversity and dynamics of dendritic signaling. *Science*, 290(5492):739–744.

[Jaccard, 1901] Jaccard, P. (1901). Étude comparative de la distribution florale dans une portion des alpes et des jura. *Bull Soc Vaudoise Sci Nat*, 37:547–579.

[Jimbo et al., 1999] Jimbo, Y., Tateno, T., and Robinson, H. (1999). Simultaneous induction of pathway-specific potentiation and depression in networks of cortical neurons. *Biophysical Journal*, 76(2):670–678.

[Kandel et al., 2000] Kandel, E. R., Schwartz, J. H., Jessell, T. M., Siegelbaum, S. A., Hudspeth, A. J., et al. (2000). *Principles of neural science*, volume 4. McGraw-hill New York.

[Kim et al., 2010] Kim, I.-J., Zhang, Y., Meister, M., and Sanes, J. R. (2010). Laminar restriction of retinal ganglion cell dendrites and axons: subtype-specific developmental patterns revealed with transgenic markers. *The Journal of Neuroscience*, 30(4):1452–1462.

[Koenderink, 1984] Koenderink, J. J. (1984). The structure of images. *Biological cybernetics*, 50(5):363–370.

[Kong et al., 2005] Kong, J.-H., Fish, D. R., Rockhill, R. L., and Masland, R. H. (2005). Diversity of ganglion cells in the mouse retina: unsupervised morphological classification and its limits. *Journal of Comparative Neurology*, 489(3):293–310.

[Kruskal, 1956] Kruskal, J. B. (1956). On the shortest spanning subtree of a graph and the traveling salesman problem. *Proceedings of the American Mathematical society*, 7(1):48–50.

[Lankton and Tannenbaum, 2008] Lankton, S. and Tannenbaum, A. (2008). Localizing region-based active contours. *Image Processing, IEEE Transactions on*, 17(11):2029–2039.

[Lathen et al., 2008] Lathen, G., Jonasson, J., and Borga, M. (2008). Phase based level set segmentation of blood vessels. In *Pattern Recognition, 2008. ICPR 2008. 19th International Conference on*, pages 1–4. IEEE.

[Läthén et al., 2010] Läthén, G., Jonasson, J., and Borga, M. (2010). Blood vessel segmentation using multi-scale quadrature filtering. *Pattern Recognition Letters*, 31(8):762–767.

[Lee et al., 1994] Lee, T.-C., Kashyap, R. L., and Chu, C.-N. (1994). Building skeleton models via 3-d medial surface axis thinning algorithms. *CVGIP: Graphical Models and Image Processing*, 56(6):462–478.

[Leergaard et al., 2012] Leergaard, T. B., Hilgetag, C. C., and Sporns, O. (2012). Mapping the connectome: multi-level analysis of brain connectivity. *Frontiers in neuroinformatics*, 6.

[Lindeberg, 1998] Lindeberg, T. (1998). Edge detection and ridge detection with automatic scale selection. *International Journal of Computer Vision*, 30(2):117–156.

[Liu et al., 2010] Liu, J., White, J. M., and Summers, R. M. (2010). Automated detection of blob structures by hessian analysis and object scale. In *Image Processing (ICIP), 2010 17th IEEE International Conference on*, pages 841–844. IEEE.

[Longair et al., 2011] Longair, M. H., Baker, D. A., and Armstrong, J. D. (2011). Simple neurite tracer: open source software for reconstruction, visualization and analysis of neuronal processes. *Bioinformatics*, 27(17):2453–2454.

[Lorenz et al., 1997] Lorenz, C., Carlsen, I.-C., Buzug, T. M., Fassnacht, C., and Weese, J. (1997). Multi-scale line segmentation with automatic estimation of width, contrast and tangential direction in 2d and 3d medical images. In *CVRMed-MRCAS'97*, pages 233–242. Springer.

[Maccione et al., 2012] Maccione, A., Garofalo, M., Nieus, T., Tedesco, M., Berdondini, L., and Martinoia, S. (2012). Multiscale functional connectivity estimation on low-density neuronal cultures recorded by high-density cmos micro electrode arrays. *Journal of neuroscience methods*, 207(2):161–171.

[Marom and Eytan, 2005] Marom, S. and Eytan, D. (2005). Learning in ex-vivo developing networks of cortical neurons. *Progress in Brain research*, 147:189–199.

[Meijering, 2010] Meijering, E. (2010). Neuron tracing in perspective. *Cytometry Part A*, 77(7):693–704.

[Meijering, 2012] Meijering, E. (2012). Cell segmentation: 50 years down the road [life sciences]. *Signal Processing Magazine, IEEE*, 29(5):140–145.

[Meijering et al., 2004] Meijering, E., Jacob, M., Sarria, J.-C., Steiner, P., Hirling, H., and Unser, M. (2004). Design and validation of a tool for neurite tracing and analysis in fluorescence microscopy images. *Cytometry Part A*, 58(2):167–176.

[Meijering et al., 2003] Meijering, E. H., Jacob, M., Sarria, J.-C. F., and Unser, M. (2003). A novel approach to neurite tracing in fluorescence microscopy images. In *SIP*, pages 491–495.

[Morel and Solimini, 2012] Morel, J.-M. and Solimini, S. (2012). *Variational methods in image segmentation: with seven image processing experiments*, volume 14. Springer Science & Business Media.

[Mori and van Zijl, 2002] Mori, S. and van Zijl, P. C. M. (2002). Fiber tracking: principles and strategies – a technical review. *NMR in Biomedicine*, 15(7-8):468–480.

[Mukherjee et al., 2015] Mukherjee, S., Condron, B., and Acton, S. T. (2015). Tubularity flow field—a technique for automatic neuron segmentation. *IEEE Transactions on Image Processing*, 24(1):374–389.

[Myatt and Nasuto, 2008] Myatt, D. R. and Nasuto, S. J. (2008). Improved automatic midline tracing of neurites with neuromantic. *BMC Neuroscience*, 9(S1):P81.

[Narayanaswamy et al., 2011] Narayanaswamy, A., Wang, Y., and Roysam, B. (2011). 3-d image pre-processing algorithms for improved automated tracing of neuronal arbors. *Neuroinformatics*, 9(2-3):219–231.

[Neumann and H 2016] Neumann, S. and H L. (2016). Cell type-specific bipolar cell input to ganglion cells in the mouse retina. *Neuroscience*, 316:420 – 432.

[O'Donnell and Westin, 2006] O'Donnell, L. and Westin, C.-F. (2006). High-dimensional white matter atlas generation and group analysis. *MICCAI*, 9(Pt 2):243–51.

[Osher and Fedkiw, 2003] Osher, S. and Fedkiw, R. (2003). Implicit functions. In *Level Set Methods and Dynamic Implicit Surfaces*, pages 3–16. Springer.

[Osher and Sethian, 1988] Osher, S. and Sethian, J. A. (1988). Fronts propagating with curvature-dependent speed: algorithms based on hamilton-jacobi formulations. *Journal of computational physics*, 79(1):12–49.

[Ozcan et al., 2015] Ozcan, B., Negi, P., Laezza, F., Papadakis, M., and Labate, D. (2015). Automated detection of soma location and morphology in neuronal network cultures. *PloS one*, 10(4):e0121886.

[Palágyi and Kuba, 1998] Palágyi, K. and Kuba, A. (1998). A 3d 6-subiteration thinning algorithm for extracting medial lines. *Pattern Recognition Letters*, 19(7):613–627.

[Paragios et al., 2006] Paragios, N., Chen, Y., and Faugeras, O. D. (2006). *Handbook of mathematical models in computer vision*. Springer Science & Business Media.

[Pavan and Pelillo, 2003] Pavan, M. and Pelillo, M. (2003). A new graph-theoretic approach to clustering and segmentation. In *Proceedings. Computer Society Conference on Computer Vision and Pattern Recognition.*, volume 1, pages I–145. IEEE.

[Pavan and Pelillo, 2007] Pavan, M. and Pelillo, M. (2007). Dominant sets and pairwise clustering. *Pattern Analysis and Machine Intelligence, IEEE Transactions on*, 29(1):167–172.

[Pawley, 2006] Pawley, J. B. (2006). Fundamental limits in confocal microscopy. In *Handbook of biological confocal microscopy*, pages 20–42. Springer.

[Peng et al., 2010] Peng, H., Ruan, Z., Long, F., Simpson, J. H., and Myers, E. W. (2010). V3d enables real-time 3d visualization and quantitative analysis of large-scale biological image data sets. *Nature biotechnology*, 28(4):348–353.

[Pool et al., 2008] Pool, M., Thiemann, J., Bar-Or, A., and Fournier, A. E. (2008). Neuritetracer: a novel imagej plugin for automated quantification of neurite outgrowth. *Journal of neuroscience methods*, 168(1):134–139.

[Prasad et al., 2007] Prasad, V., Semwogerere, D., and Weeks, E. R. (2007). Confocal microscopy of colloids. *Journal of Physics: Condensed Matter*, 19(11):113102.

[Prim, 1957] Prim, R. C. (1957). Shortest connection networks and some generalizations. *Bell Labs Technical Journal*, 36(6):1389–1401.

[Reuman and Capowski, 1984] Reuman, S. R. and Capowski, J. (1984). Automated neuron tracing using the marr-hildreth zerocrossing technique. *Computers and biomedical research*, 17(2):93–115.

[Roska et al., 2006] Roska, B., Molnar, A., and Werblin, F. S. (2006). Parallel processing in retinal ganglion cells: how integration of space-time patterns of excitation and inhibition form the spiking output. *Journal of Neurophysiology*, 95(6):3810–3822.

[Rykhlevskaia et al., 2008] Rykhlevskaia, E., Gratton, G., and Fabiani, M. (2008). Combining structural and functional neuroimaging data for studying brain connectivity: a review. *Psychophysiology*, 45(2):173–187.

[Sato et al., 1997] Sato, Y., Nakajima, S., Atsumi, H., Koller, T., Gerig, G., Yoshida, S., and Kikinis, R. (1997). 3d multi-scale line filter for segmentation and visualization of curvilinear structures in medical images. In *CVRMed-MRCAS'97*, pages 213–222. Springer.

[Schindelin et al., 2012] Schindelin, J., Arganda-Carreras, I., Frise, E., Kaynig, V., Longair, M., Pietzsch, T., Preibisch, S., Rueden, C., Saalfeld, S., Schmid, B., et al. (2012). Fiji: an open-source platform for biological-image analysis. *Nature methods*, 9(7):676–682.

[Schmitt et al., 2004] Schmitt, S., Evers, J. F., Duch, C., Scholz, M., and Obermayer, K. (2004). New methods for the computer-assisted 3-d reconstruction of neurons from confocal image stacks. *Neuroimage*, 23(4):1283–1298.

[Schneider et al., 2012] Schneider, C. A., Rasband, W. S., and Eliceiri, K. W. (2012). Nih image to imagej: 25 years of image analysis. *Nature methods*, 9(7):671–675.

[Segev and Rall, 1998] Segev, I. and Rall, W. (1998). Excitable dendrites and spines: earlier theoretical insights elucidate recent direct observations. *Trends in neurosciences*, 21(11):453–460.

[Semwogerere and Weeks, 2005] Semwogerere, D. and Weeks, E. R. (2005). Confocal microscopy. *Encyclopedia of Biomaterials and Biomedical Engineering*, 23:1–10.

[Seung, 2012] Seung, S. (2012). *Connectome: how the brain's wiring makes us who we are*. Houghton Mifflin Harcourt.

[Siek et al., 2001] Siek, J. G., Lee, L.-Q., and Lumsdaine, A. (2001). *The Boost Graph Library: User Guide and Reference Manual, Portable Documents*. Pearson Education.

[Spira and Hai, 2013] Spira, M. E. and Hai, A. (2013). Multi-electrode array technologies for neuroscience and cardiology. *Nature nanotechnology*, 8(2):83–94.

[Sporns, 2011] Sporns, O. (2011). The human connectome: a complex network. *Annals of the New York Academy of Sciences*, 1224(1):109–125.

[Sporns et al., 2005] Sporns, O., Tononi, G., and Kötter, R. (2005). The human connectome: a structural description of the human brain. *PLoS computational biology*, 1(4):e42.

[Srinivasan et al., 2010] Srinivasan, R., Li, Q., Zhou, X., Lu, J., Lichtman, J., and Wong, S. T. (2010). Reconstruction of the neuromuscular junction connectome. *Bioinformatics*, 26(12):i64–i70.

[Stockley et al., 1993] Stockley, E., Cole, H., Brown, A., and Wheal, H. (1993). A system for quantitative morphological measurement and electrotonic modelling of neurons: three-dimensional reconstruction. *Journal of neuroscience methods*, 47(1):39–51.

[Storch, 2000] Storch, W. B. (2000). *Immunofluorescence in clinical immunology: a primer and atlas*. Springer Science & Business Media.

[Svoboda, 2011] Svoboda, K. (2011). The past, present, and future of single neuron reconstruction. *Neuroinformatics*, 9(2-3):97–98.

[Thomas et al., 1972] Thomas, C., Springer, P., Loeb, G., Berwald-Netter, Y., and Okun, L. (1972). A miniature microelectrode array to monitor the bioelectric activity of cultured cells. *Experimental cell research*, 74(1):61–66.

[Torben-Nielsen et al., 2007] Torben-Nielsen, B., Tuyls, K., and Postma, E. O. (2007). *On the Neuronal Morphology-Function Relationship: A Synthetic Approach*, pages 131–144. Springer Berlin Heidelberg, Berlin, Heidelberg.

[Tsai et al., 2003] Tsai, R., Osher, S., et al. (2003). Level set methods and their applications in image science. *Communications in Mathematical Sciences*, 1(4):1–20.

[Türetken et al., 2011] Türetken, E., González, G., Blum, C., and Fua, P. (2011). Automated reconstruction of dendritic and axonal trees by global optimization with geometric priors. *Neuroinformatics*, 9(2-3):279–302.

[Van Den Boomgaard and Van Balen, 1992] Van Den Boomgaard, R. and Van Balen, R. (1992). Methods for fast morphological image transforms using bitmapped binary images. *CVGIP: Graphical Models and Image Processing*, 54(3):252–258.

[Wakana et al., 2007] Wakana, S., Caprihan, A., Panzenboeck, M. M., Fallon, J. H., Perry, M., Gollub, R. L., Hua, K., Zhang, J., Jiang, H., Dubey, P., et al. (2007). Reproducibility of quantitative tractography methods applied to cerebral white matter. *Neuroimage*, 36(3):630–644.

[Wang et al., 2011] Wang, Y., Narayanaswamy, A., Tsai, C.-L., and Roysam, B. (2011). A broadly applicable 3-d neuron tracing method based on open-curve snake. *Neuroinformatics*, 9(2):193–217.

[Wearne et al., 2005] Wearne, S., Rodriguez, A., Ehlenberger, D., Rocher, A., Henderson, S., and Hof, P. (2005). New techniques for imaging, digitization and analysis of three-dimensional neural morphology on multiple scales. *Neuroscience*, 136(3):661–680.

[Wikipedia,] Wikipedia.

[Wu et al., 2015] Wu, P., Yi, J., Zhao, G., Huang, Z.and Qiu, B., and Gao, D. (2015). Active contour-based cell segmentation during freezing and its application in cryopreservation. *Biomedical Engineering, IEEE Transactions on*, 62(1):284–295.

[Yezzi et al., 2002] Yezzi, A., Tsai, A., and Willsky, A. (2002). A fully global approach to image segmentation via coupled curve evolution equations. *Journal of Visual Communication and Image Representation*, 13(1):195–216.

[Zhang et al., 2014] Zhang, C., Yarkony, J., and Hamprecht, F. A. (2014). Cell detection and segmentation using correlation clustering. In *Medical Image Computing and Computer-Assisted Intervention–MICCAI 2014*, pages 9–16. Springer.

[Zhao et al., 2011] Zhao, T., Xie, J., Amat, F., Clack, N., Ahammad, P., Peng, H., Long, F., and Myers, E. (2011). Automated reconstruction of neuronal morphology based on local geometrical and global structural models. *Neuroinformatics*, 9(2-3):247–261.

[Zheng and Hong, 2016] Zheng, Z. and Hong, P. (2016). Incorporate deep-transfer-learning into automatic 3d neuron tracing. *BRAININFO 2016 : The First International Conference on Neuroscience and Cognitive Brain Information*.

[Zijdenbos et al., 1994] Zijdenbos, A. P., Dawant, B. M., Margolin, R., Palmer, A. C., et al. (1994). Morphometric analysis of white matter lesions in mr images: method and validation. *Medical Imaging, IEEE Transactions on*, 13(4):716–724.

[Zordan et al., 2015] Zordan, S., Zanotto, M., Nieus, T., Di Marco, S., Amin, H., Maccione, A., and Berdondini, L. (2015). A scalable high performance client/server framework to manage and analyze high dimensional datasets recorded by 4096 cmos-meas. In *Neural Engineering (NER), 2015 7th International IEEE/EMBS Conference on*, pages 968–971. IEEE.